HIGHLY CONDUCTIVE STRETCHABLE ELECTRICALLY CONDUCTIVE COMPOSITES FOR ELECTRONIC AND RADIO FREQUENCY DEVICES

A Thesis
Presented to
The Academic Faculty

by

Joshua C. Agar

In Partial Fulfillment
of the Requirements for the Degree
Master of Science in the
School of Materials Science and Engineering

Georgia Institute of Technology
August 2011

HIGHLY CONDUCTIVE STRETCHABLE ELECTRICALLY CONDUCTIVE COMPOSITES FOR ELECTRONIC AND RADIO FREQUENCY DEVICES

Approved by:

Dr. C.P. Wong, Advisor
School of Materials Science and Engineering
Georgia Institute of Technology

Dr. Meisha Shofner
School of Materials Science and Engineering
Georgia Institute of Technology

Dr. Christopher Summers
School of Materials Science and Engineering
Georgia Institute of Technology

Dr. Karl Jacob
School of Materials Science and Engineering
Georgia Institute of Technology

Date Approved: June 29, 2011

To my Grandfathers Irwin Olefson and Robert Agar who both passed away during my study at Georgia Institute of Technology

ACKNOWLEDGEMENTS

First, I would like to express my gratitude to my advisor Professor C. P. Wong for his advise, support and encouragement regardless of how ridiculous my ideas and objectives were. His unrelenting encouragement to try anything and everything was fundamental in my ability to fail repeatedly without being deterred before finally discovering. I would also like to thank my Professors who provided me with the knowledge, skills and insight needed to be a successful engineer. I would like to specifically thank Professor Paul Braun, Professor Steve Granick and Professor John Rogers for instilling in me their unique insight and methodologies to approach scientific discoveries. I would like to extend my gratitude to the member of my committee Professor Meisha Shofner, Professor Karl Jacob and Professor Christopher Summers for reading through my abnormally long thesis and for their unique and valuable insight and perspective.

I would like to thank my family for all the support they provided during my study.

I would also like to thank the following faculty and staff members for their guidance and support during my study: Dr. Meilin Liu, Dr. Robert Snyder, Dr. Tom Sanders, Dr. Seth Marder, Dr. Naresh Thadhani, Dr. Zhong Lin Wang, Dr. Lisa Rosenstein, Dr. David Gottfried, Mrs. Susan Bowman, Mr. James Cagle, Mr. John Holthaus, Mr. Tim Banks, Mr. Rusty Edwards, Ms. Sarah Johnson, Mr. Dean Sutter, Ms. Karen H. Mayo, Ms. Angie Beggs, Ms. Shirley Manchester, Ms. Jasmin Frett-Hodge, Ms. Jyoti Ghosh, Mrs. Hope Payne Dr. Yolande Berta. I would like to give a special

thanks to Mrs. Debbie Wolf-Lopez for saving me from loss of multiple limbs and Dr. Manos Tentzeris for teaching me the value of humility.

I would also like to thanks my program managers and collaborators: Dr. Stefanie Lotz, Dr. Venky Sundaram, Ms. Giulia Orecchini, Dr. Manos Tentzeris, Mr. Abhishek Choudhury, Mr. Nitesh Kumbhat.

I would like to acknowledge the input and help I received from my fellow co-workers: Mr. Wei Lin, Mr. Qizhen Liang, Mrs. Yan Liu, Mrs. Zhuo Li, Mr. Ziyin Lin, Mr. Wentian Gu, Ms. Fan Cai, Dr. Cheng Yang, Dr. Yagang Yao, Dr. Jintang Shang, Mr. Shaun Zhang and Mr. Stewart Wilkens. I would also like to thank my undergraduate students: Ms. Katy Lin, Ms. Jessica Durden and Mr. Kevin Lawrence. I would like to give a special thanks to my three main collaborators, Dr. Rongwei Zhang, Dr. Jack Moon and Dr. Daniela Staiculescu who provided insight and perspective on a daily basis. Furthermore I would like to thank Dr. Daniela Staiculescu for watching my cat during all of my travel.

Finally, I would like to acknowledge the funding agencies who supported my study Intel Corporation and National Science Foundation.

TABLE OF CONTENTS

	Page
ACKNOWLEDGEMENTS	iv
LIST OF TABLES	xi
LIST OF FIGURES	xii
LIST OF SYMBOLS	xvii
LIST OF ABBREVIATIONS	xxi
SUMMARY	xxiii
Chapter	
1 Introduction	1
1.1 Electronics in the modern era	1
1.2 Electronic packaging in the modern era	2
1.3 Introduction to electrically conductive adhesives	4
1.4 Basic properties of isotropically conductive adhesives	6
1.5 Compositions of ICAs	9
1.5.1 Polymeric matrix formulations	9
1.5.2 Chemistry of epoxy ICAs	11
1.5.3 Chemistry of silicone ICAs	16
Peroxide-cured silicones	19
Condensation-cure silicones	20
Hydrosilylation-cured silicones	21
1.5.4 Conductive fillers	23
1.6 Processing of ICAs	26
1.6.1 Printing processes	26

1.6.2 Curing process of ICAs 29
1.7 Processing of anisotropically conductive and non-conductive adhesives 31
1.8 Electrical conduction mechanism in ECCs 33
1.8.1 Modeling electrical conduction in ECCs 34
Discrepancies with published models 36
1.8.2 Methods to increase electrical conductivity of ECC 41
Incorporation of high aspect ratio or 1D fillers: 41
Low temperature sintering of nanoparticles 42
Increased polymer matrix shrinkage 44
In-situ replacement / removal of surfactant on particle surfaces 44
1.8.3 Concluding remarks 45
1.9 Future perspective on ECCs for electronic packaging 45
1.10 Research methodology and objectives 47
2 Understanding the Interface in Electrically conductive Composites 49
2.1 Introduction 49
2.2 Experimental methods 50
2.2.1 Theoretical reconceptualization of the filler interface 50
2.2.2 Effect of matrix dielectric on electrical conductivity 50
2.3 Theoretical conceptualization of the filler-filler interface 51
2.4 Effect of matrix dielectric constant on electrical conductivity in ECCs 58
2.5 Outlook and perspective 61
3 Stretchable Electrically Conductive Composites 63
3.1 Motivation 63

3.2 Methods of packaging stretchable electronics 64
3.2.1 Stretchable geometries 64
3.2.2 Stretchable electro-Active materials 67
3.3 1st generation stretchable electrically conductive polydimethylsiloxane 69
3.3.1 Experimental methods 70
Fabrication and characterization of highly conductive PDMS stretchable electrically conductive composites 70
Characterization of the tensile-electrical response of S-ECC 71
Patterning and device level integration 72
3.3.2 Results and discussion 72
Fabrication and characterization of highly conductive PDMS stretchable electrically conductive composites 72
Characterization of the tensile-electrical response of S-ECC 74
Patterning and device level integration 77
Outlook and perspective 79
3.4 Second Generation Stretchable Electrically Conductive PDMS 80
3.4.1 Experimental methods 80
Effect of AA on electrical properties of S-ECC 80
Mechanical characterization of S-ECC 81
3.4.2 Results and discussion 82
Effect of AA on electrical properties of S-ECC 82
Mechanical characterization of S-ECC 86
3.5 Stretchable 3D interconnects using S-ECC 89

3.5.1 Fabrication of stretchable package 90

3.5.2 Results and discussion 93

3.6 3rd generation stretchable electrically conductive composites 97

3.6.1 Formulation and characterization of PDMS matrix material 97

Fourier transform infrared spectroscopy (FTIR) 98

Thermal analysis of S-ECC 103

3.6.2 Scanning electron micrograph of S-ECC 112

Electrical properties of S-ECC 117

Encapsulation and transfer of S-ECC 119

Electrical mechanical response of S-ECC 120

4 Stretchable RF Devices 126

4.1 Fundamentals of microstrip lines 127

4.2 Fabrication of stretchable microstrip line 131

4.3 RF characterization of stretchable microstrip line 133

4.4 Fabrication of stretchable RF antenna 136

5 Summary, Conclusions and Future areas of interest 139

5.1 Summary of results 139

5.2 Future work 141

5.2.1 Understanding of the conduction mechanism in ECC 141

5.2.2 Stretchable conductive composites 141

Ultra-low stress large area interconnects 142

Inkjettable stretchable electrically conductive composite 142

Ultra low cost stretchable electrically conductive composite 143

5.3 Stretchable radio frequency devices 143

5.4 Concluding remarks 144

REFERENCES 147

LIST OF TABLES

Page

Table 1. Comparison of properties of conductive adhesives and Metallic Solders [15] 7

Table 2. Comparison of processing of metallic solder and ICA 8

Table 3. Comparison of adhesive matrixes for ICA applications [16]. 11

Table 4. Material properties of commercial silicones [28-30]. 17

Table 5. Commercial forms of silicone elastomers [42]. 19

Table 6. General materials requirements for ink-jet printable ICAs [83]. 29

Table 7. Possible through film electron transport mechanisms that contribute to tunneling resistance in ECCs [102]. 40

Table 8. ECA formulations tested. 51

Table 9. Table showing the silicone polymers acquired. 98

Table 10. Typical absorption spectra for siloxanes and alkyl polymers [195]. 99

Table 11. Comparison of performance of formulated S-ECC to published literature. 125

LIST OF FIGURES

Figure 1. Schematic drawing of packaging levels [4]. 3

Figure 2. Schematic drawing of interconnection using A. isotropically conductive adhesives B. anisotropically conductive adhesives C. non-conductive adhesives [11]. 6

Figure 3. Molecular structures of A. DGEBF B. MHHPA C. 2E4MZCN 12

Figure 4. Catalyzed epoxy anhydride curing mechanism 15

Figure 5. Molecular structure of PDMS 16

Figure 6. Crosslinking mechanism of peroxide cured silicones. 20

Figure 7. Sn catalyzed condensation reaction. 21

Figure 8. A. Hydrosilylation cross-linking in the presence of Pt catalyst. B. Catalysis mechanism of hydrosilylation by platinum based on Chalk and Harrod mechanism [44, 45]. 23

Figure 9. Image showing A. Stencil printing process. B. Screen printing process [80]. Reprinted with permission of John Wiley & Sons, Inc. 28

Figure 10. Time temperature transformation (TTT) diagram [84]. Blue line indicates ideal ICA curing profile. 31

Figure 11. A. Schematic plot showing transition from non-conductive to conductive percolated network. B. Schematic representation of a percolated network of conductive fillers in a polymeric matrix. 34

Figure 12. Schematic drawing showing circuit diagram of a single particle trapped between bumps in a single ACF interconnect. Inset shows regions where current flow occurs through a constricted metal contact and tunneling [101]. 36

Figure 13. Schematic drawing of electron transfer via an A. Extended state B. Localized state 40

Figure 14. DSC of surfactant desorption from the surface of Ag 26 LV [11]. 52

Figure 15. DSC of surfactant desorption from the surface of Ag 52 [11]. 53

Figure 16. Isothermal DSC of silver flakes at 150°C [11]. 53

Figure 17. TGA showing desorption of surfactant from the surface of Ag flakes [11]. 54

Figure 18. Schematic diagram of interface between two silver flakes on close approach [11]. 55

Figure 19. Diagram of particle interaction with chemically adsorbed stearic acid [11]. 56

Figure 20. DSC showing curing peak of virgin 862 cured with 2E4MZCN catalyst [11]. 59

Figure 21. DSC showing curing peak of CoAcAC doped 862 epoxy cured with 2E4MZCN catalyst [11]. 59

Figure 22. DSC showing curing peak of 862 epoxy catalyzed by CoAcAc [11]. 60

Figure 23. ECA resistivity as a function of CoAcAc concentration (dielectric constant) [11]. 61

Figure 24. Isothermal TMA of S-ECC during curing at 150°C [186]. 73

Figure 25. Bulk resistivity of S-ECC as a function of curing temperature [186]. 74

Figure 26. DMA of conventional Sylgard 184 PDMS following annealing at 150°C for 1 hour [186]. 75

Figure 27. Contact angle measurements of A. UVO treated PDMS and B. Untreated PDMS [186]. 76

Figure 28. Images of A. tensile mold, B. tensile mold embedded with S-ECC, C. un-strained tensile specimen D. strained tensile specimen [186]. 77

Figure 29. Graph showing measured resistance during tensile strain [186]. 77

Figure 30. Images of lines fabricated in A. photoresist B. PDMS [186]. 78

Figure 31. Schematic drawing showing fabrication process of S-ECC based electronics [186]. 79

Figure 32. SEM image showing morphology of Ag flakes A. Virgin B. Treated at 150°C for 10 min and C. Treated at 150°C for 30 min A. 84

Figure 33. MDSC of A. Ag flakes B. Ag flakes with AA. 86

Figure 34. Graph of simultaneous tensile electro-mechanical characterization of silicone S-ECC. Inset: stress strain curve of dog bone tensile specimen [193]. 87

Figure 35. Schematic illustration of technique to fabricate 3D structures of S-ECC [195]. 92

Figure 36. Schematic drawing of the fabricated 5-layer assembly of interconnected S-ECC [195]. 93

Figure 37. 3D confocal micrograph of A. Stretchable “via” like structures B. Electrically isolated layers within the stretchable conductive 3D package [195]. 94

Figure 38. TMA of PDMS-encapsulate (sample size 1.161 mm) and stretchable conductive composites (sample size 1.2817 mm) [195]. 96

Figure 39. Molecular structure of A. Vinyl functionalized PDMS B. Hydride functionalized PDMS. C. Karstedt catalyst. 98

Figure 40. Sigma Aldrich (~580 Mn) hydride terminated PDMS. 100

Figure 41. Gelest hydride terminated PDMS. 101

Figure 42. FTIR spectra of Wacker 1200A vinyl functionalized PDMS. 101

Figure 43. FTIR Spectra of the uncured PDMS formulation. 102

Figure 44. FTIR spectra of the cured PDMS formulation. 103

Figure 45. TMA of A. S-ECC matrix. B. S-ECC. C. PDMS encapsulant. 105

Figure 46. DSC showing the curing temperature of the PDMS matrix. 106

Figure 47. Idealized plot of polymeric transitions in DMA during a temperature sweep experiment at a constant oscillation frequency. 108

Figure 48. DMA of S-ECC during cooling and heating. 110

Figure 49. DSC of silicone matrix crystallization. 111

Figure 50. SEM image of top surface morphology of A. S-ECC B. S-ECC with AA. 113

Figure 51. SEM cross-sectional images of S-ECC after 5,000 cycles to tensile strain of 50% A. Parallel to strain direction in virgin formulation. B. Parallel to tensile strain AA treated flakes. C. Perpendicular to tensile strain virgin formulation. D. Perpendicular to tensile strain AA treated. 114

Figure 52. SEM image showing A. surface topography and perpendicular cross section of S-ECC after 5000 tensile elongations to 50%. B. Surface of AA treated S-ECC strained to 30%. 115

Figure 53. Surface morphology of Ag flakes in virgin composite formulation. 116

Figure 54. Reduction of surfactant by hydride-terminated silicone. 116

Figure 55. Graph showing S-ECC resistivity as a function of curing temperature. 117

Figure 56. Electrical conductivity of S-ECC as a function of Relative vinyl concentration. Black box plots are for virgin formulations and the blue boxplots are for AA treated formulations. 119

Figure 57. Electrical resistivity during cyclical tensile elongations to 50%. 122

Figure 58. Resistivity of stretchable conductive composite as a function of 85°C/85% RH aging time after mechanical deformation to 150% elongation >5000 times and manually applied biaxial strain to elongations >200%. 124

Figure 59. Schematic drawing of a microstrip line. 128

Figure 60. Schematic diagram showing the process to fabricate stretchable microstrip line [193]. 132

Figure 61. Photographs of microstrip line indicating its ability to flex, stretch and twist [193]. 133

Figure 62. S-parameter measurement results for different line configurations: B. Straight C. Bent D. Twisted [193]. 135

Figure 63. Cross-section of stretchable microstrip line after testing [193]. 136

Figure 64. Images showing A. Printed antenna on Teflon B. Stretchable antenna after encapsulation. 137

Figure 65. S11 measurements of fabricated unstrained antenna. 138

LIST OF SYMBOLS

°C	Celsius
W	Ohm
ω	Frequency of strain oscillation
Φ	Work function
σ	Conductivity
ρ_t	Tunneling resistivity
ρ	Resistivity Density of crosslinks
ν_{iJ}	Hopping rate between sites i and j
N	Poisson's ratio
λ	Wavelength
δ	Indentation depth
δ	Phase lag between stress and strain
γ	Propagation constant
β	Phase
α_R	Loss due to radiation
α_G	Loss due to conductivity of dielectric
α_D	Loss due to dielectric loss tangent
α_c	Loss due to metal conductivity
α	Localization length Attenuation
Z_0	Characteristic impedance

W	Watt
V	Volts
T_γ	Gamma transition
T_β	Beta transition
T_r	Williams-Landel-Ferry constant
T_m	Melting temperature
T_{g0}	Glass transition temperature of uncured resin
$T_{g\infty}$	Temperature where polymer cures completely
T_g	Glass transition temperature
Tc	Crystallization temperature
tan δ	Dielectric loss tangent
t	Time
S_{21}	Insertion Loss, reflection
S_{11}	Input return loss, transmission
S	Film thickness
R_{total}	Total resistance of conductive filler contact
R_t	Tunneling resistance
R_f	Filler resistance
R_{CR}	Constriction resistance
R_c	Contact resistance
R’	Metallic loss

R	Radius Gas constant
psi	Pounds per square inch
P	Normal stress on adsorbed layer
MPa	Megapascals
Moles	Mol
Mil	1/1000 of an inch
M_c	Molecular weight between crosslinks
K_{eff}	Effective dielectric constant
K_{bulk}	Bulk modulus
K	Kelvin
J	Joules
H_0	Height of monolayer
H	Thickness
G’	Shear storage modulus
F_H	Shull Correction factor
F	Force
F	Frequency
E”	Loss modulus
E’	Storage modulus
dB	Decibels
d	Particle diameter
D	Contact diameter

CTE	Thermal coefficient of expansion
C_2	Williams-Landel-Ferry constant
C_1	Williams-Landel-Ferry constant
a	Radius of contact with monolayer
3D	Three-dimensional
$\varepsilon_{r\perp}$	Dielectric constant
μ_0	Williams-Landel-Ferry constant
υ_0	Mechanism dependent constant
$\sigma_{y\perp}$	Yield stress
$\varepsilon_i, \varepsilon_j$	Energy at state i,j
δ_H	Shull Correction factor
R_{RFSH}	Radio-frequency sheet resistance
r_{ij}	Distance between sites i and j

LIST OF ABBREVIATIONS

2E4MZCN	1-cyanoethyl-2-ethyl-4-methylimidazole
ACA/ACF	Anisotropically conductive adhesives / films
CCD	Charge coupled devices
CoAcAc	Cobalt (III) acetylacetonate
DEA	Dielectric analysis
DGEBF	Diglycidyl ether of Bisphenol F
DSC	Differential scanning calorimetry
e-Sn/Pb	Eutectic tin-lead
ECA	Electrically conductive adhesives
ECC	Electrically conductive composites
FTIR	Fourier Transform Infrared spectroscopy
GaInEu	Gallium indium eutectic
HFSS	High frequency structure simulator
HTV	High temperature vulcanizing
I/O	Input/outputs
IC	Integrated circuit
ICA	Isotropically conductive adhesives
LED	Light emitting diodes
LR	Liquid rubber
LT-TLPS	Low temperature transient liquid phase sintering
MDSC	Modulated differential scanning calorimetry
MHHPA	4-methylhexahydrophthalic anhydride

NCA/NCF	Non-conducting adhesives / films
Pb	Lead
PCB	Printed circuit board
PDMS	Poly(dimethylsiloxane)
RF	Radio frequency
RFID	Radio frequency identification
RTV-1, RTV-2	Room temperature vulcanizing
S-ECC	Stretchable electrically conductive composite
Sn	Tin
TGA	Thermogravimetric analysis
TTT	Time-temperature-transformation
UVO	UV-ozone
Vol	Volume
WBAN	Wireless body area networks
Wt	Weight

SUMMARY

The electronics industry is shifting its emphasis from reducing transistor size and operational frequency to increasing device integration, reducing form factor and increasing the interface of electronics with their surroundings. This new emphasis has created increased demands on the electronic package. To accomplish the goals to increase device integration and interfaces will undoubtedly require new materials with increased functionality both electrically and mechanically.

This thesis focuses on developing new interconnect and printable conductive materials capable of providing power, ground and signal transmission with enhanced electrical performance and mechanical flexibility and robustness. More specifically, we develop: 1.) A new understanding of the conduction mechanism in electrically conductive composites (ECC). 2.) Develop highly conductive stretchable silicone ECC (S-ECC) via *in-situ* nanoparticle formation and sintering. 3.) Fabricate and test stretchable radio frequency devices based on S-ECC. 4.) Develop techniques and processes necessary to fabricate a stretchable package for stretchable electronic and radio frequency devices.

In this thesis we provide convincing evidence that conduction in ECC occurs predominantly through secondary charge transport mechanism (tunneling, hopping). Furthermore, we develop a stretchable silicone-based ECC which, through the incorporation of a special additive, can form and sinter nanoparticles on the surface of the metallic conductive fillers. This sintering process decreases the contact resistance and enhances conductivity of the composite. The conductive composite developed has the best reported conductivity, stretchability and reliability. Using this S-ECC we fabricate a

stretchable microstrip line with good performance up to 6 GHz and a stretchable antenna with good return loss and bandwidth.

The work presented provides a foundation to create high performance stretchable electronic packages and radio frequency devices for curvilinear spaces. Future development of these technologies will enable the fabrication of ultra-low stress large area interconnects, reconfigurable antennas and other electronic and RF devices where the ability to flex and stretch provides additional functionality impossible using conventional rigid electronics.

CHAPTER 1

INTRODUCTION

1.1 Electronics in the modern era

Within the past decade there has been an exponential expansion in humans' reliance on their electronic devices. Today you would be hard-pressed to find a single person more than an arms length away from an internet connected device. The increased availability of capable mobile devices has created a highly competitive consumer driven industry, where the consumer demands for improved form factor, functionality and performance of electronic devices are unrelenting.

Within this past decade the boom in device performance and capabilities has been the result of improved fabrication capabilities, enabling higher transistor densities per chip. For example the current Intel Xenon processors are fabricated with 45 nm manufacturing processes, where a decade ago, in 2001 Intel Xenon processors used 180 nm manufacturing technology [1]. Gordon Moore originally theorized the evolution of transistor miniaturization rate in his landmark paper Cramming More Components onto Integrated Circuits [2]. Moore hypothesized that the size of the transistor would be reduced in half every two years [2]. However, realizations of transistors smaller than 16 nm is fundamentally impossible due to electronic tunneling through gates smaller than 5 nm [3]. It has been theorized that this fundamental limit to Moore's law will be realized by 2018 [3]. To realize increased performance after achieving this fundamental size limitation of the transistor will require a radical new approach to transistor design or more likely a change in packaging and integration.

1.2 Electronic packaging in the modern era

An Electronic package contains all of the form and function necessary to connect the integrated circuit (IC) with the world. Typical electronic packages have four key functions: signal distribution, power distribution, heat dissipation and mechanical stability. When discussing electronic packaging technologies, it is typical to divide the package into four levels:

Level 0: Semiconductor Chip (IC)

Level 1: Chip carrier (lead frame)

Level 2: Mounting of packaged IC to printed circuit board (PCB) or another substrate.

Level 3: Board-to-board connections.

In level 1 interconnection, the IC is mounted onto a chip carrier commonly called lead frame. Attaching the chip to the lead frame is accomplished using interconnect materials: solder or electrically conductive adhesives (ECAs) or through wire bonding, tape automated bonding or flipchip assembly. Following formation of level 1 interconnection the chip is hermetically sealed; either with a lid or a polymer mold. Following level 1 interconnection the packaged IC is mounted on the PCB. The assembled PCB is then directly interconnected on the motherboard. A schematic drawing showing the interconnection levels is shown in Figure 1.

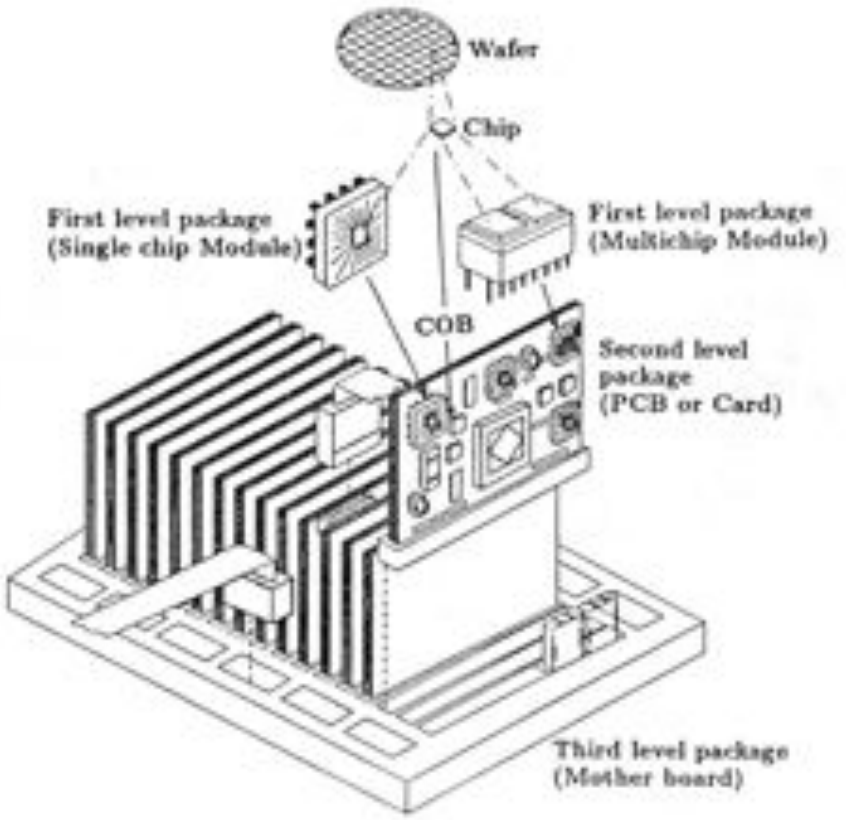

Figure 1. Schematic drawing of packaging levels [4].

Due to the limitations of Moore's law industry has been increasingly interested in exploiting new architecture and packaging to increase performance of electronic devices without decreasing transistor dimensions. This new ideology has resulted in multi-cored devices. However, creating electronic devices with increased parallel processing capabilities has created increasing demands on the electronic package. Current objectives in electronic packaging include decreasing pitch, improving number of input/outputs (I/O), reducing power consumption, reducing resistivity and improving software to maximize performance. To obtain these objectives will undoubtedly require new high performance materials, processes and designs. From a materials standpoint the greatest challenge remains the electrical interconnect material.

1.3 Introduction to electrically conductive adhesives

The semiconductor industry has made considerable strides within the past decades but integration and interconnection of components into electronic systems has remained essentially unchanged. Lead (Pb) based alloys like eutectic tin-lead (e-Sn/Pb) solders have been the interconnect material of choice used for power, ground and signal transmission in the semiconductor industry. However, toxicological and environmental concerns associated with lead based interconnects have caused manufacturers to seek alternative interconnect materials.

To date, efforts to produce alternative interconnect materials have focused on two alternatives: Lead-free solders and electrically conductive adhesives (ECAs). Most lead free solders contain Tin (Sn) because it is inexpensive and melts at relatively low temperatures (232°C). However, the melting temperature (T_m) is high when compared with conventional Pb based solders (T_m=183°C). It is desirable to processes electronics at temperatures <150°C to minimize thermal incompatibilities and increase long term reliability. Although some lower temperature Lead-free solders are available, Indium/Tin (Sn/In T_m=120°C), Tin/Bismuth (Sn/Bi T_m=138°C), and Tin/Zinc/Silver/Aluminum/Gallium (Sn/Zn/Ag/Al/Ga T_m=189°C), their properties and processability are still of concern [5]. On the other hand, polymer-based composite systems like ECAs are the ideal interconnect alternative to lead-containing solder interconnects. Electrically conductive adhesives mainly consist of a composite formed from conductive particles embedded in a polymeric resin (epoxy, polyimide, polyurethane or silicone). In these composites the polymer provides adhesions, toughness, physical shape and structure, while the metallic fillers (silver, gold, nickel,

copper) provide electrical conductivity. Compared to metallic solder technology, ECAs offer numerous advantages, such as environmental friendliness (elimination of lead usage and flux cleaning), mild processing conditions, fewer processing steps (reducing processing cost), and fine pitch capability [6, 7]. Polymer-based ECAs offer the advantage that they can be processed at T < 150°C, significantly lower than metallic solders. The widespread use of polymer based ECAs with low temperature processability would dramatically reduce the carbon footprint of the semiconductor industry.

ECAs have been commonly classified into three categories: isotropically conductive adhesives (ICA), anisotropically conductive adhesives / films (ACA / ACF) and non-conducting adhesives / films (NCA / NCF). ICA generally have high metallic filler loadings >80 wt% (~25-30 vol%) [8, 9]. The high filler loading in ICAs creates an electrically interconnected network unconfined by directionality (Figure 2A). ACAs (Figure 2B) in comparison have reduced metallic filler loadings (<5-10 wt%), below the percolation threshold. The formation of conductive pathways in ACF is established after thermal-compression bonding. The low filler loading in ACA interconnects limits the conduction pathway to direction of the compressive load during bonding. NCA (Figure 2C), unlike ICA and ACA, does not contain any conductive particles; instead an organic adhesive is used to bond the bump to the pad under an applied pressure (1-500 MPa) and elevated temperatures (T~150 ºC). It is believed that the conductivity in NCAs results from the formation of metallic contact resulting from asperities on the bump surfaces[10].

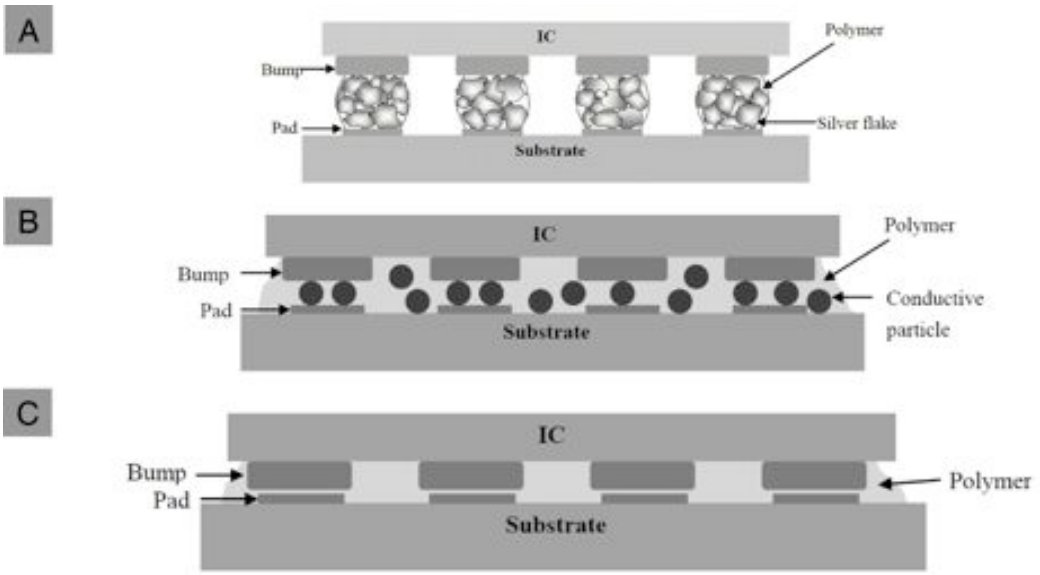

Figure 2. Schematic drawing of interconnection using A. isotropically conductive adhesives B. anisotropically conductive adhesives C. non-conductive adhesives [11].

1.4 Basic properties of isotropically conductive adhesives

ICAs are conductive adhesives that most resemble metallic solder due to their isotropic electrical properties. However, the isotropic nature of ICAs means they must be patterned to obtain the interconnection without shorting. Compared to metallic solder, ICAs have numerous advantages that make them a desired alternative to metallic solders. ICAs do not contain Pb, do not require flux, have mild processing conditions and fewer processing steps [12-14]. These features result in lower stress on the package following cure, enhancing yield and reliability [12-14]. Despite these beneficial attributes ICAs have a few key limitations that have slowed their widespread use in electronic components. ICAs compared to metallic solders have much lower electrical and more importantly thermal conductivities, have worse reliability, lower current carrying

capacity, reduced impact toughness, etc [12-14]. A comparison of the properties of Sn/Pb solder and ICAs can be seen in Table 1.

Table 1. Comparison of properties of conductive adhesives and Metallic Solders [15]

Characteristic	**Sn/Pb solder**	**ICA**
Volume resistivity (Ω cm)	0.000015	0.00035
Typical junction R (mΩ)	10-15	<25
Thermal conductivity (W/m K)	30	3.5
Shear strength (psi)	>2200	2000
Finest pitch (mil)	12	<6-8
Minimum processing temperature (^{o}C)	215	150-170
Environmental impact	Negative	Very minor
Thermal fatigue	Yes	Minimal

From a processing standpoint there are many advantages for the use of ICAs instead of metallic solders. Besides the environmental aspects and fewer processing steps already mentioned, ICAs offer more variability for application specific material design. ICAs can be formulated with special additives, with specific chemical functionality. For example, ICA can be tailored to achieve strong adhesion to a wide variety of surfaces, were solder adhesion tends to be limited only to metallic surfaces. Moreover, modification of the polymer curing mechanism and cure kinetics can be used to control curing temperature and rate of curing, enabling curing times between seconds and hours and cure temperatures between room-temperature and 200°C. Most importantly ICAs can be made compliant, enabling the decoupling of the IC from the substrate. This can be used as an effective method to minimize the stress caused by CTE mismatch between the IC and the substrate. Stress generation from CTE mismatch is the key limiting factor in determining the maximum die dimensions. The ability to use compliant ICAs will enable increased size, interconnection and functionality between the IC and the substrate. A comparison of the processing of solder and ICAs is shown in Table 2.

Table 2. Comparison of processing of metallic solder and ICA

Connection Method	Advantages	Limitations
Solder	Batch processing Automated dispensing or screen-printing Automated reflow Long history of use/mature process Easy reworkability	Requires flux Risk of flux residues and corrosion Concern over toxicity of lead Corrosion of solder in humid environments, if not encapsulated Risk of voids under large component Large stress due to large CTE mismatches High temperature exposure during solder reflow (220-260°C) Limited wetting and adhesion to some surface (e.g. glass)
Conductive adhesive	Wide range of processing temperatures (23-200°C) Fine-pitch capability Automated dispensing or screen-printing Application-specific formulations Wide variety of commercially available products to choose from Ability to relieve stress Easy to add additives that provide excellent adhesion to a wide variety of surfaces Snap cure types cure in seconds (160-200 °C) Directional conductivity with anisotropic forms May be reworkable	Lower electrical and thermal conductivities compared with solder Risk of outgassing in enclosed packages Most require moderate to long cures (1-2 h) Limited thermal stability Finite absorption of moisture Made with proprietary formulations which makes companies reliant on suppliers

1.5 Compositions of ICAs

ICAs formulations typically include a polymeric resin, curing agent, catalyst, conductive fillers and various additives. These additives include antioxidants, corrosion inhibitors, adhesion promoters, rheological additives and surfactants to enhance wetting.

1.5.1 Polymeric matrix formulations

In ICAs the polymeric matrix is used to mechanically bind the composite, providing structure and adhesion necessary to form interconnection. ICAs have been formulated with both thermoplastic and thermosetting resins.

Thermoplastic polymers are polymers that are solid below their glass transition temperature (T_g) but flow at temperatures above T_g. For use as ICAs, thermoplastic polymers must have a sufficiently high T_g to avoid creep and loss of adhesion during thermal cycling associated with typical use. On the other side, the T_g must be sufficiently low to enable easy processing and prevent damage to the chip carrier during assembly. Conventionally, polyimide has been used as the thermoplastic of choice for ICAs. Thermoplastic elastomers are ideal for applications where processing is difficult and/or reworkability is mandatory. However, there are a few significant drawbacks of using thermoplastic ICAs. First, as you approach the T_g, the polymer begins to flow, leading to poor adhesion. Secondly, to process thermoplastics ICAs with very high T_g typically requires the use of volatile plasticizers and/or solvents. During processing these volatile components evaporate creating voids. These drawbacks of thermoplastic elastomers make fabrication of reliable, highly conductive interconnects difficult.

Thermosetting polymers are polymers that following curing form a three-dimensional (3D) interconnected network such that the entire polymer can be considered one large molecule. Because a 3D network is formed from small pre-polymers/oligomers, the viscosity of the uncured thermoplastic ICAs is typically much lower than thermoplastic ICAs. The lower viscosity of uncured thermoplastic resins makes processing by screen or stencil printing easier and possible at ambient temperatures. There are many thermosetting resins that have been used in ICAs but epoxy resins are by far the most common. Epoxy resins have been the matrix material of choice because of their excellent adhesion, good thermal stability, commercial availability and their common use in industrial processing. Besides epoxy, many other thermosetting resins have been used to prepare ICAs. These include silicones [16], cyanate esters [17], polyurethanes [18], etc.

These molecules can be blended or formulated to obtain application specific polymer and composite properties. For conventional ICA applications an ideal polymeric matrix should have a long shelf life and working time, fast cure at low temperatures, high Tg, low absorption of volatiles, good adhesion and high impact toughness [14]. A table comparing the properties of different polymeric matrixes for ICA applications is shown in Table 3.

Table 3. Comparison of adhesive matrixes for ICA applications [19].

Materials	**Advantages**	**Disadvantages**
Epoxies	Thermally stable Good moisture and chemical resistance High purity Low outgassing	Long cure cycles with anhydride hardeners; Degassing required for two-component systems Large exotherm when amine-cured
Silicones	Highest purity Stress absorbing High and low temperature stability Low temperature cure Stretchable and flexible	Migrates to other circuit elements Low surface energy Swelled by non-polar solvents Low Tg Large CTE
Polyurethanes	Good flexibility at low temperatures Stress absorbing Highly versatile chemistry	Lower thermal stability and service temperature (150-163 °C) Moderate bond strength
Polyimides	Higher temperature stability High ionic purity Reduced bleedout	Trapped solvent can produce voids under large ICs Requires multi-step curing to volatilize solvent High-stress materials May absorb moisture in cured condition
Cyanate esters	High adhesion strength High thermal stability High T_g Low CTE	High-moisture absorption Popcorn susceptibility

1.5.2 Chemistry of epoxy ICAs

Epoxy resins and hardeners typically cure under specific conditions: temperature, UV excitation, microwave, moisture, etc. During the curing process, the mechanism of interaction between the molecules changes from van der Waals to covalent, resulting in an internal compressive stress on the composite. This compressive stress causes the conductive fillers to be pushed closer together during the curing process, increasing

contact between fillers. This increased contact improves the electrical conductivity of the composite [12].

To obtain strong adhesion, coupling agents are typically used. These coupling agents enable the formation of covalent bonding between the surfaces of the chip and the adhesive. Because thermally stable covalent bonds form between the substrate and the polymer matrix, ICAs formed with epoxy matrixes are not reworkable [20, 21].

The most commonly used epoxy resin formulation uses diglycidyl ether of Bisphenol F (DGEBF) resin, a carboxylic anhydride 4-methylhexahydrophthalic anhydride (MHHPA) hardener and 1-cyanoethyl-2-ethyl-4-methylimidazole (2E4MZCN) (Figure 3A-C). This formulation has been chosen because it has excellent mechanical properties, is nearly stress-free following curing, has a low exotherm, low moisture absorption and high shrinkage [22]. The main disadvantage of this system is that it requires relatively high curing temperatures >120°C and long curing durations ~1 hour [22].

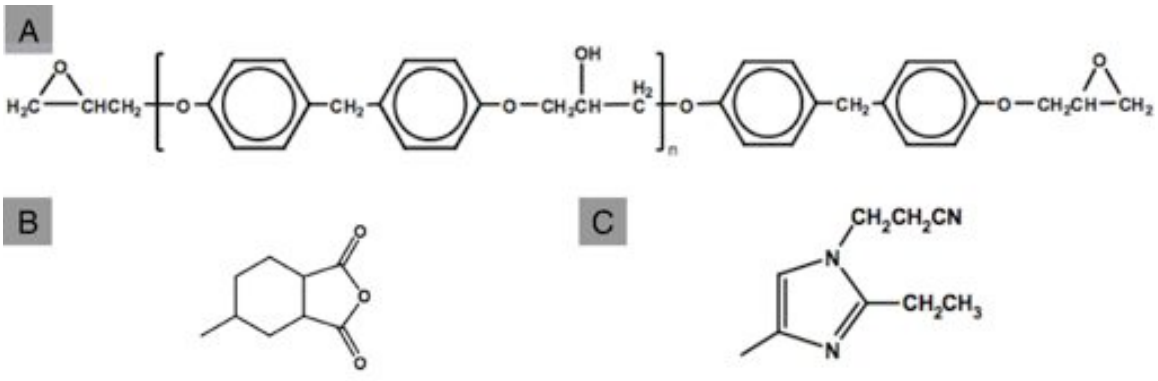

Figure 3. Molecular structures of A. DGEBF B. MHHPA C. 2E4MZCN

The curing mechanism of these epoxy-anhydride systems is still unclear due to the large number of reactions that can occur both competitively and synergistically [22-

29]. There are two proposed mechanisms for the curing of this epoxy resin. First, the 2E4MZCN catalyst can react with an epoxy group on the DGEBF to form a zwitterion with an alkoxide anion and a quaternary nitrogen (Figure 4D). The alkoxide anion can react with the anhydride group on MHHPA, producing a carboxylate anion (Figure 4E). There are two competing reactions involving the carboxylate anion. First, the carboxylate anion could react with an epoxide group, generating a new alkoxide anion (Figure 4F). Or, esterification between the hydroxyl group on the epoxy resin and the alkoxide can occur (Figure 4G). Fischer proposed a second mechanism which has become more widely accepted [24, 25]. In this mechanism the tertiary amine, which is a Lewis base, reacts with the anhydride to form a zwitterion containing a quaternary nitrogen and a carboxylate anion (Figure 4H). The carboxylate anion can then react with an epoxide group (Figure 4I) or undergoes esterification with a hydroxyl group either on an anhydride or on DGEBF. If the carboxylate anion reacts with an epoxide, generating an alkoxide anion this anion then reacts with MHHPA. The reaction of MHHPA generates a new carboxylate anion allowing the covalent network to be formed (Figure 4J). Termination occurs through the combination of two living polymers (Figure 4K). A third uncatalyzed mechanism proposed by Fish et al. also can occur [24, 25]. In this mechanism, the hydroxyl group on the DGEBF opens the anhydride, producing an ester group and a carboxylic acid group (Figure 4A). The carboxylic acid can react with an epoxide group to form a di-ester-alcohol (Figure 4B). This process can continue by alternating addition of MHHPA and DGEBF or by esterification. This process will continue until termination occurs via a condensation reaction of a carboxylic acid and a

hydroxyl group (Figure 4C). Typically optimal mechanical properties of the resin are obtained when the formulation contains 0.85 molar equivalents of anhydride [30].

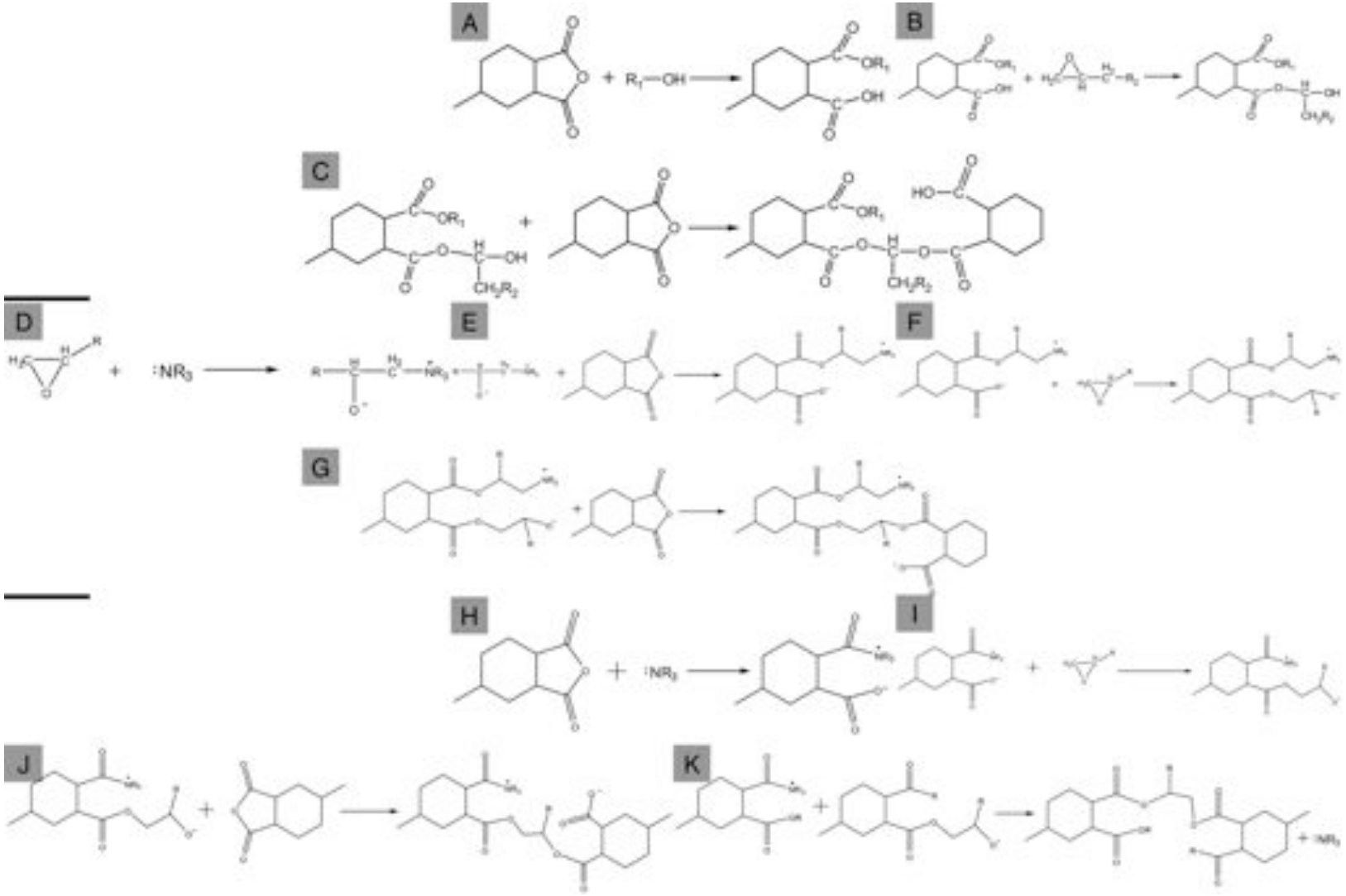

Figure 4. Catalyzed epoxy anhydride curing mechanism

1.5.3 Chemistry of silicone ICAs

Silicones, due to their unique set of properties have found use and application where organic polymers could not suffice. In electronic packaging silicone gels have been a mainstay material for low stress hermetic packaging of electronic components and as potting material for electronic devices. Silicones unique properties are derived from its unique structure. Unlike most polymers whose backbone tends to be composed of only organic constituents (C, N, O, S, P, etc.), silicones or more generally siloxanes are hybrid materials whose backbone consists of inorganic (Si) and organic (O) constituents. The most commonly utilized silicone polymer is poly(dimethylsiloxane) (PDMS) (Figure 5).These unique and beneficial properties include: excellent thermal and environmental stability, ozone and oxidation resistance, low electrical conductivity, high breakdown voltage, low dielectric constant, good flexibility at low temperatures, very low T_g, T_c and T_m, low activation energy for viscous flow, high gas permeability, good elasticity, low surface energy, good solvent and oil resistance, physiological inertness, can be cross-linked using a variety of methods at ambient and elevated temperatures, has tunable surface properties, is hydrophobic, easy to chemically functionalize and can replicate surface features with nanometer scale resolution and high aspect ratio. A list of some of the common properties of commercial PDMS elastomers is shown in Table 4.

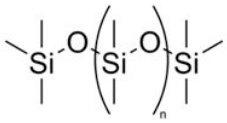

Figure 5. Molecular structure of PDMS

Table 4. Material properties of commercial silicones [31-33].

Materials	Sylgard 184	RTV 615
Color	Transparent	Transparent
Resin viscosity (mPa s)	3900	4300
Shore-A hardness	50	44
Tensile Strength (MPa)	-	6.5
Elastic Modulus (MPa)	1.8	-
Thermal Conductivity (W m^{-1} K^{-1})	0.18	0.2
Thermal Expansion Coefficient (μm m^{-1} K^{-1})	310	270
Dielectric Breakdown (kV mm^{-1})	21.2	19.7
Dielectric Constant	2.65	2.7
Resistivity (Ω cm)	$1.2x10^{14}$	$1.8x10^{15}$

These unique properties of PDMS are the result of its atypical chemistry, intermolecular and intramolecular forces. PDMS's high temperature and chemical stability results from the high bond energy associated with the Si-O bond (621.7 kJ/mole), ~100 kJ/mole more than a typical C-C bond [34]. Furthermore, the Si-O backbone is highly flexible, having a rotational potential energy of (3 kJ/mol), compared to the rotational bond energy of hydrocarbons of (14 kJ/mol) [35]. This low rotational potential energy of PDMS makes it have one of the lowest known polymeric glass transition temperatures, between -123°C and -54°C [36].

Despite these excellent properties, silicone elastomers typically have very low modulus, resilience and tear strength [36, 37]. To enhance the mechanical properties of silicones, Polmanteer et al. showed that by blending polymers with a high and low degree of functionality that loss mechanisms during failure, tear strength and modulus could be increased [38, 39]. However, the mechanical properties of this silicone are still insufficient for most applications. To produce silicones with sufficient mechanical properties requires the incorporation of particulate fillers. Reinforcing fillers can be used to increase tensile strength, tear strength and abrasion resistance, providing a several-fold

enhancement compared to virgin resins [40]. The most common fillers used are colloidal silica. The reinforcement capability of silica fillers is highly dependent on the particles surface area and the van der Waals and hydrogen bonding between fillers and polymer [41]. Comparative studies have found that fumed silica, produced by flame annealing droplets of amorphous silica, are more efficient to reinforce silicones than amorphous silica [42]. The improved reinforcement capability of fumed silica was correlated to a difference in surface chemistry. In fumed silica there are randomly distributed isolated hydroxyl groups which can covalently bond to silicone; conversely, amorphous silica have surfaces containing short poly(silic acid), which cannot covalently bond to silicone [43, 44].

Elastomeric networks of silicone have highly versatile chemistry and structure of the precursor resins. Typically industrial silicones have been stratified into four primary types: high temperature vulcanizing (HTV), liquid rubber (LR), room temperature vulcanizing 1 (RTV-1) and 2 (RTV-2). Where the difference between RTV-1 and RTV-2 is that RTV-1 is a one-component system that cures when exposed to moisture. On the other hand, RTV-2 is stable until mixing parts A and B together. The most prominent difference between silicone rubbers classified as HTV, RTV and LR is the viscosity and molecular weight of the polymeric precursors. The basic properties of the polymeric precursor are shown in Table 5

Table 5. Commercial forms of silicone elastomers [45].

Silicone elastomer	Polymer viscosity (Pa s)	Chain length (SiO_2) units
HTV-solid	20,000	6,000
RTV-1 and RTV-2 - liquid to paste	0.1-20	<800
LR- paste like	5-100	<1,000

These silicone resins are typically cured via one of three curing mechanisms: Peroxide cure, condensation cure or hydrosilylation.

Peroxide-cured silicones

PDMS can be cured by peroxide catalyst via one of two mechanisms. Curing initiates when a peroxide catalyst undergoes homolytic cleavage producing free radicals (Figure 6-1). These radicals can either abstract hydrogen from a methyl group on the PDMS (Figure 6-1), forming ethylenic linkages between siloxanes (Figure 6-4). Or more efficiently, the free radicals can react with vinyl functional groups on PDMS (Figure 6-3). Once the free radical is formed on or adjacent to the vinyl group the radical can attack another vinyl or methyl group forming crosslinks (Figure 6-4, 5). Termination occurs via coupling of two radicals or through hydrogen abstraction from a peroxide molecule. Silicones, which undergo peroxide cure, can react at a wide variety of temperatures depending on the decomposition temperature of the peroxide catalyst used. Peroxide cured silicones are commonly preferred by industry because of their longer shelf life and lower cost than other types of silicone elastomers. However, there are some disadvantages to peroxided cured silicone rubbers. Peroxide cure rubbers tend to yellow

after curing, smell during production, smell and taste bad and leave peroxide residues in the rubber.

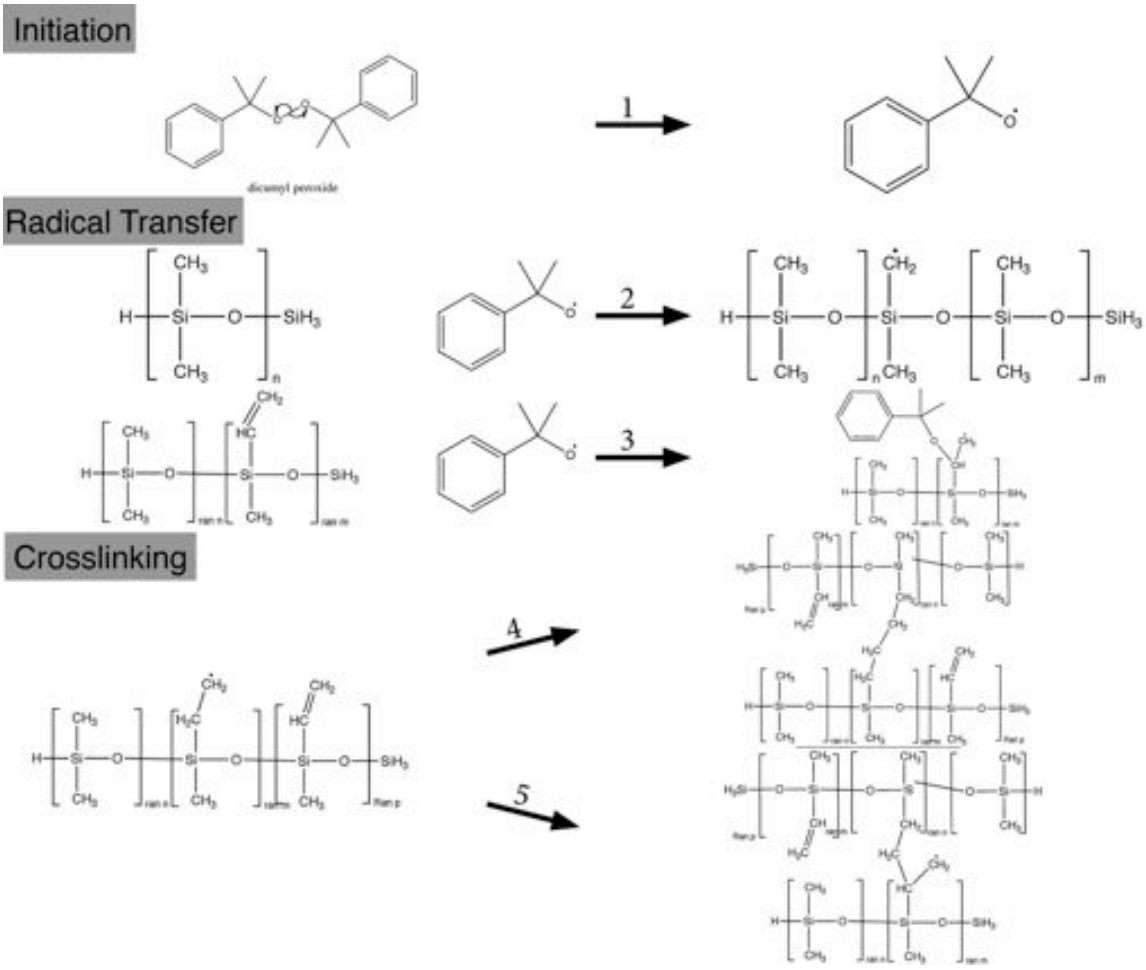

Figure 6. Crosslinking mechanism of peroxide cured silicones.

Condensation-cure silicones

Condensation cure silicones react by condensation of silanol groups to form siloxanes. To avoid problems associated with self-condensation and form a 3D cross-linked network formulations contain multifunctional cross-linkers containing alkoxysilanes, acyloxysilanes, silicone hydrides or ketoximinosilanes [34]. To hasten the rate of this reaction Sn catalysts are typically used. Activation of the Sn catalyst requires

the partial hydrolysis of Sn by water, thus the reaction tends to be initiated by water. The condensation curing reaction can be described as shown in Figure 7.

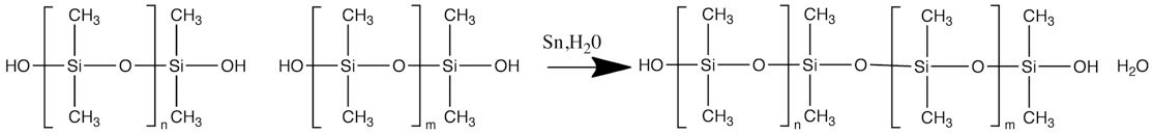

Figure 7. Sn catalyzed condensation reaction.

For RTV-1 condensation cure silicones water is absorbed from the moisture in the air catalyzing the curing mechanisms. On the other hand, RTV-2 condensation cure silicones are sold in two part mixtures where one component contains water. This system is useful because it is very easy to control the crosslink density and functionality of the elastomer by controlling the crosslinkers used. The large quantity of volatiles generated during the curing process leads to a volumetric shrinkage following cure of 0.2-2% [45]. This shrinkage can enhance conductivity of ECAs formulated with condensation-cured silicones. However, there is currently no published literature discussing the fabrication of ECAs or electrically conductive composites (ECC) using condensation-cured silicones with low resistivity ($<1x10^{-3}$ Ω-cm). It is likely that condensation cure silicones have not be used to formulate ECC because the reaction tends to revert at temperatures >90°C if not completely reacted and because exposure to moisture at elevated temperatures can oxidize metallic surfaces [45].

Hydrosilylation-cured silicones

Hydrosilylation involves a reaction between a silicone hydride and an olefin, creating an alkylenic linkage. The most commonly used olefins are vinyl functionalized silicones. 3D silicone networks can form when multifunctional silicones hydrides and

vinyl-functionalized silicones are reacted. Hydrosilylation reactions are catalyzed by group 8-10 metals, the most common of which is platinum complexes like platinum-divinyltetramethyldisiloxane (Karstedt's catalyst) [46]. Platinum based catalysts are preferred because they react quickly and function at very low concentrations (1-2) ppm. The cross-linking process by hydrosilylation is shown in Figure 8A. The most commonly accepted mechanism for hydrosilylation of silicones was described by Chalk and Harrod [47]. However, recently there has been some small modifications made to the proposed mechanism to account for the induction period and the formation of platinum colloids [48]. This mechanism is shown schematically in Figure 8B. The main benefit of hydrosilylation-based cross-linking is there are no by-products produced and the only residue is a small volume of colloidal platinum. Because there are no by-products or volatiles there is no shrinkage during cure. The lack of shrinkage following curing is typically an advantage, however; for preparation of ECCs it is a disadvantage. To cause shrinkage in hydrosilylation-cured silicones curing must be done in the expanded state at elevated temperatures. PDMS which when cured at room temperature has negligible shrinkage can shrink >2% when cured at 100°C. This shrinkage is only slightly less than typical epoxies which exhibit a shrinkage of ~3.8 vol% following cure [32, 49, 50].

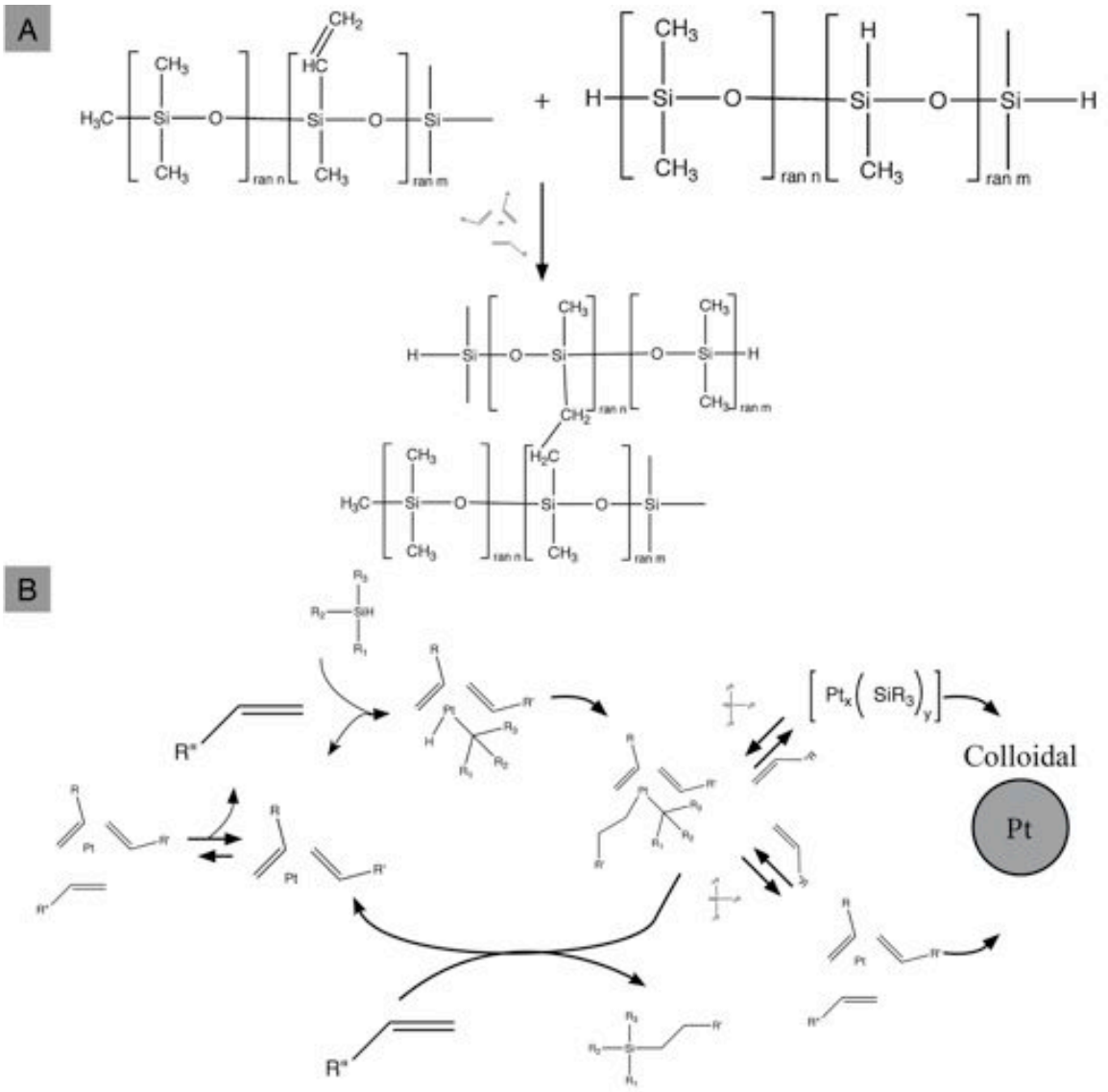

Figure 8. A. Hydrosilylation cross-linking in the presence of Pt catalyst. B. Catalysis mechanism of hydrosilylation by platinum based on Chalk and Harrod mechanism [47, 48].

1.5.4 Conductive fillers

Electrically conductive fillers are added to the polymer matrix to make the composite electrically conductive. Many fillers have been utilized to prepare ICAs these

include: silver (Ag), gold (Au), Copper (Cu), nickel (Ni), carbon in many different allotropes, etc. [51]. Moreover, to reduce the cost of metallic particles and increase CTE compatibility, many ICAs are formulated with glass or silica coated particles. The most commonly used conductive filler for high performance ICAs is Ag. Ag is used because it has the highest electrical (15.87 nΩ-m) and thermal conductivity (429 W m^{-1} K^{-1}) of any metal [51]. Equally important is that silver oxide has higher electrical conductivity than other metals commonly used except Au, which is cost prohibitive for use in ICAs. The main disadvantages of Ag-filled ICAs is that silver is electrochemically active and significantly more expensive than Cu and Ni. However, these low cost conductive fillers, Cu and Ni ICAs easily oxidize. Once oxidized the conductivity of the ICA is dramatically reduced. Even if corrosion inhibitors are used, Cu ICAs electrical conductivity is not stable during accelerated aging [52]. The reliability of Cu ICAs has been enhanced by coating the Cu particles with Ag, however due to incomplete coating of the Cu surfaces Ag-coated Cu ICAs are also unstable during aging [53-55]. Carbon materials such as carbon black [56, 57], graphite/graphene [58, 59] and carbon nanotubes (CNTs) [60-63] have been used as conductive fillers for ICAs. However, composites formed with carbon materials tend to have low electrical conductivity. To improve the electrical conductivity of conductive polymer composites, carbon materials have been coated with metals as fillers, such as Ag-plated CNTs [64, 65], Ag-plated carbon fibers [66], Ag-coated graphite [67-69], Ni-coated carbon fibers [70] and Ni-coated graphite [71]. In literature, conductive particles coated with a low melting temperature alloys (Containing Bi, In, Sn, Sb, Ga and/or Zn) have been used to enhance contact between conductive fillers [72-78]. Similarly, incorporation of small metallic nanoparticles with low melting points, due to

melting point depression resulting from their large surface area-to-volume ratio, have been used to sinter conductive fillers reducing contact resistance [79].

The shape and size of the conductive fillers play an intricate role in determining the properties of the ICA. Conductive fillers of various shapes and sizes have been investigated, including: micron-sized metallic flakes, nano- micron- sized spherical metallic particles, graphene (2D), carbon black, CNT (1D), carbon fiber, silver nanowires, etc. The aspect ratio of the fillers is the most influential geometric factor in determining the properties of the ICA. As the aspect ratio of the fillers increases, the percolation threshold decreases, reducing the volumetric filler loading necessary to achieve isotropic electrical properties. Furthermore, when the percolation threshold is reduced it is more likely that multiple conduction pathways exist for current flow, giving rise to reduced resistance. By reducing the percolation threshold, lower filler loadings can be used, improving the mechanical properties of the composite. This effect is most dramatic when using 1D fillers like carbon nanotubes or silver nanowires. The most common fillers used for ICAs are 1-20 μm metallic flakes. It is advantageous to use large flakes because they require fewer contacts to carry current a given distance, have a high aspect ratio, have lower viscosity than smaller sized particles, are inexpensive to fabricate and can be easily be dispersed in polymeric matrixes [80]. To enhance the packing density of Ag flakes, multi-modal or bi-modal flakes are typically used. The use of fillers with a distribution of sizes enhances contact area between flakes, reducing resistivity of the composite.

Dispersing surfactant-free micron-to-nanometer sized conductive fillers well in a polymer matrix is difficult. As the size of the fillers decrease it becomes increasingly

more difficult to prevent aggregation of the conductive fillers. To prevent aggregation and aid in dispersion of the conductive fillers surfactants are used. These surfactants, typically fatty acids, act as compatibilizers between the conductive filler and the polymeric matrix. The lubricant despite aiding in dispersion reduces electrical contact between the conductive fillers. It is important to choose an appropriate surfactant to prevent aggregation without any detrimental effects on the electrical properties of the final composite. Lu et al. investigated the thermal decomposition of surfactants on the surface of silver flakes [81, 82]. They found that thermal decomposition temperature and the onset temperature of the exothermic peak in DSC is proportional to the chain length of the surfactant. Furthermore, they found that the lubricant bonds to the surface by forming a Ag-salt between the surfactant and the Ag surface. The presence of these lubricants is essential to disperse the silver flakes; however, as the chain length of the surfactant increases metallic contact is reduced and tunneling resistance is increased. Thus, in an ideal formulation surfactants are removed during the curing processes, prior to reaching gelation.

1.6 Processing of ICAs

1.6.1 Printing processes

Since ICAs are isotropically conductive, to create desired interconnection without shorting requires that the adhesive be patterned. For flipchip applications it is desirable to pattern ICAs into bumps. Methods to form patterned ICA bumps should be rapid, highly reproducible and have fine pitch. The most common methods for printing ICAs is screen-printing and stencil printing. In screen-printing, ICA is printed through a metallic mesh

to form ICA bumps on pads. On the other hand, in stencil-printing process a metallic stencil is used to selectively print ICA bumps on pads. The difference between these two processes is that in stencil printing the metallic stencil is in intimate contact with the substrate; while in screen-printing processes a patterned metallic mesh floats slightly above the surface of the substrate. Stencil-printing and screen-printing processes are shown in Figure 9. These stencils/meshes are generally fabricated by etching, electroforming, or laser drilling are capable of obtaining micro-scale resolution. During the printing process, a squeegee is used to push ICA through a designed stencil or mesh. As the stencil/mesh lifts away from the substrate, the patterned ICA paste remains. The ICA bumps that are formed via the screen-printing process can be either fully cured bumps or pre-cured (B-stage) for thermosetting polymers or alternatively can undergo a bakeout to remove residual solvent in thermoplastic ICAs. The bumps formed during this process are typically 50–75 μm. This process can create bumps with pitch as fine as 125 with bump densities up to 80,000 bumps/wafer. Once wafers are bumped and diced, wafers are flipped over and bonded to carrier chips. The bonding process is dependent on the material properties of the adjoining bumps. Following bonding, epoxy-based underfill material is injected into the gap between the chip and the carrier for mechanical reliability and hermetic encapsulation.

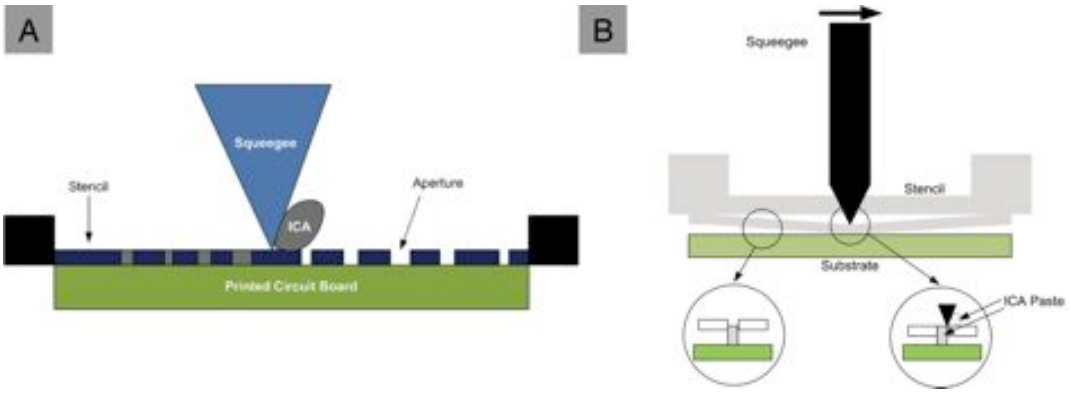

Figure 9. Image showing A. Stencil printing process. B. Screen printing process [83]. Reprinted with permission of John Wiley & Sons, Inc.

Recently, there has been significant effort to use ink-jetting technology to print ICAs. In this process ICA is diluted in a solvent and dispensed through a small nozzle onto the surface of a substrate. Ink-jet printing processes are ideal for printing ICAs because they have high throughput, can easily be adapted to small-scale production and are single step additive processes which reduce the cost and complexity of processing. Despite the benefits of ink-jet printed technologies there are many challenges that still need to be solved. The greatest challenge is creating an ink that has sufficiently low viscosity to enable printing of small drops while at the same time being conductive enough to be used as an interconnect. Highly conductive ICAs typically contain a high concentration (>70 wt%, >25 vol%) of large metallic particles resulting in a thick paste with a viscosity of ~25,000 cP at 25°C. To circumvent the issue of high viscosity in polymeric ICAs most commercial inks contain metallic nano-particles dissolved in a solvent containing only minimal polymeric binder. Once printed, the solvent is evaporated and the film is annealed at temperatures between 100-200°C. During the annealing process the nanoparticles sinter due to their high surface energy. Following the

sintering process the produced films have bulk resistivity of <2.5x10-6 Ω-cm, only an order of magnitude higher than bulk silver [84]. Recently it has be shown that sintering of silver nanoparticles can be induced at room temperature by exposing the nanoparticles to oppositely charged polyelectrolytes [85]. The major drawback of these polymer inks is that they do not contain enough polymeric binder to provide adhesion, thus are completely ineffective as an interconnect material. To produce inkjettable ICAs requires a careful balance of matrix composition, filler loading and shape to prevent aggregation, clogging of the nozzle as well as enable uniform droplet formation. The general material properties required to produce an inkjettable ICA are shown inTable 6. Currently it has been possible to inkjet print ICA with a drop size of 150 μm [86]. For inkjet technology to be used for interconnection in commercial devices will require increased conductivity and improved resolution capabilities.

Table 6. General materials requirements for ink-jet printable ICAs [86].

Viscosity	≤ 100 mPas
Conductive particle size	≤ 5 μm
Pot life at processing temperatures	1 hour
Curing profile	Drying step → curing step
Conductivity	10^{-4} Ω cm

1.6.2 Curing process of ICAs

The polymerization and crosslinking of ICA is a bulk polymerization process thus the viscosity of the polymer is dynamically changing throughout the curing process. Careful control of ICA viscosity during assembly is essential for obtaining highly reliable interconnects. Prior to crosslinking the ICA viscosity can be modeled by the Williams-Landel-Ferry model (WLF) Eq. 1, where C_1, C_2, T_r and μ_0 are empirical constants. As the reaction proceeds the polymer chains become longer. As the chain length increases it

becomes increasingly more difficult for the chains to slide across one another leading to an increase in viscosity. Once the reaction has preceded long enough the polymer crosslinks and is essentially a single molecule, no longer having fluid-like behavior. At this point in the reaction, the polymer transitions from fluid-like to solid-like behavior. This transition is called the gel point. Gelation is typically reached when 55-80% of the reaction has occurred [51].

$$\mu(T) = \mu_0 \exp\left(\frac{-C_1(T - T_r)}{C_2 + T - T_r}\right) \quad (1)$$

Following the gel point the reaction proceeds at a reduced rate, as the mobility of the molecules is reduced. Eventually the molecular mobility is so low that the molecules are no longer able to react; this phase of the reaction is called vitrification. The curing process of thermosets is typically described by Time-Temperature-Transformation (TTT) diagrams. A typical TTT diagram is shown in Figure 10. On this diagram, T_{g0} is the glass transition temperature of the uncured resin, Gel T_g is the temperature where vitrification and gelation occur simultaneously and $T_{g\infty}$ is the temperature where the polymer completely cures. When ICAs are cured, it is advantageous to have multiple curing stages. The first heating stage is used to reduce the viscosity of ICA enabling it to wet the surface, while the second stage is used to cure the resin. To obtain ideal mechanical properties of the resin it is essential that the TTT diagram is known to avoid vitrification. An ideal curing profile is shown by the blue line in Figure 10.

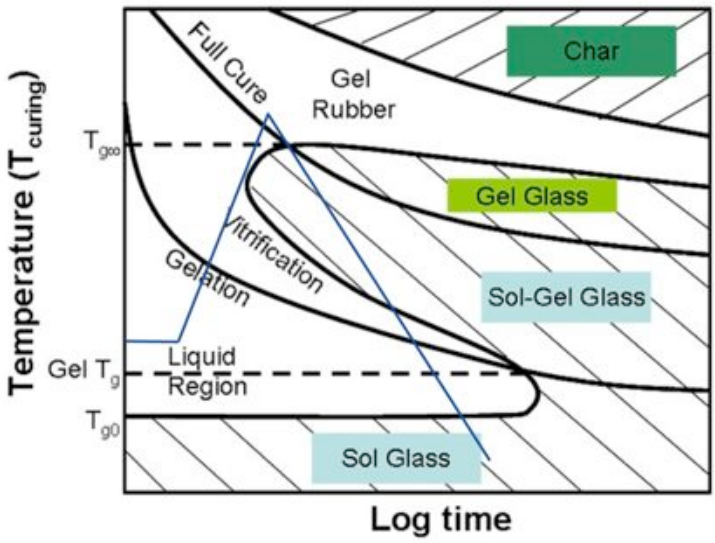

Figure 10. Time temperature transformation (TTT) diagram [87]. Blue line indicates ideal ICA curing profile.

1.7 Processing of anisotropically conductive and non-conductive adhesives

The increased performance, frequency and form factor of modern microelectronic devices requires low cost, environmentally friendly and simple solutions to create low profile, ultra-fine pitch interconnects. Two frontrunners, Anisotropic Conductive Adhesive/Film (ACA/ACF) and Non-Conducting Adhesive/Films (NCA/NCF) have become the most popular candidates for research and development of new ultra fine pitch (<40μm) interconnect materials. ACFs films are prepared by taking deformable submicron to micron-sized particles and suspending them within a polymer matrix, solvated with a highly volatile organic solvent. Thin films of these materials are prepared via a bar coating process. In the bar coating process, a squeegee is used to prepare a thin film of specified thickness, typically less than 50 μm. The formed films have particle filler loadings less than the percolation threshold, thus are insulating. Following solvent

evaporation, the films are pre-cured on the bumps, where interconnection is to be made. A chip, onto which interconnection is going to be established, is interconnected by flip chip bonding at elevated pressures (<300 MPa) and temperatures (>150°C). Upon completion of the bonding process, interconnection is achieved through unidirectional conductivity resulting from particles trapped between the two bumps. No additional processing, underfill or reflow is needed, eliminating costly processing steps and improving device reliability. NCF interconnections are manufactured and processed similarly to ACF films, except no conductive particles are incorporated into the polymer film. Electrical connection in NCF is established through contact between small asperities on the surface of the metallic bump. Because NCF is not intrinsically conductive these materials do not need to be patterned onto the bump surface, reducing the complexity and cost of processing. Because of the facile processes to form larger area interconnects with ACF/NCF, these ECAs are commercially used in a wide range of low powered, large area commercial devices such as smart cards and liquid crystal displays [88].

Despite the numerous advantages of interconnects based on NCF and ACF technologies, they have limitations that limit their use as interconnects for high-powered devices like microprocessors. Compared to metallurgical solder joints, ACF and NCF have restricted contact area and poor interfacial bonding. These inferior properties result in lower electrical conductivity, poorer reliability, reduced current carrying capacity and reduced impact strength compared to solder interconnects [89, 90].

Current standards of ACF/NCF have conductivities and current carrying capacities orders of magnitude lower than metallic solders [12, 89-91]. To achieve high conductivity and current carrying capacity requires careful control over the film

thickness, curing temperature, cure kinetics and viscosity. In the ideal case, as the IC is thermo-compression bonded the epoxy viscosity should drop. This reduction in viscosity during heating will enable the polymer to be completely displaced from the interface. Furthermore, the metallic particles should deform to maximize contact. Once contact between the bumps and particles is established the epoxy resin should rapidly cure to avoid vitrification. If all these criteria are met the interconnect will have ideal electrical properties, adhesion, mechanical strength and toughness.

Currently, the greatest challenge limiting ACF/NCF use for large area high density interconnects is the CTE mismatch between the IC and the organic substrate. This CTE mismatch results in large internal stresses, which becomes increasingly large as the die size is increased. Improved design of NCF and ACF materials will enable ACF/NCF to be used as simple, large area, ultra fine pitch interconnects for high-powered electronics.

1.8 Electrical conduction mechanism in ECCs

The origins of electrical conductivity in electrically conductive polymer composites (ECC) are typically described in terms of percolation theory. This theory states that at some specific volume fraction of filler of a specific aspect ratio that a continuous network is formed. This fundamental description is purely based on establishing mechanical contact between fillers. In ECAs percolation is defined as the filler loading when the conductivity of the composite dramatically increases until eventually reaching a plateau [7]. In Ag flake filled ICAs percolation threshold tends to be reached around at filler loadings around 16 vol%. It has been assumed that following

percolation the particles are in direct metallic contact [7]. A schematic plot and a schematic drawing of a percolated network is shown in Figure 11A and B respectively.

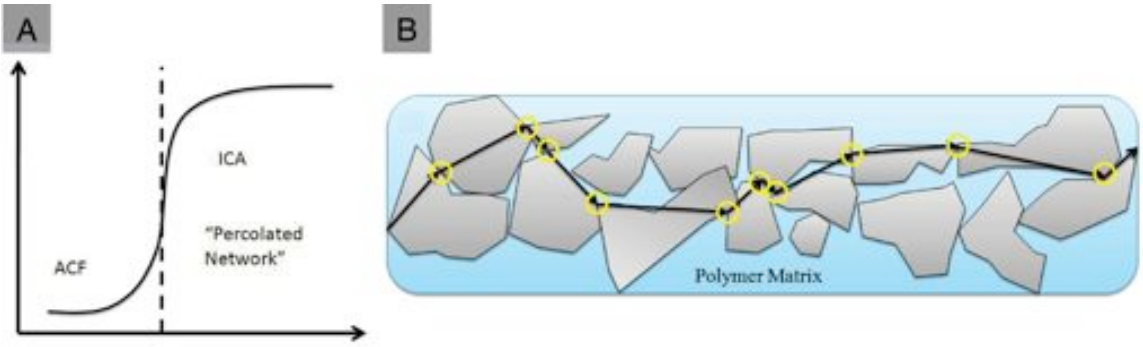

Figure 11. A. Schematic plot showing transition from non-conductive to conductive percolated network. B. Schematic representation of a percolated network of conductive fillers in a polymeric matrix.

1.8.1 Modeling electrical conduction in ECCs

Modeling the electrical conductivity of ECAs requires careful and detailed understanding of the composites formulation, processing and properties. Classically, the conduction pathway has been discussed in terms filler resistance (R_f) and the contact resistance (R_c). Contact resistance has been defined in terms of two key components, constriction resistance (R_{CR}), resulting from current being constricted to flow through the small area of contact between conductive fillers, and the tunneling resistance (R_t), resulting from tunneling of electrons between thin polymeric layers (<5nm) or surfactants coating on the conductive fillers. Using this interpretation most published literature defines the total resistance as shown in Eq. 2 [6, 92-97].

$$R_{total} = R_f + R_{CR} + R_T \quad (2)$$

Where

$$R_f = \frac{\rho}{\pi d} \ln \frac{d + \sqrt{d^2 - D^2}}{d - \sqrt{d^2 - D^2}} \tag{3}$$

$$R_c = \frac{\rho}{d} \tag{4}$$

$$R_t = \frac{\rho_t}{\pi(\frac{d}{2})^2} \tag{5}$$

Where ρ is the bulk resistivity of the silver, d is the particle diameter, D is the contact diameter and ρ_t is the tunneling resistivity. In this model, the film resistance is typically described in terms of the Simmons model. In this model, tunneling occurs between two similar metals separated by a thin insulating film [98]. Based on the Simmons model, Holm and Kirschestein described the conductivity due to tunneling as a function of the film thickness in Å (s), work function (Φ) and dielectric constant ε_r of the film, as shown in Eq. 6-8 [12, 98-102].

$$\rho_t(s, \Phi, \varepsilon) = \frac{10^{-22}}{2} \frac{A^2}{1 + AB} e^{AB} \tag{6}$$

$$A = 7.32 \times 10^{-5} (s - \frac{7.2}{\Phi}) \tag{7}$$

$$B = 1.265 \times 10^{-6} \sqrt{\Phi - \frac{10}{s\varepsilon}} \tag{8}$$

From this model it is rather intuitive that decreasing the tunneling gap will dramatically increase the conductivity of the ECA. There are many factors that control the tunneling gaps. These factors include: Physiochemical enthalpy and entropy of adsorption, Oxide thickness, filler loadings, particle and polymer surface energy, surfactant (length, structure, packing), cure shrinkage, etc. [95, 96]. Experimentally, it has been proposed that the tunneling gap is anywhere between 10 to 100 Å [95, 96]. Jackson, et al. used the model proposed by Holm to predict the thickness of the insulating

layer. They found that the dielectric film thickness at the interfaces was 5.96 Å under the assumptions that Φ was 4.75 eV and ε_r was 4.2 [101, 103].

Discrepancies with published models

Despite the numerous citations of publications proposing the model of electrical conduction in ECAs described by Eq. 2, there are a few obvious flaws with this model. The most obvious is that this model assumes that constriction resistance and tunneling are series processes. Instead, conduction via tunneling and direct metallic contact happen simultaneously; thus are parallel processes. A more precise model of the conduction pathway between a single particle contacts is shown graphically in Figure 12 and numerically in Eq. 9.

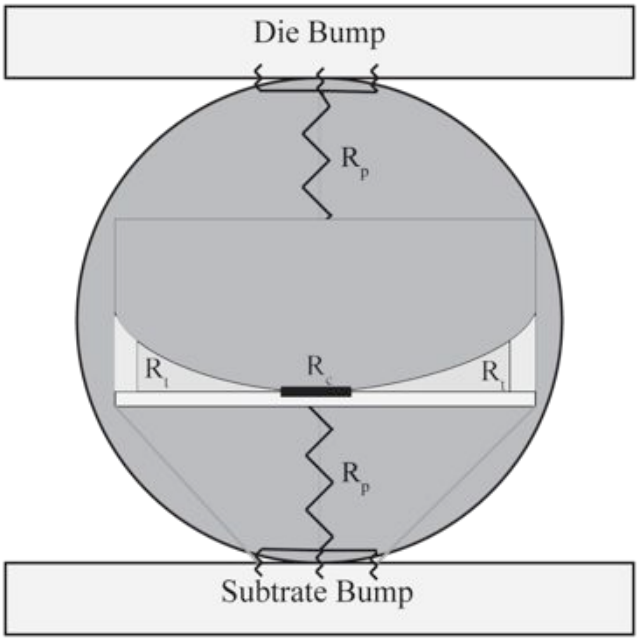

Figure 12. Schematic drawing showing circuit diagram of a single particle trapped between bumps in a single ACF interconnect. Inset shows regions where current flow occurs through a constricted metal contact and tunneling [104].

$$R = \sum \left[\frac{1}{R_{cr}} + \frac{1}{R_t}\right]^{-1} + R_p \quad (9)$$

Based on the previously described conceptual understanding of the interface, it is inconceivable that the insulating film is only 5.96Å thick, as determined by Jackson, et al [101, 103]. This would correspond to only ~5 fully extended carbon-carbon single bonds. Such an extremely thin dielectric layer between fillers is unrealistic. Metallic particles, treated with short chain surfactants, have a thin insulating layer on the order of 11-20 Å. This theoretical interface thickness is calculated without assuming any adsorbed or trapped polymer at the interface. Given the inconceivable thickness of the calculated interface, it is likely that the tunneling mechanism proposed by Simmons does not apply to contacts between conductive fillers. Instead, it is highly probable that a more complex through bond electron transport mechanism is responsible for the high conductivity in ECCs.

The model of electron tunneling presented by Simmons describes electron transport via a process of direct, coherent tunneling. A necessary condition for coherent tunneling is that the wavefunctions of the two metallic electrodes are continuous. Coherent tunneling processes occur in one discrete event. The strong spatial dependence of coherent tunneling means that it is generally insignificant at long distances (>25Å) [105]. It is more probable that electrical conduction in interconnects occurs through incoherent tunneling mechanisms. The incoherent tunneling model assumes that electrons undergo a series of coherent tunneling events, where the probability of each tunneling event is determined by the depth of the potential well and the length of the barrier [106, 107]. Electron transport through incoherent tunneling mechanisms occurs through a series of short tunneling events. Since the probability of a series of short tunneling events

occurring is greater than the probability of a single tunneling event occurring over the same distance, conduction through incoherent tunneling mechanisms have a decreased dependence on the length of the tunneling gap. The reduced spatial dependence of incoherent tunneling mechanisms allows electron transport over longer distances than transport via coherent tunneling mechanisms.

A second long range electron transport mechanism that likely participates in electron transport in ECC is hopping. Hopping mechanisms rely on molecular reconfiguration, altering the energy states of the molecules, promoting a series of tunneling events, eventually leading to conduction [105, 108-114]. Depending on the molecular structure, order and mobility of the molecules hopping conduction can occurs via localized states. Localized states are states where the wavefunctions are localized, decaying exponentially as it propagates away from its source. Schematic drawing of tunneling processes via extended and localized states is shown in Figure 13A-B respectively. The presence of disorder in insulating materials permits localized energy states to exist within the forbidden band gap. The existence of localized states within the band gap enables conduction via hopping mechanisms [109, 111]. Since the density of states is highly dependent on molecular order, intermolecular order, crystallinity and defects play a significant role in controlling the rate of hopping conduction. The hopping rate between sites i and j (υ_{ij}), can be described by Eq. 10, where where υ_0 is dependent on the electron transport mechanism, r_{ij} is the distance between sites i and j, α is the localization length and $\varepsilon_i(\varepsilon_j)$ is the energy at the localized state i(j) [108, 115]. Additional possible contributing mechanisms of through film conduction as well as their temperature, field and spatial dependence is shown in Table 7. Despite the understanding

of electron transport mechanisms independently, it is very difficult to correlate these theories to complex engineering systems, where electron transport processes occur competitively and synergistically. Future models will need to consider these additional conduction pathways.

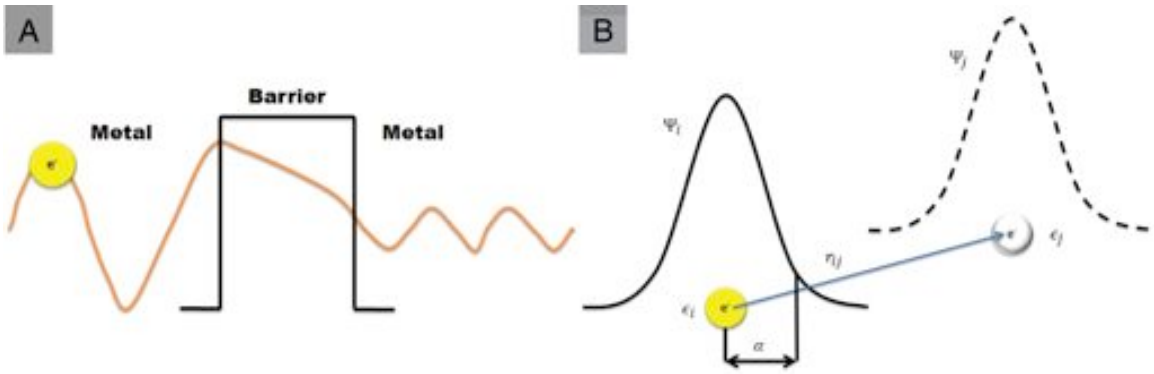

Figure 13. Schematic drawing of electron transfer via an A. Extended state B. Localized state

$$v_{ij} = v_0 \, exp\left(-\frac{2r_{ij}}{\alpha}\right) exp\left(-\frac{|\varepsilon_i - \varepsilon_F| + |\varepsilon_j - \varepsilon_F| + |\varepsilon_j - \varepsilon_i|}{2kT}\right) \quad (10)$$

Table 7. Possible through film electron transport mechanisms that contribute to tunneling resistance in ECCs [105].

	Temperature Dependence	**Voltage Dependence**	**Film Thickness Dependence**
Coherent Tunneling	none	linear (low V)	exp(-βd)
Incoherent Tunneling	none	linear (low V)	exp(-cd)
Hopping	exp(-α/T)	linear (low V)	d-1
Poole-Frenkel effect	exp(-α/T)	exp(bV1/2)	exp(-cd1/2)
Thermionic (Schottky) emmision	exp(-α/T)	exp(bV1/2)	exp(-cd1/2)
Fowler-Nordhiem	none	V2exp(-b/V)	exp(-cd)

1.8.2 Methods to increase electrical conductivity of ECC

The presence of polymeric binders and limited contact area between conductive fillers make them intrinsically less conductive than metals or metallic solders. Since, the electronics packaging industry is diligently researching new ways to decrease the disparity between ECC and metallic solders. The following section will discuss some of the methods recently used to enhance conductivity of ECC.

Incorporation of high aspect ratio or 1D fillers:

As previously discussed, the use of high aspect ratio or 1D fillers reduces the percolation threshold. This reduction in the percolation threshold results from a decrease in the minimum number of contacts necessary to transverse a distance. It was recently found that ICAs formed with Ag nanowires had a resistivity of 1.2×10^{-4} Ω-cm, at 56 wt% filler loadings [116-118]. It was hypothesized that the improved electrical conductivity was the result of increased contact area between fillers, fewer contact points required to form a percolated network, more stable contact between fillers and increased tunneling rates [116-118]. The ICA formed with Ag nanowires did not only perform better electrically but also mechanically. The shear strength of ICAs formed with silver nanowires on a aluminum plate was (17.6 MPa) compared to conventional ICAs formed with micron sized flakes (17.3 MPa) [118].

Similarly, multi-walled carbon nanotubes (MWCNT) have been incorporated into micron filled ICAs with filler loadings below the percolation threshold to induce percolation. It was found that through incorporation of <1 wt% of carbon nanotubes that the electrical resistivity and the percolation threshold of ICAs could be reduced [119].

However, their measured values for bulk resistivity are significantly lower than the state of the art. Moreover, others have found that the addition of carbon nanotubes into ICA formulations with metallic filler loadings greater than the percolation threshold have no impact on the conductivity of the composite [64]. In the same study it was found that by doping the CNT or by coating them with Ag the conductivity of the composite could be increased [64]. One of the greatest challenges when using high aspect ratio fillers is preventing their aggregation. Aggregation of these high aspect ratio fillers makes processing very challenging. Currently, the benefits associated with the use of high aspect ratio fillers do not yet justify tackling the processing challenges.

Low temperature sintering of nanoparticles

Metallic nanoparticles due to their high surface area compared to their volume have lower thermal stability than bulk metal. This instability enables these particles to melt and agglomerate at temperatures significantly lower than the melting temperature of the bulk metal. The ability of metallic nanoparticles to sinter at relatively low temperatures (<200°C) has enabled their use in printing of conductive traces [85, 120-124], metal-to-metal bonding [125] and electrical interconnection [126-133]. Recently, nanoparticle sintering has been used as a method to reduce contact resistance in ICAs. It was found that the incorporation of sinterable Ag nanoparticles near the percolation threshold tends to reduce the resistivity of the composite. This resistivity of the resulting composite is due to increased packing density and contact area between conductive fillers [134]. However, if the nanoparticles do not sinter the resistivity of the composite dramatically increases due to the increased number of contacts necessary for current to flow a given distance [126, 132, 134-136]. This observation was confirmed by Ye et al.

who showed through SEM studies how the incorporation of Ag nanoparticles reduces contact between micron-sized particles (large area contacts) and instead forms contacts via the incorporated nanoparticles (small area contacts); thus increasing contact resistance [135].

To properly produce ECCs with sinterable nanoparticles requires that the particles are very small (<2nm) and have a high surface energy. However, to disperse particles with such a high surface energy and area requires that the particles be coated with surfactants. These surfactants stabilize the surface therefore reducing the propensity of the particles to sinter. Jiang et al. investigated the effects of surfactant chemistry and chain length on the electrical properties of ICAs composed of Ag flakes and Ag nanoparticles [132]. Jiang et al. found that the most important parameters, which control the rate of sintering, is the chain length and the debonding temperature of the surfactant [132]. Following the optimization of the nanoparticle concentration and surfactant, a minimum resistivity of 5×10^{-6} Ω-cm was obtained [133]. Another key factor that controls sintering that has been commonly overlooked is the cure kinetics of the polymer matrix. To increase sintering it is desirable to slow the cure kinetics, allowing sintering to occur prior to gelation of the polymer.

A second mechanism of sintering in ICAs is low temperature transient liquid phase sintering (LT-TLPS). TLPS occurs when ECCs are prepared with a high melting point metallic powder and a metallic powder of a low-melting point alloy (Sn-Pb, Sn-In, Ga-In, etc.) [75-77, 137]. During LT-TLPS the low-melting-point powder forms an alloy with the high-melting point powder as the matrix cures, forming metallurgical connections. ECCs which undergo LT-TLPS have electrical and mechanical properties

comparable to metallic solders. Lu et al. showed that ICA formulations that undergo LT-TLPS had lower resistance and contact resistance than commercial ICAs [74]. Further details regarding this method of conductivity enhancement have been excluded for brevity, detailed description of LT-TLPS can be found in [138].

Increased polymer matrix shrinkage

Prior to the curing process ECC have extremely low conductivity and in most cases are insulating. However, following curing the bond mechanism within the resin changes, resulting in a compressive stress on the composite. This compressive stress causes the matrix to shrink. The shrinkage of the matrix brings the particles closer together increasing contact; improving the electrical conductivity of the ECC [139]. Since the shrinkage of the polymer is directly correlated to the crosslink density, ECCs with increased crosslinking density tend to have increased conductivity. This mechanism was confirmed through experiments where the percentage of tri-functional epoxy was increased from 2 wt% to 10 wt%; in doing so, the resistivity of the ICA decreased from 3.0×10^{-3} Ω-cm to 0.58×10^{-3} Ω-cm [140].

In-situ replacement / removal of surfactant on particle surfaces

Long chain surfactants on the surface of conductive particles are a necessary requirement to produce homogeneous conductive pastes [81, 82, 141, 142]. However, this lubricant decreases metallic contact and increases the tunneling/hopping barrier. In-situ replacement of long chain acids (stearic acid) with short chain molecules diacids (malonic acid) decreases the length of the tunneling gap, increasing conductivity of the composite. It was found that through the replacement of stearic acid with malonic acid

that the resistivity of the ICA decreased from ~7.3×10^{-4} to ~4.7×10^{-4} Ω-cm [143]. Similar results were demonstrated using aldehydes, resulting in a decrease in bulk resistance from ~7.3×10^{-4} to 6.0×10^{-5} Ω-cm [144]. It was proposed that the increased performance of ICAs with aldehyde additives resulted from the removal of stearic acid from the surface of the silver flakes and from the reduction of silver oxide [144].

1.8.3 Concluding remarks

Conduction mechanisms in ECAs are highly complex. Currently the conduction mechanism is still under debate. Further work is necessary to determine what factors are most important in determining the macro-scale performance of ECCs. Furthermore, deriving fundamental conclusions regarding the conduction mechanism from noticing a change in an engineering result is difficult, especially when trying to compare composites prepared and processed in different ways, with different polymeric compositions, different particle shapes, with different surfactants and different methods of characterization.

1.9 Future perspective on ECCs for electronic packaging

Future advances in electronic packaging will be stratified into one of two key objectives, increased performance or increased functionality. Obtaining increased performance in ECCs mainly consists of increasing complexity of device architecture, reducing form factor, increasing conductivity, decreasing dielectric loss and increasing I/O while maintaining price parity.

The second area of growth for electronic packaging materials is related to increase functionality, form factor and human interfaces. Recent developments in electronic

devices have revolutionized how humans connect with their devices. Developments in electronic packaging have enabled the fabrication of low cost, large area touch enabled displays. The production of tablet-enabled devices like the iPad has enabled people to interact directly with their devices rather than through peripheral devices. New packaging technologies, which enable new methods of human interaction with their devices, will enable new functionality impossible with current packaging technologies.

Over the past decade significant effort has been devoted to create flexible electronic devices. To achieve flexible electronic devices required a complete redesign of how devices are fabricated. Active materials have been transitioned from silicon wafers to grown amorphous silicon or organic electro-active molecules and solder and epoxy based interconnect technologies have been abandoned and replaced with more compliant interconnect materials [145, 146]. Recently, companies have started developing flexible displays, photovoltaics and mobile devices however the cost and reliability of these devices currently prohibit their large-scale commercialization [146-148]. An even more challenging objective is to produce devices that are not only flexible but are stretchable. The leading researcher in the field of stretchable electronics is J. A. Rogers, his group has developed a wide range of stretchable electronic devices based small silicon active devices interconnected by ultra-thin serpentine-like interconnects supported on elastomeric substrates [149-156]. Using this stretchable technology Rogers et al has fabricated: curved linear charge coupled devices (CCD) which mimic the human eye, inverters, bio-absorbable electrodes, light emitting diodes (LEDs), organic photovoltaic devices, electro-optic devices, etc [149-156]. All of these devices gain additional function through their ability to bend and stretch with their environments. Despite their successful

fabrication of many complex devices using conventional micro-fabrication technology, fabrication of these stretchable devices involves many more processes than fabricating conventional rigid devices. These additional processing steps directly correlate to an increase in cost and a decrease in yield. Therefore application of Rogers' technology will likely be limited to specialty products and medical devices where cost is less of a concern. For stretchable electronic devices to go mainstream, new simple packaging technologies will need to be developed to achieve adequate device performance and stretchability. Chapter 3 presents a parallel approach to fabrication of stretchable electronic devices using highly conductive silicone based printable stretchable conductive composites. Finally, in Chapter 4, we for the first time show the operation of stretchable-high impact toughness, radio frequency devices capable of operating at a wide variety of temperatures.

1.10 Research methodology and objectives

This thesis provides new perspective and develops new technology for future electronic packages. In Chapter 2 of this thesis we will address the fundamental mechanism of the conduction mechanisms in ECC. In this chapter, we will show how tunneling / hopping rate, not direct metallic contact area is the conductivity limiting conduction mechanism. Chapter 3 presents a new approach for fabrication of stretchable electronic devices using highly conductive, printable silicone-based stretchable conductive composites. Finally, in Chapter 4, we for the first time show the operation of stretchable high-impact toughness, radio frequency devices capable of operating at a wide variety of temperatures.

Research Objectives:

- Understand the effect of the interface on the conduction mechanism in ECCs.
- Develop new highly conductive silicone-based stretchable conductive composites for use in stretchable electronic devices.
- Demonstrate fully functional stretchable-RF devices using stretchable silicone conductive composites.
- Provide framework and processing techniques to utilize silicone-based stretchable conductive composites for high-impact and stretchable applications, where stretchable and compliant conductors enable increased device functionality.

CHAPTER 2

UNDERSTANDING THE INTERFACE IN ELECTRICALLY CONDUCTIVE COMPOSITES

2.1 Introduction

Isotropic-ECCs are composed of small particles embedded in a polymer matrix. Because these particles are small they inherently have a high surface area. As surface area increases interfaces and interfacial properties become increasingly more important in determining the properties of the bulk material. ECCs need to be designed such that the interaction between the polymer matrix and the conductive fillers is sufficient to prevent aggregation; while at the same time you do not want the matrix to interact too strongly with the particles, because it would limit metallic contact. Controlling the polymer-particle interaction, surfactant, viscosity, cure kinetics, shrinkage during curing and particle filler loadings is essential in determining the particle-particle interface within the composite [81, 82, 157, 158]. Most published literature improperly describes the conduction mechanism at the filler-filler interface in ECC as a series resistor consisting of the constriction resistance and the tunneling resistance [157, 158]. This type of model assumes that direct metallic contact is non-existent; however, it is commonly assumed that metallic contact does exist [74, 81, 139, 157-164]. Based on the proposed model of electrical conductivity in ECCs (Eq. 2-8), incorporating constriction resistance in series with tunneling resistance would be including an area dependent effect twice. Furthermore, charge segregation on a single particle as implied by constriction resistance would create a local potential increasing tunneling/hopping probability. However, this

phenomenon is excluded from the model. We show in this chapter a new way to conceptualize the interface between conductive fillers and show experimentally that through film transport mechanisms is the conductivity determining mechanisms in ECCs.

2.2 Experimental methods

Two proof of concept type experiments were used to gain insight into the structure of the interface: 1. Theoretical description of the interface between metallic fillers. 2. Study of the effects of matrix dielectric constant on conduction in ECC.

2.2.1 Theoretical reconceptualization of the filler interface

Thermogravimetric analysis (TGA) was conducted using a Q5000 (TA Instruments). Ag flakes (Ferro Corporation) were heated to 150 °C at a rate of 10°C / min, the flakes were held isothermally for 1 hour and then heated to 300°C at a rate of 5°C/min. Differential scanning calorimetry (DSC) Q2000 (TA Instruments) was conducted isothermally at 150°C for 1 hour, followed by heating to 300°C at a rate of 5°C/min. The silver flake interactions were conceptualized by considering the forces that result due to deformations in the adsorbed monolayer upon close approach. The Hertz model and the Shull correction factor were used to qualitatively describe the surface forces between approaching Ag flakes.

2.2.2 Effect of matrix dielectric on electrical conductivity

Diglycidyl ether of bisphenol-F (DGEBF, Shell Chemical Company) (Epon 862) was doped with Cobalt (III) Acetylacetonate (CoAcAc) (98% Sigma Aldrich) at concentrations of 2.5 and 5 wt%. CoAcAc was dissolved in DGEBF at 80°C for >7

hours, until the CoAcAc was completely dissolved. Curing agent, hexahydro-4-methylphthalic anhydride (HMPA, Lindau Chemicals) and catalyst 1-cyanoethyl-2-ethyl-4-methylimidazole (2E4MZ-CN, Shikoku Chemicals Corporation) was added to the epoxy at room temperature. ECA was prepared by dispersing a bimodal mixture of silver flakes in the epoxy formulation in a 4(Ag):1(epoxy) ratio by weight. ECA Formulations prepared are outlined in Table 8. Two strips of Kapton tape (Dupont) were applied onto pre-cleaned glass slides. ECA formulations were printed onto glass slides using a doctor blade. Following thermal cure at 150°C for 1 hour, bulk resistance was measured as described in Appendix A. The dielectric constants of the prepared epoxies was determined using a dielectric analyzer (TA Instruments) model 2970, using a single surface remote sensor at room temperature immediately following curing at 150°C. The cure kinetics of the epoxy systems formulated was determined using a differential scanning calorimeter TA Instruments model Q2000 at a ramp rate of 5°C/min up to a maximum temperature of 250°C.

Table 8. ECA formulations tested.

Epoxy (wt%)	Co(III) ACAC (wt%)	Silver A	Silver B	Cure Temperature/Time
20	0	40	40	150°C / 1 Hr
17.5	2.5	40	40	150°C / 1 Hr
15	5	40	40	150°C / 1 Hr

2.3 Theoretical conceptualization of the filler-filler interface

DSC on silver flakes coated with stearic acid determined the desorption onset temperature to be 161.33°C and 185.38°C, for Ag 26LV (Figure 14) and Ag 52 (Figure 15) respectively. Since this is significantly greater than the ECA curing temperature of 150°C, the surface lubricants do not desorb during the curing process. Similarly,

Isothermal DSC at the curing temperature of 150°C confirmed that there is no desorption during the curing process (Figure 16). TGA did show some evidence of weight loss at 150°C; however this is likely to correspond to weakly adsorbed organics or water on the surface of the Ag flakes. Even if the weight loss at 150°C is correlated to desorption, the rate of desorption is slow to impact the resulting filler interface. The desorption of the surfactant is evident by the peak at 189.5°C in the TGA (Figure 17). The positive weight gain seen in the TGA is likely the result of oxidation following desorption. Since 2E4MZCN-based cure used in the epoxy system reacts quickly, gelation occurs prior to significant desorption of surfactants. Desorption following polymeric gelation will not affect the interconnectivity of the fillers. Thus we must assume that the surfactants remain on the surface of the silver flakes following the curing process.

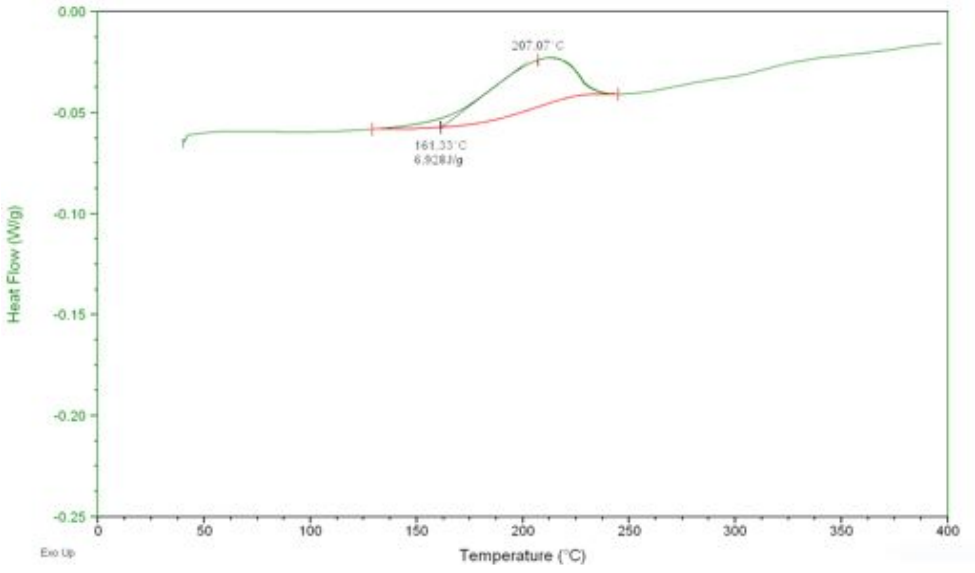

Figure 14. DSC of surfactant desorption from the surface of Ag 26 LV [11].

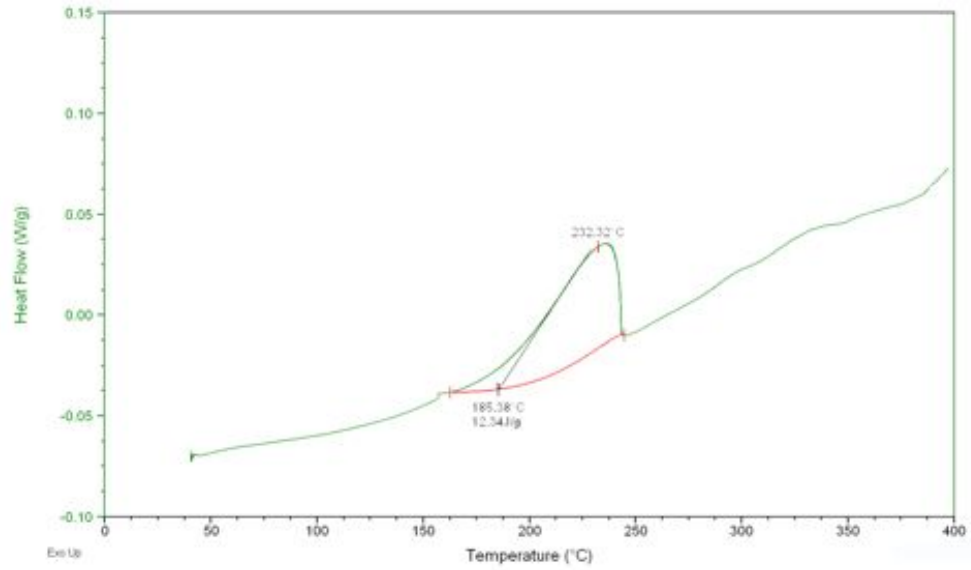

Figure 15. DSC of surfactant desorption from the surface of Ag 52 [11].

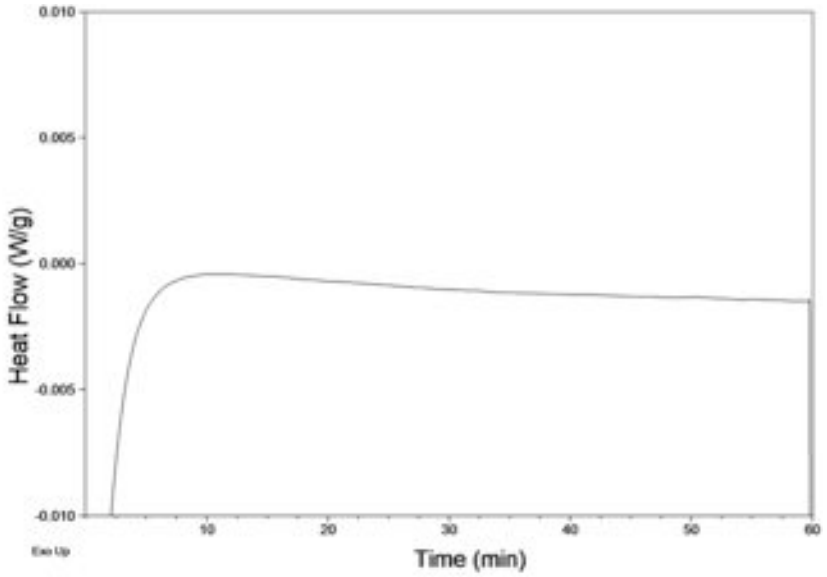

Figure 16. Isothermal DSC of silver flakes at 150°C [11].

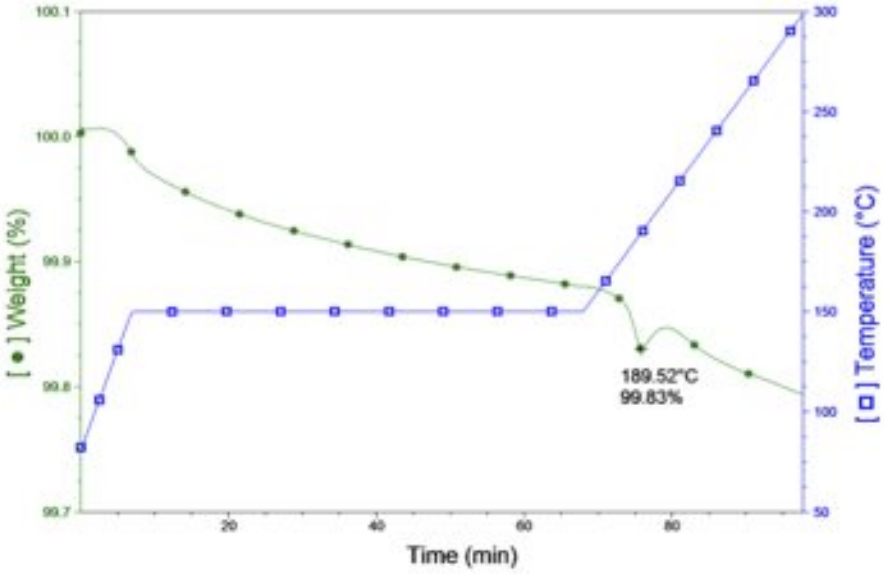

Figure 17. TGA showing desorption of surfactant from the surface of Ag flakes [11].

These adsorbed surfactants are essential to obtain uniform highly conductive ECA because they act as a lubricant, stabilizing the particle dispersion and preventing aggregation. Silver flake dispersions stabilized with stearic acid surfactants are stable for >3 months without any noticeable sedimentation or aggregation. Without surface treatment of silver flakes ECA formulations are unstable, inhomogeneous and difficult to process. Thus, because of the existence of a thin layer of adsorbed surfactant on the surface of the silver flakes, the interactions between two silver flakes can be visualized as shown in Figure 18.

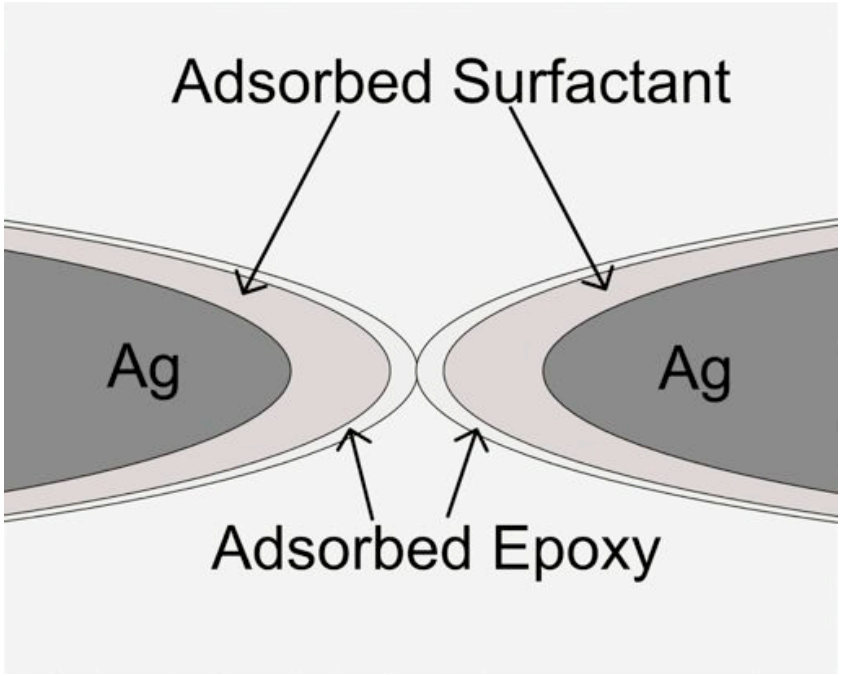

Figure 18. Schematic diagram of interface between two silver flakes on close approach [11].

The silver flakes will be coated with a surfactant ~2.3 nm thick and a layer of physically adsorbed epoxy. The thickness of the physically adsorbed epoxy layer is dependent on its molecular length, conformation, molecular structure and surface interactions. Upon close approach of particles during printing, the surfactant and surface adsorbed epoxy must be displaced to form metallurgical contact. Under the assumption that the silver particles are not deformed during the printing process, the deformation of the surfactant layer can be modeled by the Hertz theory (Figure 19) [165, 166]. The Hertz theory relates the contact area with the force through the bulk modulus of elasticity of a penetrating sphere of radius R onto a planar surface. For simplicity we will assume that the adsorbed layer is a homogenous elastomeric monolayer with thickness h. Therefore,

silver flake on close approach will cause an indentation (δ) in the monolayer, as described by eq. 11.

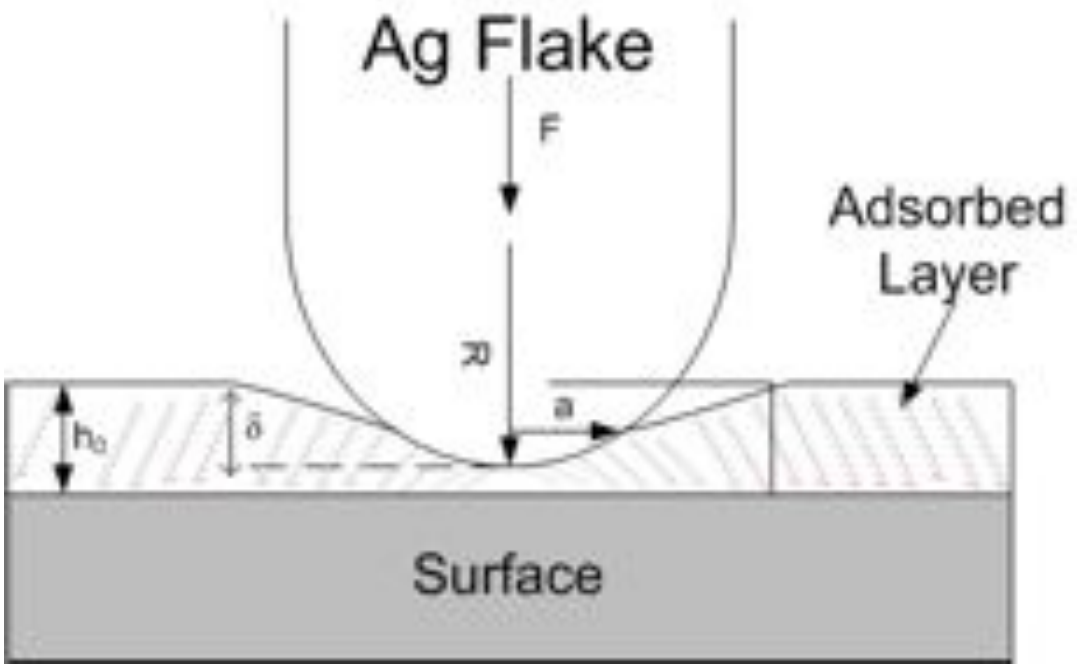

Figure 19. Diagram of particle interaction with chemically adsorbed stearic acid [11].

$$\delta = \frac{a^2}{R} \tag{11}$$

The indentation of the surfactant molecules can be related to the applied force through the bulk modulus (K_{bulk}):

$$K_{bulk} = \frac{3E}{\left(2(1-\nu)^2\right)} \tag{12}$$

$$F = K_{bulk} R^{1/2} \delta^{3/2} \tag{13}$$

The applied force causes a distribution in the normal stress (p(r)) of the adsorbed layer along the radius of the penetrating particle:

$$p(r) = \frac{3K_{bulk}a}{2\pi R}\left(1-\left(\frac{r}{a}\right)^2\right)^{1/2} \tag{14}$$

The yield stress of the adsorbed layer, perpendicular to the loading axis is defined from the point where the sphere starts penetrating into the adsorbed layer:

$$\sigma_{y\perp} = \frac{3F_y}{2\pi a_y^2} \tag{15}$$

Upon indentation, the adsorbed layer will act to distribute the stress. This effect is incorporated through the Shull correction factor for indentation [167].

$$\delta = \delta_H \left(0.4 + 0.6 \exp\left(-\frac{1.8a}{h_0} \right) \right) \tag{16}$$

$$F = F_H \left(1 + 0.15 \left(\frac{a}{h_0} \right)^3 \right) \tag{17}$$

ECA formulations are significantly more complex than the simplified model above, however the aforementioned model provides a perspective and insight into the interfacial forces between silver flakes. Both the Hertz model and the Shull correction factors assume a non-interacting, low viscosity, frictionless medium. Experimental determination of the repulsive force of adsorbed surfactants in aqueous solutions, using atomic force microscopy has shown the repulsion force to vary between 1-15 nN (~2.5-37.5 MPa) [168]. The variation in repulsion force is a direct result of the molecular length of the adsorbed layer and dispersion stability. The models represented only accounts for the interaction when one of the surfaces is treated; interactions with two surfactant-modified surfaces are exceedingly more complex. Furthermore, secondary relaxation mechanisms of the epoxy, which acts as the solvent, coupled with the large frictional forces at the interface, add an additional degree of complexity. Since all these effects serve to increase the particle-particle repulsion, this model can be used to define the minimum possible force needed to cause direct metallic contact. A more complex and descriptive model is needed to quantitatively understand the surface forces in ECA.

However, since the required force to cause deformation in the adsorbed surfactant is well in excess of the applied force, formation of a percolated metallic network is highly unlikely. This implies that a thin dielectric layer exists between the silver flakes. Thus secondary charge transport mechanisms dominate charge transport at the interface. These secondary conduction mechanisms consist of tunneling and hopping electron transport mechanisms. It is likely that the statistical probability of these tunneling/hoping mechanisms control the macro scale conductivity of ECAs.

2.4 Effect of matrix dielectric constant on electrical conductivity in ECCs

Previous studies have found that inclusion of CoAcAc, a latent catalyst can increase the dielectric constant of epoxy from 3-4 to 5-6 [169]. Since tunneling rates are inversely related to the dielectric constant, modulation of the dielectric constant can serve as an indicator of the relative importance of tunneling in the macroscale-conduction in ECAs [170]. We prepared epoxy based ECAs as described in the experimental methods. It was found that the dielectric constant of the virgin epoxy, 2.5 wt% CoAcAc and 5 wt% CoAcAc epoxy was ~3.1, ~4.2 and ~5.5 respectively. This increase in dielectric constant upon doping with CoAcAc is due to highly polarizable bonds in the CoAcAc structure.

To minimize experimental variability associated with incorporation of a latent catalyst, 2E4MZCN, a catalyst which reacts quickly at low temperatures was used to catalyze the curing of the doped epoxy. DSC confirmed that the cure mechanism was unaltered by the addition of the CoAcAc, in the presence of 2E4MZCN. Comparison of the curing profile for virgin (Figure 20) and CoAcAc doped epoxies (Figure 21), where the cure was catalyzed by 2E4MZCN, shows that the enthalpy of reaction and onset temperature was unchanged by the addition of 5 wt% CoAcAc. DSC of CoAcAc

catalyzed epoxy was found to have an onset temperature 160.43 °C, ~45°C higher than both the doped and virgin epoxies (Figure 22). Thus, the CoAcAc doping played an insignificant role in the cure mechanism.

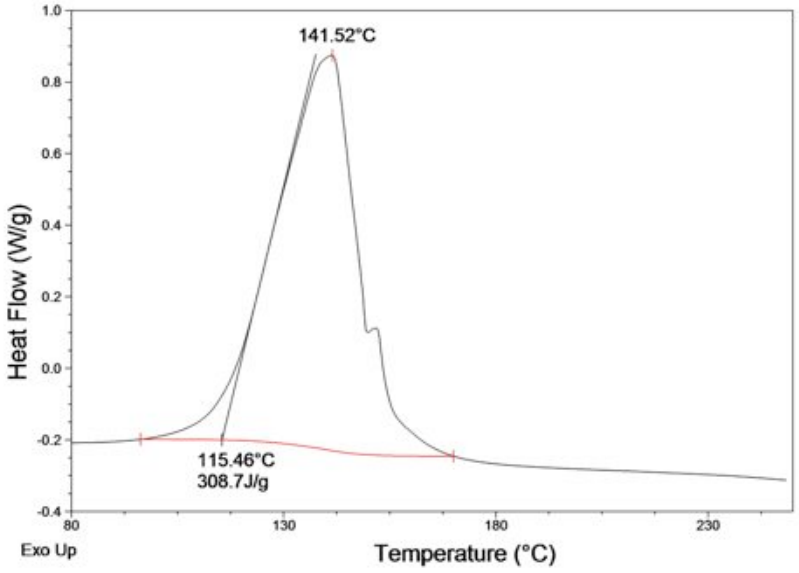

Figure 20. DSC showing curing peak of virgin 862 cured with 2E4MZCN catalyst [11].

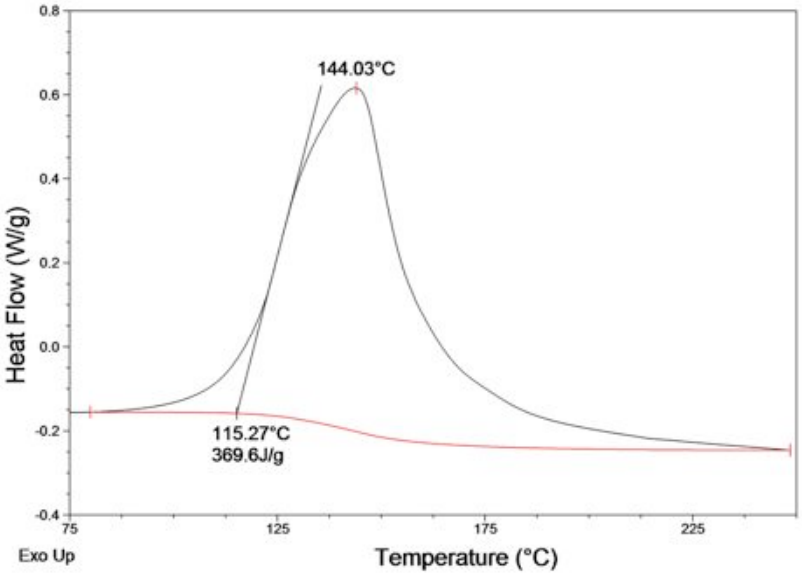

Figure 21. DSC showing curing peak of CoAcAC doped 862 epoxy cured with 2E4MZCN catalyst [11].

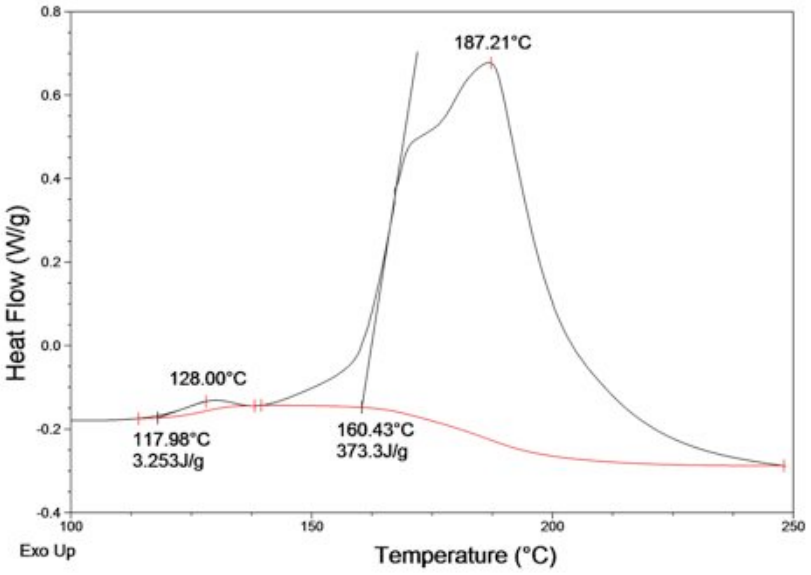

Figure 22. DSC showing curing peak of 862 epoxy catalyzed by CoAcAc [11].

The conductivity measurements on epoxies formulated as described in Table 8 are shown in Figure 23. ECA prepared with the virgin epoxy was found to have an average resistivity of $9.71 \times 10^{-4} \pm 3.37 \times 10^{-4}$ Ω-cm. The CoAcAc doped ECA was found to have a resistivity directly correlated with the doping concentration / dielectric constant. The resistivity of the ECA doped with 2.5 wt% and 5 wt% CoAcAc had average resistivities of $2.24 \times 10^{-3} \pm 7.09 \times 10^{-4}$ Ω-cm and 1.56±0.52 Ω-cm respectively. If the silver flakes are in direct metallic contact, the dielectric constant of the epoxy should have no effect on the DC resistivity. However, tunneling probability is inversely correlated to the polarizability of the tunneling medium [171]. Thus, tunneling must play a significant role in the conduction pathway. If a percolated network of metallurgical interconnected particles exists alterations to the tunneling probability would have a minimal effect on the bulk resistivity. Any doubt that one might have regarding the validity of this conclusion should also consider that the volume percentage of silver flakes increased with CoAcAc concentration. The virgin ECA contained 30 vol% Ag flakes, where the ECA doped with

5 wt% CoAcAc had a 31.5 vol% of Ag. This increase in filler loading should dramatically enhance the electrical conductivity of the ECA, but the reverse was observed. The orders of magnitude dependence of the bulk resistivity on tunneling probability confirms that a percolated metallic network does not exist.

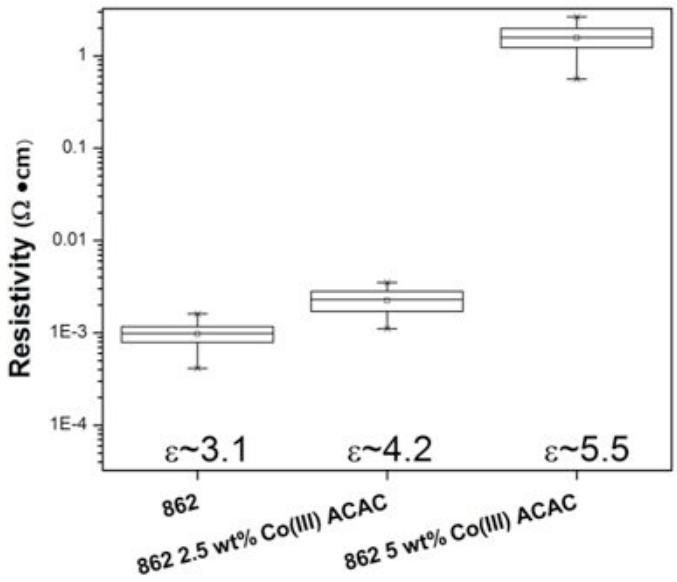

Figure 23. ECA resistivity as a function of CoAcAc concentration (dielectric constant) [11].

2.5 Outlook and perspective

The evidence confirming that an interconnected metallic network does not exist in ECAs is not unexpected. Over the past 15 years, literature has qualitatively described the resulting ECA structure as Ag flakes isolated by small insulating layers. However, they failed to deduce that this interpretation implies that a percolated metallic network does not exist.

Typically in published literature, tunneling and hopping mechanisms has been considered a secondary conduction mechanism that only contributes marginally to the

bulk electrical properties. This study emphasizes the importance of the nanometer to sub-nanometer region separating the conductive fillers. Even though it has already been well established, through studies on surfactants and sintering, that enhancing contact between conductive fillers can greatly enhance conductivity of ICAs, we present the first study which shows that tunneling/hopping is the conductivity determining mechanism in ECAs, above their percolation threshold. This new insight provides researchers a new direction to approach increasing conductivity of ICAs, with enhanced potential for significant impact.

CHAPTER 3

STRETCHABLE ELECTRICALLY CONDUCTIVE COMPOSITES

3.1 Motivation

Future stretchable electronic devices require natural integration at the system, device and package level in the form of a functional package. The flexible and stretchable package has to enable natural integration with its environment and its movements. New flexible and stretchable fabrication processes and interconnection technologies must be developed, focusing on simplicity of design and functionality. The advantages of stretchable electronics has been highlighted by Rogers et al, who has fabricated curved linear charge coupled devices (CCD) which mimic the human eye, inverters, bio-adsorbable electrodes, light emitting diodes (LEDs), organic photovoltaic devices, electro-optic devices, etc. [149-156]. Each of these devices gain increased functionality by their ability to change their shape under mechanical load. For example due to the shape and stretchability of the curvilinear CCD array, single lens optics can be used without having to worry about third-order Seidel aberrations. Designing optics on a stretchable-curvilinear platform dramatically increases resolution while reducing cost and form factor associated with complex lenses and optics [149]. The ability to design stretchable electronic devices enables the fabrication of devices which integrate naturally with the human body and / or its surroundings. In the case of the curvilinear CCD array, the ability to stretch enables the device to be packaged and function nearly identically to the human eye [149]. Despite the successful fabrication of many complex stretchable electronic devices the electronic packaging technology is still not ready for the

fabrication of commercial stretchable electronic devices. The following section will discuss the current state of the art in packaging for stretchable electronics.

3.2 Methods of packaging stretchable electronics

Packaging of stretchable electronics requires that the components be interconnected and bonded to elastomeric substrates, typically PDMS. To achieve stretchability in mechanically unconventional electronics one of two approaches is used, either adding complex geometry to accommodate strains or by creating new materials which are not only stretchable but also electro-active [152, 172].

3.2.1 Stretchable geometries

Achieving stretchability actually does not require stretchable materials, just flexible materials in stretchable geometries. For example, consider a metallic spring, even though the metal itself barely stretches under an applied load, the entire structure can stretch or compress significantly. The same approach is used when creating stretchable electronics, metallic interconnect structures are shaped in complex geometries. However, typically conventional inorganic semiconductors used in electronics are extremely brittle. This obstacle is easily overcome by making brittle materials ultra-thin, essentially eliminating any strain associated with bending. For example, silicon sheets 100 nm thick supported on a 20 μm elastomer experience only a ~0.1% peak strain when bending to a radius of curvature of 1 cm. This strain is significantly less than the fracture limit of silicon, ~1% [150, 173]. Furthermore, the true strain on the material can be reduced by minimizing the contact between the ultra-thin geometrically stretchable material and the elastomeric substrate. By designing the electronic package such that brittle materials are

made flexible and in out of plane, wave-like geometries electronics can stretch significantly with minimal stress and strain on the brittle components. Significant effort has been devoted to control the buckling processes to obtain specific geometries. Typical geometries used to obtain highly stretchable electronics include 1D and 2D "wave" like buckling, spiral, leaf-spring type and serpentine patterns [174-178]. Using this approach it is easy to fabricate devices that can withstand in-plane strains of >100% [179].

The key advantages of this technology are that no new materials or technologies not currently in use in micro-fabrication processes need to be developed or utilized. Due to the familiarity of the processes necessary to fabricate stretchable electronic devices based on fabrication of ultra-thin flexible geometries, 1st generation stretchable electronic devices will likely be fabricated using this approach. However, there are many limitations of the techniques and processes that will dramatically hinder the application of these technologies in mass-produced, low-cost consumer electronics. First, fabricating the structures and geometries necessary to produce functional electronic devices is highly complex involving a significant number of processing steps. For example, to fabricate the electronics necessary to produce the stretchable CCD array requires 80 individual processing steps and 8 individual lithography processes [149]. Since the cost of fabrication increases multiplicatively to exponentially with the addition of each processing step, large-scale production of these devices is cost prohibitive. Furthermore, once the device is fabricated it needs to be mechanically transferred to a pre-strained substrate. The transfer process is difficult, yet can be accomplished with high yields, >95% for large 20mm by 20 mm arrays containing 163,216 elements [149]. However, even at these yields, a single failure would result in the failure of an entire line. Because

these stretchable devices are fabricated in large arrays, single elements, which malfunction, cannot be replaced. To obtain highly reproducible device fabrication requires highly uniform wafer level processing. However, obtaining a high degree of uniformity during wafer level processing is challenging, especially for electro-optic elements like LED and photovoltaics. For example, in conventional LED fabrication variation in performance on the wafer level is significant enough that each element has to be pre-tested and sorted by quality [180]. Another issue with this approach is it is difficult to obtain high area densities of active components in the wafer level or on the package. This is an unavoidable consequence of having complex geometries, which can linearize when strained. Again using the curvilinear CCD camera as an example, the pitch between the electronic elements 20 μm and the size of the active elements is only 17.5 μm; giving an aerial coverage of only 28%. Areal coverage is especially important for the design of stretchable displays, CCD and photovoltaics because it directly influences the device performance. Taking a new approach, where trenches which contained the buckled interconnects were fabricated on the PDMS substrate, areal densities of GaAs photovoltaics >70% were obtained [152]. However, designing electronics with this geometry would limit its flexibility if the conductive elements are located on the interior radius. Furthermore, because geometry not the material is responsible for the stretchability, the geometry needs to be optimized for the specific application. The need for the geometry and processes to be redesigned with for each application is a significant economical limitation.

Another geometry-based method to prepare stretchable electronics was originally derived from observations that gold deposited on pre-strained PDMS spontaneously

buckles when being released from the applied strain [181]. Because Au deposited on pre-strained PDMS has out of plane geometry these structures are stretchable. It was found that these structures could be strained up to ~22%, significantly longer than the un-textured Au films [182]. The mechanism was determined to result from the formation of small micro-cracks on the Au film, which allows the film to deform out-of-plane during stretching. This out of plane deformation enables large strains in the macro-scale dimensions without invoking large strain in the Au [183]. Recently, these techniques have been used to fabricate multilayer electronic devices, something currently impossible using Rogers et al. approach [184]. However, preparation of stretchable electronics using this technique has many limitations. First, Au adhesion to PDMS is very weak. As a result deposited Au layers has very poor abrasion resistance and is easily transferred to any surface it touches. Secondly, because the stretchability of these structures is predominantly based upon the formation of micro-cracks any strain will result in decreased resistivity. More concerning is as these devices are repeatedly strained these cracks will propagate, eventually leading to failure. Due to the lack of consistent performance and reliability it is unlikely that deposited films could be used in stretchable electronic devices.

3.2.2 Stretchable electro-Active materials

A second approach to produce stretchable electronic devices is to use materials that are intrinsically stretchable. This approach is challenging because highly conductive materials tend to have low elasticity and poor mechanical robustness. On the other hand, materials with good elasticity and toughness tend to have poor electrical properties. Therefore, obtaining stretchable electro-active materials requires the development of

composites to achieve high conductivity and good mechanical properties. However, achieving conductivity close to that of bulk metal is extremely challenging. For example, the lowest reported resistivity for conductive rubbers containing carbon particles or Ag is 10 and 1.75×10^{-4} Ω-cm respectively [172, 185]. Surprisingly, research on stretchable conductive composites has been relatively limited. Most of these elastic conductors have focused on carbon nanotube filled composites. However, due to the mechanical reinforcing properties of carbon nanotubes researchers are constantly searching for methods to obtain high filler loading without limiting elastic strain. Shin et al. showed the through infiltration of multi-walled carbon nanotube forests with polyurethane that a conductor with rubber-like elasticity could be produced [186]. However, the composite had a relatively high resistivity 0.5 Ω cm, showed significant increase in resistance during tensile strain and showed reduced electrical conductivity after 100 cycles to elongations of 60% or more [186]. Work by Sekitami et al. showed that using an ionic liquid, single-walled nanotubes (SWCNT) could be dispersed in vinylidiene floride-hexafloropropylene copolymer. This composite had a resistivity of 1.75×10^{-2} Ω-cm and showed minimal degradation after repeated tensile strains of 38% [187]. In a later publication the same group showed that jet milling could be used to enhance the performance of the elastic conductor [188]. They reported a conductivity of 9.8×10^{-3} Ω-cm and a stretchability of 29% [188]. Or by reducing the concentration of carbon nanotubes they were able to achieve tensile strains of 118% but had a high resistivity of 0.102 Ω-cm [188]. To date, the best performing elastic conductor reported was published by Chun et al., in Nature Nanotechnology [186]. They showed that hybrid composites of SWCNT decorated in Ag nanoparticles and micron sized Ag flakes, in

polyvinylidenefluoride (PVDF), had a resistivity of $1.75x10^{-4}$ Ω-cm after hot rolling [186]. Prior to hot rolling the composites had a measured resistivity of $3.2x10^{-4}$ Ω-cm [186]. The samples were found to be conductive at tensile strains of 140%, however the resistivity dramatically increased after strains of 30% or more (ρ >1x10-3 Ω-cm) [186]. Moreover, the composite showed good performance under cyclical strains >5000 cycles to 20% elongation, but its reliability at strains greater than 20% elongation was not reported [186]. There are many advantages to using this approach to fabricate stretchable electronic devices. First, electronics based on stretchable composites can be prepared via direct printing processes, dramatically reducing the cost of device fabrication. Furthermore, because they are polymer based it is very easy to tune the mechanical properties, electronic response and adhesion for specific applications. Furthermore, if sufficient adhesion can be achieved, these materials could be used as a compliant interconnect material which could accommodate the large stresses associated with CTE mismatch in large area interconnects. Geometrically stretchable structures hold no potential for use as interconnect materials. However, to be competitive with geometrically stretchable electronic packages the conductivity and performance of stretchable conductors needs to be improved. The following sections of this chapter will discuss my approach to produce highly conductive stretchable composites for future stretchable electronic devices.

3.3 1st generation stretchable electrically conductive polydimethylsiloxane

Surprisingly, there are very few publications directly discussing the fabrication of printable stretchable conductive silicone composites for electronic packaging

applications. In these first set of experiments the feasibility of creating highly conductive stretchable conductive silicone composites and a process necessary to package stretchable electronic devices was shown.

3.3.1 Experimental methods

The experiments conducted could be divided into three key subcategories: 1. Fabrication and characterization of polydimethylsiloxane (PDMS)-based stretchable electrically conductive composites (S-ECC) 2. Characterization of the tensile-electrical response of S-ECC. 3. Printing and device level integration.

Fabrication and characterization of highly conductive PDMS stretchable electrically conductive composites

S-ECC was fabricated using polydimethylsiloxane Slygard 186 (Dow Chemical) with a bimodal distribution of silver flakes SF-52 and Ag 26LV (Ferro Corporation). Silver flakes were added to the two-part PDMS mixture in an 80:20 by weight ratio. Silver flakes were dispersed in PDMS using a mixture of manual stirring and ultra-sonication. Two strips of Kapton tape (Dupont), 3-mil thick was applied onto pre-cleaned glass slides. S-ECC was printed between the pieces of tape using a doctor blade. Following thermal cure at temperatures in the range of 120-180°C for 15 minutes, the bulk resistance was measured as described in Appendix A. Characterization of the shrinkage during cure was measured isothermally at 150 °C using a thermal mechanical analyzer Model Q400 (TA Instruments).

Characterization of the tensile-electrical response of S-ECC

Eight pieces of 2-mil Kapton tape (Dupont) was placed within a metallic pan. A two-part mixture of PDMS Sylgard 184 (Dow Chemical) was poured into the metallic pan ~0.75 cm thick. The PDMS was degassed using sonication until no air bubbles were visually apparent. PDMS was cured at 70 °C for 1 hour. Following cure PDMS molds were removed from the metallic pans. Tensile specimens were cut using a razor blade from the PDMS mold using a custom designed dog-bone shaped tensile template. UV-ozone treatment (UVO) (Samco International) for 7 minutes was used to clean the surface and alter the surface properties of the PDMS.

Contact angle measurements were measured using Model 190 CA Goniometer (Ramé-Hart Instrument Co.). Immediately following UVO treatment S-ECC prepared as described was screen printed into the inlayed impression of the tape. Copper foil (Sigma Aldrich) was placed on the ECA at the far ends of the tensile mold. The tensile mold was cured at 150 °C for 15 minutes. Following cure, simultaneous tensile and electrical measurements were recorded. Specimen dimensions were measured with a digital caliper (VWR). The tensile testing was conducted with an Instron 5548 microtester (Instron Corp.) at an extension rate of 2 mm/min. Electrical resistance was recorded simultaneously at 2-second intervals using a Keithley 2000 (Keithley Instruments Inc.) multimeter connected through testpoints software. Compressive DMA model 2980 (TA instruments) of mold following initial cure was conducted isothermally at 150 °C for 15 minutes.

Patterning and device level integration

Negative Photoresist NR9-8000 (Futurrex) was spin coated on 4-inch silicon wafer (University Wafer) using a Karl Suss RC8 spin coater (Karl Suss) at 750 rpm. Soft bake was conducted at 70 °C for 3 minutes followed by 150 °C for 2 minutes. Lithography was completed using a custom designed transparency mask on a Karl Suss MA-6 Mask Aligner (Karl Suss) exposure time 180 seconds. Post bake was conducted at 70 °C for 2 minutes. The pattern was developed using RD6 developer (Futurrex) for 5 minutes. The developed wafer was imaged using an optical microscope (Leica Microsystems). Degassed PDMS was poured over the pattern mold and cured at 70 °C for 1 hour. The PDMS mold was removed from the silicon wafer revealing the patterned PDMS substrate. Following UVO treatment (Samco International) for 7 minutes S-ECC was printed into the pattered PDMS substrate.

3.3.2 Results and discussion

Fabrication and characterization of highly conductive PDMS stretchable electrically conductive composites

Since the PDMS matrix used is a RTV-2 platinum cured silicone the composite will cure at room temperature. However, S-ECC cured at room temperature was insulating. Upon curing the S-ECC at high temperatures >150°C the composite undergoes a transition from insulating to conductive. This transition is caused by curing the elastomer in the expanded state. Following curing, when the composite cools, the polymer chains collapse, producing a compressive stress, which enhances particle

interconnectivity. Isothermal TMA at 150 °C for 15 minutes and sub-sequential cooling resulted in a linear dimensional change of 20% (Figure 24).

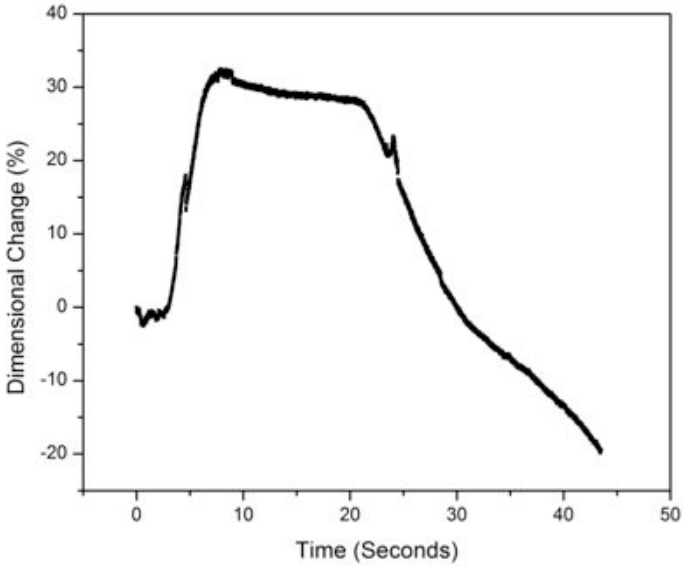

Figure 24. Isothermal TMA of S-ECC during curing at 150°C [189].

Curing the S-ECC showed that the resistivity of the composite decreased when increasing the curing temperature up to 150°C. Curing at temperatures higher than 150°C resulted in negligible change in the bulk resistivity of the composite. The minimum achievable resistivity for the S-ECC was ~$7x10^{-4}$ Ω-cm, only slightly worse than conventional epoxy based ECAs [7].

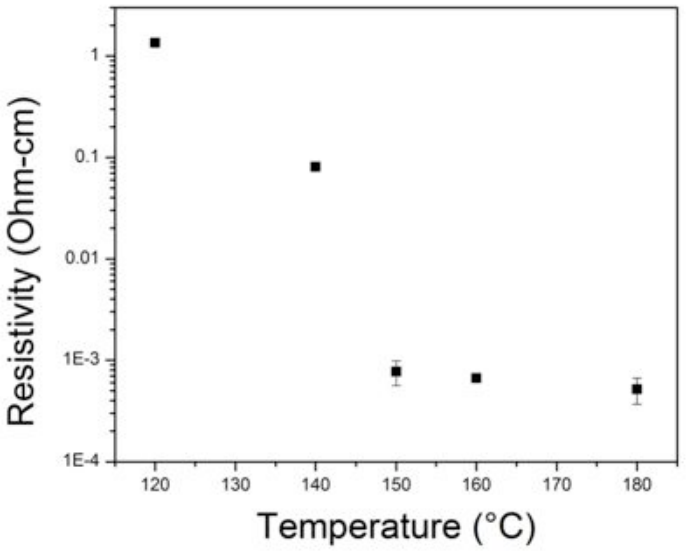

Figure 25. Bulk resistivity of S-ECC as a function of curing temperature [189].

Characterization of the tensile-electrical response of S-ECC

Commercially available ECAs have shown the capability to function under flexural and compressive strains. However, when applied to stretchable surfaces they fail under tensile strain >5%. Use of highly elastic matrix materials with high Poisson's ratio enables electrical contact between fillers to be maintained during tensile strain. PDMS which can be formulated to have nearly ideal Poisson's ratio (υ~0.5) is an ideal matrix material for use as a matrix for S-ECCs [190]. Preparation of a PDMS substrate material that could withstand the high temperatures of S-ECC curing without loss of mechanical properties required modification of the conventional Sylgard 184 formulation. Standard Sylgard 184 PDMS exhibited undesirable changes in its mechanical properties during the S-ECC curing. By reducing the crosslinking of the PDMS by incorporating 40:1 base to curing agent instead of the conventional 10:1, the elastic modulus decreased and elongation to failure improved. Compressive DMA showed that the storage modulus of

convention Slygard 184 PDMS changed from 90 MPa to 300 MPa during the S-ECC curing process. Tensile testing of PDMS-in-PDMS molds made with the conventional Slygard formulation failed at tensile strains of 5-10%. DMA confirmed that the modified PDMS formulation used had a much lower storage modulus of 0.2-0.8 MPa and exhibited minimal change during the S-ECC curing process (Figure 26). Furthermore, the mold was able to withstand tensile strains (>80%) without failure.

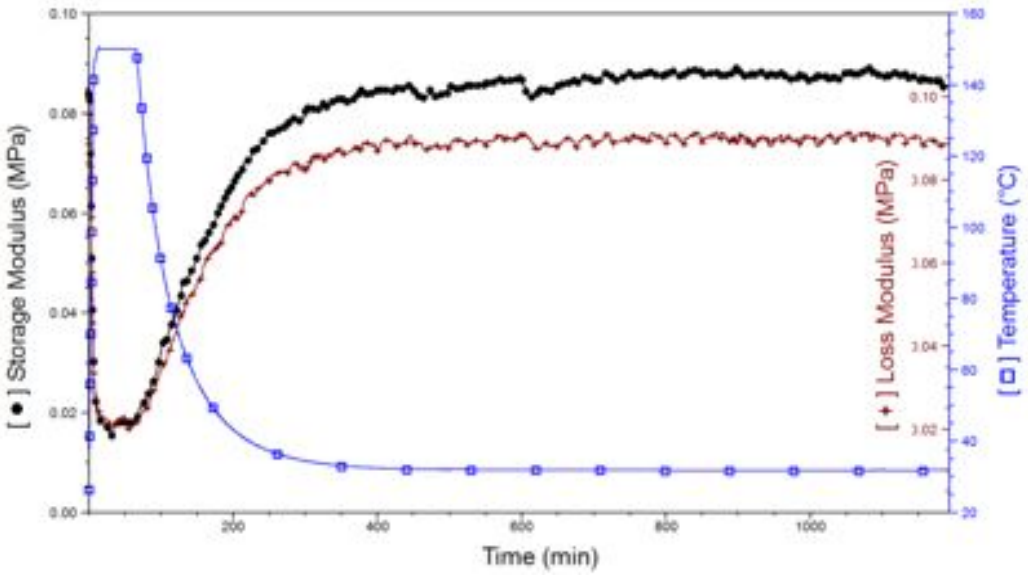

Figure 26. DMA of conventional Sylgard 184 PDMS following annealing at 150°C for 1 hour [189].

Due to the low surface energy of the PDMS substrate (~27 mJ/m^2) printing S-ECC is difficult. To facilitate printing, the surface of the PDMS mold was UVO treated. UVO treatment of the PDMS creates a temporary transformation of the surface from hydrophobic to hydrophilic. This transformation is believed to be the result of a "silica" like layer that forms as PDMS is oxidizes on the surface [191]. This silica like layer will undergo hydrophobic recovery over the course of a couple of hours, allowing the PDMS based S-ECC to adhere well to the surface of the PDMS mold [192]. The effect of UVO

treatment was characterized by measuring the contact angle with water. It was found that the UVO treated PDMS had a contact angle of 85.7°, compared to the contact angle of the untreated PDMS 116.1°. Images of the contact angle formed of water on the UVO treated and untreated substrate is shown in Figure 27.

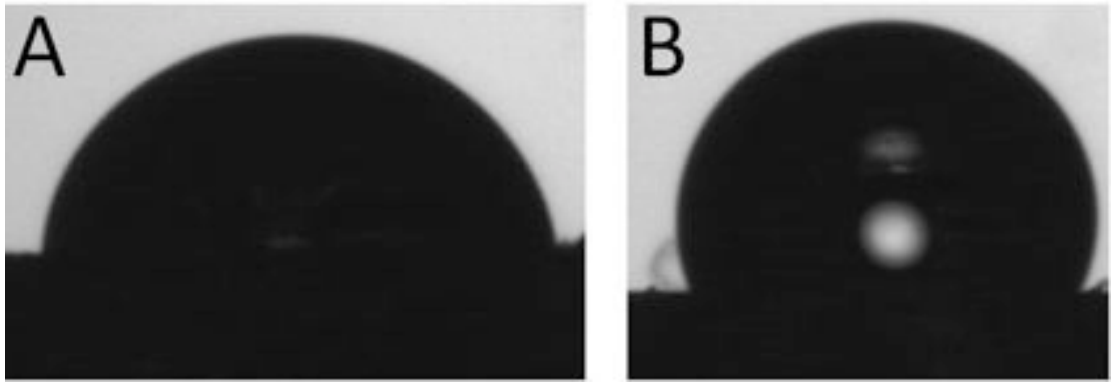

Figure 27. Contact angle measurements of A. UVO treated PDMS and B. Untreated PDMS [189].

Tensile specimens were prepared as described. Images of the tensile specimen molds are shown after initial cure (Figure 28A), following S-ECC cure (Figure 28B) and during tensile-conductivity experiment (Figure 28C-D). A plot of electrical conductivity as a function of percent elongation is shown in Figure 29. It is evident that there was no significant change in resistivity at elongations up to 40%. There was no noticeable change in resistivity for repeated tensile strains to 40%. The entire package also showed good performance under compressive and flexural strains. However, cyclical controlled simultaneous electrical measurements tended to lead to failure at the contact points. Furthermore, because of difficulties associated with making good electrical contact to the sample during tensile measurements, the reported resistance during tensile strain is an overestimate.

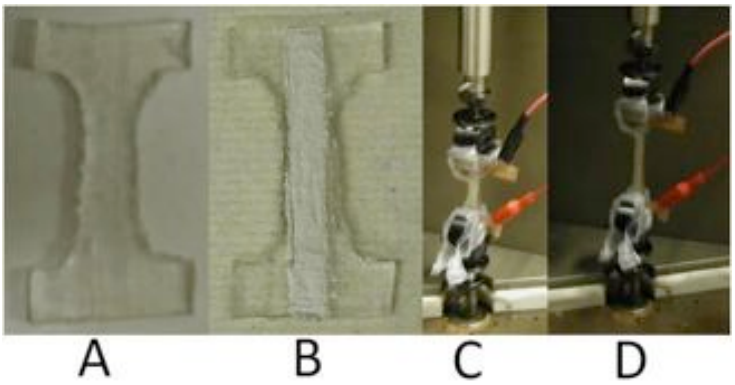

Figure 28. Images of A. tensile mold, B. tensile mold embedded with S-ECC, C. un-strained tensile specimen D. strained tensile specimen [189].

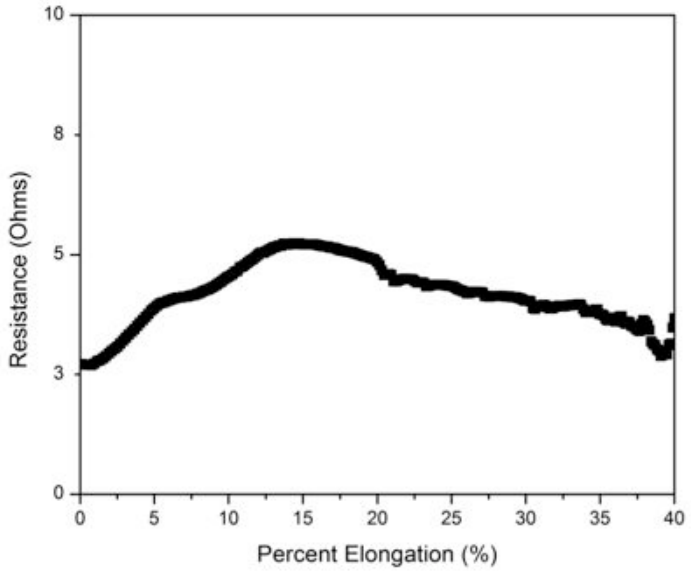

Figure 29. Graph showing measured resistance during tensile strain [189].

Patterning and device level integration

Functional electronics require the ability to fabricate complex structures with fine feature size (<100 μm) simply. PDMS represents the ideal material for use as a flexible, stretchable substrate. PDMS has been the leading material candidate for microfluidics and soft lithography processes because of its ability to be defined into complex structures with sub-micron scale resolution [190]. PDMS, because of its very low glass transition

temperature in the uncross-linked state, is a viscous liquid prior to curing, allowing high resolution inverse structures to be prepared from a master mold via a pour and cure process. Fabrication of S-ECC devices will consist of initial mold fabrication via conventional lithography processes. Master mold structures can be fabricated from SiO_2, Si_3N_4, metals, photoresist or wax [190]. Master mold can be used to produce >50 molds, dramatically reducing the cost of fabrication [190]. Following fabrication of a master mold, inverse structures of PDMS can be formed by pouring PDMS on top of the master molds surface and allowing the PDMS to cure. We defined our master molds using photoresist as described in the experimental methods. Upon fabrication of the PDMS mold and UVO treatment, S-ECC can be screen printed into the pre-defined structures. Subsequent surface mounting of micron sized discrete electrical components and curing will enable the formation of super-low cost flexible, stretchable electronics. The procedure to fabricate these devices is described schematically in Figure 31. An image of the lithographic features and the resulting features in PDMS substrate can be seen in Figure 30.

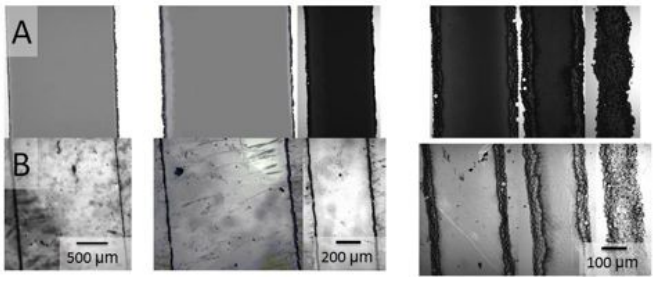

Figure 30. Images of lines fabricated in A. photoresist B. PDMS [189].

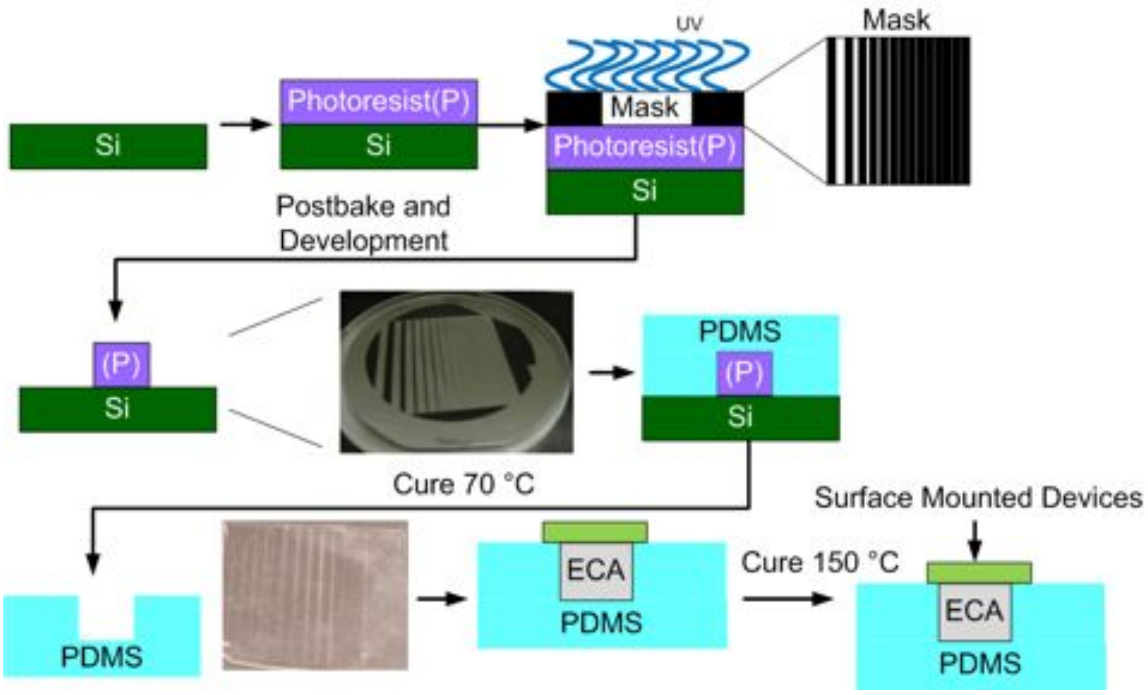

Figure 31. Schematic drawing showing fabrication process of S-ECC based electronics [189].

Outlook and perspective

We showed a proof-of-concept type experiment to show that highly conductive S-ECC could be formulated to have good performance during repeated tensile elongations. Furthermore, we showed a packaging process that could be used to integrate small discrete components on a flexible, stretchable package. However, there are many limitations of these initial materials and designs. First, the S-ECC has relatively low bulk conductivity. This low conductivity is likely the result of silica fillers used as toughening agents in the PDMS matrix. Furthermore, the processes and material designed can only be prepared in two-dimensional patterns limiting device integration and interconnectivity. Another issue for fabrication of functional electronic devices using this methodology is that the S-ECC does not have adhesive properties or strain isolation capabilities necessary

to mount and interconnect small-ridged electronic devices. Finally, the S-ECC produced with high Ag filler loadings was a high viscosity paste. The high viscosity of the paste, coupled with the low surface energy of the mold makes it very difficult to print fine features with high resolution. These problems will need to be addressed if this technology is to be implemented in consumer electronic devices.

3.4 Second Generation Stretchable Electrically Conductive PDMS

One of the key challenges of the 1st generation S-ECC was that the resistivity of the composite was too high for most commercial applications like CCD arrays, photovoltaic, RF devices etc. These problems will need to be addressed if this technology is to be implemented in consumer electronic devices. The following section will discuss the use of a novel additive, referred to as AA, which causes *in-situ* nanoparticle formation and growth, reducing contact resistance between Ag flakes within the composite. The sintering of Ag flake, using these *in-situ* formed nanoparticles causes the resistivity of the composite to decrease. Disclosure of the chemical name and structure of this additive will be included in a future publication.

3.4.1 Experimental methods

Effect of AA on electrical properties of S-ECC

Stretchable conductive composites (S-ECC) were fabricated using a silicone polymer matrix containing a bimodal distribution of silver flakes ranging in size from 1 μm to 20 μm (Ferro Corporation). The mixture consisted of 80:18:2 (wt%/wt%/wt%) of silver flakes, silicone Sylgard 186 (10:4) (Dow Corning) and AA respectively. The Ag

flakes were dispersed in the silicone matrix using a combination of manual stirring and ultra-sonication. Two strips of Kapton tape (Dupont) were applied onto pre-cleaned glass slides. S-ECC was stencil printed, in-between the pieces of Kapton tape, onto the glass slides. Following thermal cure at 170°C for 30 minutes, the bulk resistivity was measured as described in appendix A. The morphological changes from treatment of Ag flakes with AA at 150°C for 10 min and 30 min was imaged using LEO 1530 Scanning Electron Microscope (SEM) (Carl Zeiss). Similarly, SEM cross-sections of the S-ECC with AA concentrations varying from 0-5 wt% was imaged using SEM. Furthermore, modulated differential scanning calorimetry (MDSC), on the Ag flakes treated with AA, at a heating rate of 1°C/min, with a modulation amplitude of ±1°C and a frequency of 10 seconds was used to characterize the reaction between the Ag flakes and AA.

Mechanical characterization of S-ECC

A single strip of S-ECC was stencil printed between two strips of Kapton tape 4-mils thick onto a Pyrex wafer. S-ECC strips were encapsulated in PDMS, Sylgard 184 (40:1) part A to B, by pouring degassed PDMS onto the wafer containing the S-ECC. The thickness of the PDMS encapsulant was controlled by weight. Following silicone cure at 60°C lifted-off from was accomplished using a razor blade. Dog-bone tensile specimens were cut using a razor blade, with dimensions in accordance with ASTM D412 standards. The electrical response under tensile elongation was measured using a Keithley 2000 and an Instron 5548 microtester. Resistance values were recorded at 250-ms intervals during tensile elongation at an extension rate of 10 mm/sec, to a maximum elongation of 30%. Cyclical electro-mechanical testing to tensile elongations of 30%, was measured. Finally,

the electro-mechanical response of the S-ECC was measured until failure under tensile load.

3.4.2 Results and discussion

Effect of AA on electrical properties of S-ECC

The high resistance of S-ECC results from minimal contact area between conductive fillers and low tunneling rates. Increasing the conductivity of S-ECC is possible by increasing the Ag filler loading past 80 wt%; however, at filler loadings >85 wt% mechanical properties of the composite deteriorate rapidly.

Low temperature sintering of silver nanoparticles with silver flakes is an effective approach to reduce contact resistance between fillers. Gao et al. reported ECC with resistivity of 7.5×10^{-5} Ω-cm, by sintered silver nanoparticles at 150°C for 3 h [193]. By synthesizing surfactant free Ag nanoparticles, Zhang et al. demonstrated ECC with electrical resistivity of 4.8×10^{-5} Ω-cm can be prepared at 180°C for 1 h [126]. Through surface functionalization of silver nanoparticles with diacids, resistivity of $5x10^{-5}$ Ω-cm has been achieved [133]. Despite the high electrical conductivity achieved, using these materials in real applications is difficult due to complexities with processing and high cost. These difficulties result because composites formed with silver nanoparticles are: expensive, complicated to produce, difficult to disperse and are hard to printing due to their high viscosity [194]. Therefore, conventional techniques of nanoparticle sintering are too difficult to process and to costly to be useful for low cost, printable S-ECC. We describe a simple, cost-effective approach to prepare highly conductive polymer composites using AA.

Preparation of printable S-ECC requires that the conductive fillers be stabilized by lubricants (typically fatty acid) to prevent the aggregation and to improve the dispersion of the silver flakes in a polymer matrix [81]. These fatty acids assemble on the surface of the silver flakes by forming a Ag salt [195]. The presence of these fatty acids on the surface of the Ag flakes minimizes metallic contact between flakes. AA enhances the conductivity of the S-ECC by reducing the silver salt, silver carboxylate, on the surface of the silver flakes. The reduction of silver carboxylate has two roles in enhancing the conductivity of the composite. First, the reduction process removes the fatty acid surfactants, decreasing the tunneling barrier and increasing contact between flakes. Secondly, the reduction process forms small nano/submicron-sized particles on the surface of the silver flakes. These *in-situ* formed nano/submicron-sized particles have a high surface energy and are not stabilized by surfactants. Thus these *in-situ* formed particles are thermodynamically unstable. The thermodynamic instability of these *in-situ* formed particles causes the particles to sinter at low temperatures (<150°C). The sintering process reduces or eliminates contact resistance between flakes, enhancing the conductivity and reliability of the S-ECC. S-ECC prepared with 2 wt% AA had a much lower resistivity ~$2x10^{-4}$ Ω-cm, compared to the unmodified formulation which has a resistivity of ~$7x10^{-4}$ Ω-cm. The affect of AA on the morphology of the Ag flakes can be seen in Figure 32A-C. This figure shows the morphology and structure of the virgin Ag flakes and after being treated with AA for 10 minutes and 30 minutes respectively. As seen in Figure 32, the virgin flakes have a smooth surface morphology with definitive edges. After treating with AA for 10 minutes, the surface of the flakes become rougher and small circular offshoots can be seen on the edges of the flakes. With increasing

treatment time to 30 minutes, these small offshoots merge, forming metallic bridges connecting neighboring flakes together. These metallic bridges can be seen in Figure 32C outlined by the grey triangle and squares. The presence of these metallic bridges metallurgically interconnects the flakes, eliminating tunneling resistance and maximizing contact area.

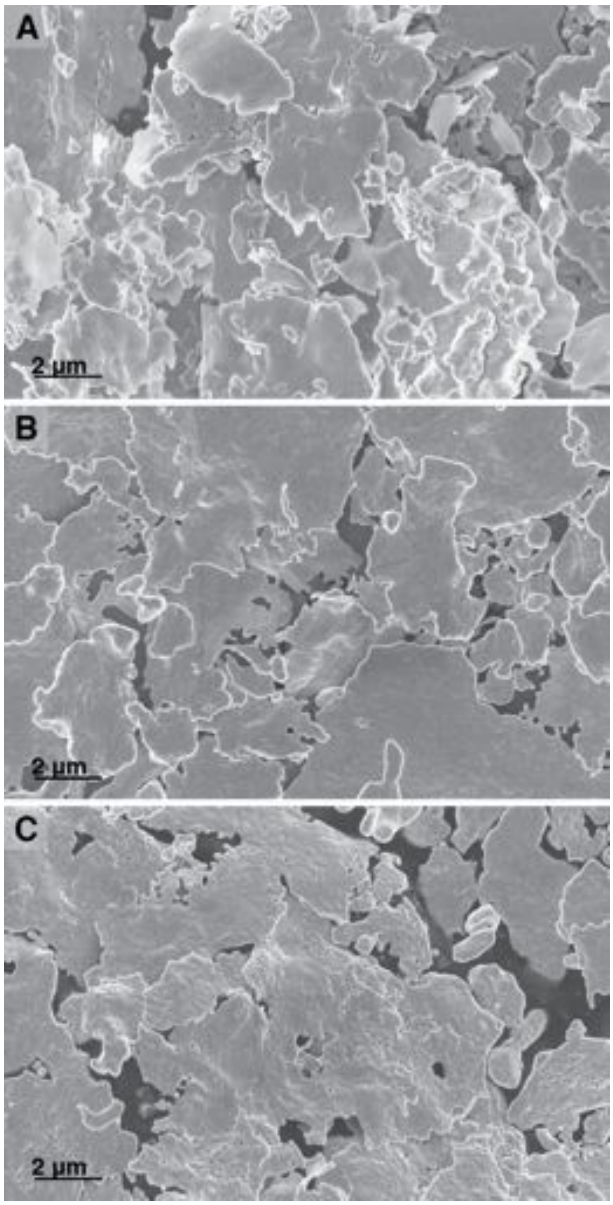

Figure 32. SEM image showing morphology of Ag flakes A. Virgin B. Treated at 150°C for 10 min and C. Treated at 150°C for 30 min A.

MDSC of virgin flakes (Figure 33A) indicates that the fatty acid surfactant started to desorb from the surface at 147.75 °C, however at a very slow rate. The peak desorption temperature was found to be 187°C. Furthermore, it was found that desorption completed at temperatures >200°C. Extracting the reversible and non-reversible heat flow from the MDSC signal, it was found that the desorption process is an irreversible process. This makes sense since the surfactants decomposed following desorption. With the addition of AA the onset temperature, peak temperature and completion temperature for the desorption were downshifted to 110°C, 134.5°C and 140°C respectively (Figure 33B). Both the peak structure and shape were the same for the virgin and AA treated flakes. Furthermore, in the MDSC of the Ag with AA there is an endothermic peak at 192°C, corresponding to the boiling of AA. From the MDSC it is evident that this peak is reversible, however the peak corresponding to the surfactant desorption is irreversible.

These results conclusively show that the addition of AA facilitates the decomposition of Ag salt associated with the bonding of fatty acids surfactants during curing. The reduction of the Ag salts causes the formation of highly unstable nanoparticles, which will readily sinter, increasing conductivity of S-ECCs. Thus the addition of AA provides a simple solution to prepare highly conductive printable S-ECCs.

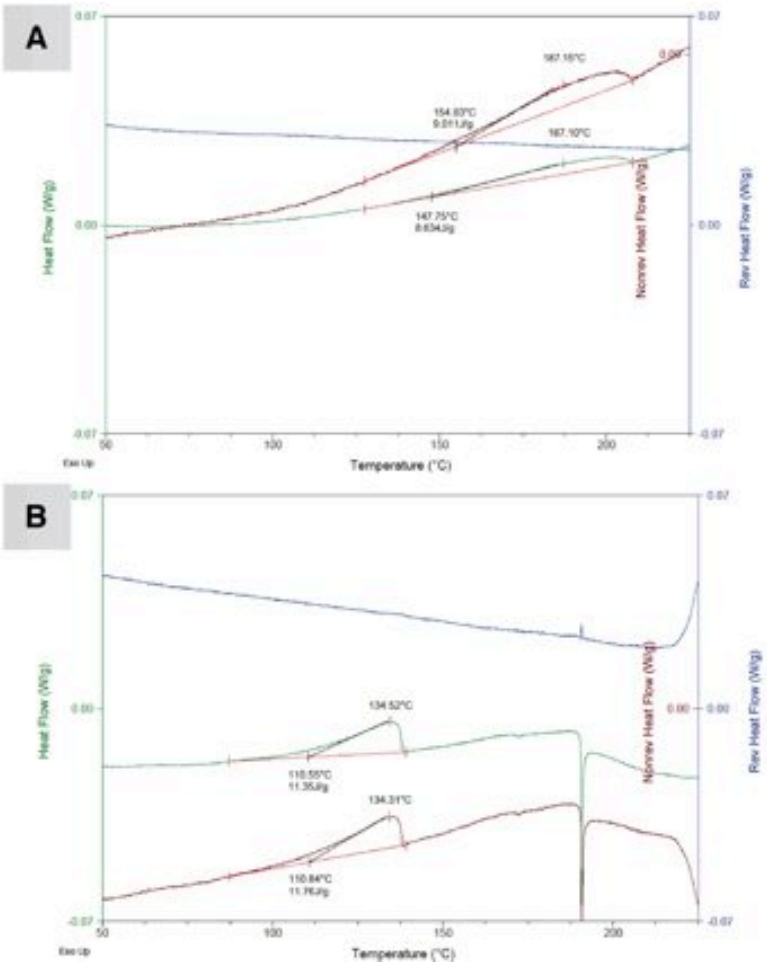

Figure 33. MDSC of A. Ag flakes B. Ag flakes with AA.

Mechanical characterization of S-ECC

Simultaneous tensile and electrical resistance measurements were measured as described in the experimental methods. The results from these experiments are shown in Figure 34. During the first trial the resistance of the S-ECC remained relatively constant up to tensile strains of $\varepsilon = 0.3$. However, following the first tensile experiment, the tensile strain caused the anisotropic silver flakes to align. The strain induced reorganization caused the resistance of the composite to increase. However, subsequent tensile strains of $\varepsilon = 0.30$ had no additional effect on the resistance. Thus, after the initial

reorganization, the composite is insensitive to repeated tensile strains of 30%. Following repeated tensile strains to 30%, the change in electro-mechanical response of the S-ECC was measured as the sample was strained to failure. The tensile-electrical measurements of the pre-strain, dog-bone specimen during strain to failure showed the resistance of the S-ECC initially decreased and then increased until finally failing at a strain of $\varepsilon = 0.70$. It is worth noting that failure was initiated in the encapsulating PDMS and not the S-ECC. Thus, it is likely that the composite itself could withstand tensile elongations of greater than 70% without failing.

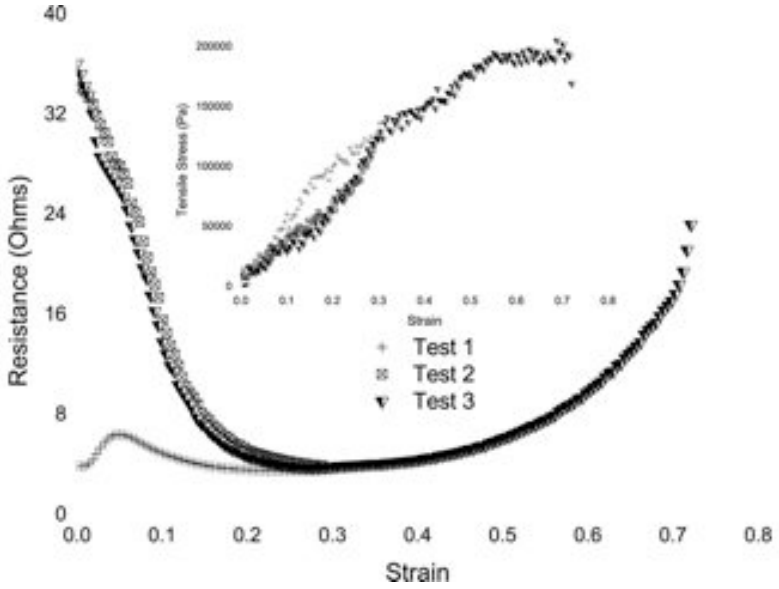

Figure 34. Graph of simultaneous tensile electro-mechanical characterization of silicone S-ECC. Inset: stress strain curve of dog bone tensile specimen [196].

We also manually tested the electro-mechanical response of the S-ECC under compression and during bending. There was no significant change in the conductivity of the S-ECC during repeated compression or bending.

Comparing this result to the 1st generation S-ECC (Figure 29) it appears that this 2nd generation material has worse electro-mechanical response; however, this is not the

case. The lower measured resistance and worse electro-mechanical response was related to variations in the preparation methods. For the tests conducted on the 1st generation S-ECC the conductor was twice as thick (200 μm) and prepared by inlaying the conductor within a predefined inlay in PDMS. Furthermore, when preparing the mold in the 1st generation material, we used a non-stoichiometric ratio of reactant. Thus in the mold there was an excess concentration of hydride functional groups. This excess concentration of hydride functional groups on long chain molecules would readily react with the excess concentration of vinyl groups in the S-ECC formulation, leading to improved adhesion and load transfer during elongation. The improved load transfer creates a more uniform distribution of stress in the S-ECC, minimizing maximum local strain. A third reason for the seemingly improved response of the 1st generation S-ECC was caused by difficulties associated with printing the S-ECC onto the PDMS mold. Because the printing process was difficult the surface morphology had large built in geometry, which can accommodate strain. Thus the true strain in the material was much less than the observed strain. On the other hand, the samples prepared for testing of the 2nd generation material were prepared by an encapsulation and lift off process. In this process, the S-ECC was cured first, resulting in a highly cross-linked material. This material does contain excess reactive vinyl groups. Thus following encapsulation the adhesion of the S-ECC to the PDMS encapsulant was not as strong as in the first generation material. The S-ECC was weakly bonded to the PDMS encapsulant but could easily be peeled off with a razor blade. This poor adhesion causes non-uniform stress distribution, creating local regions of large strain during mechanical testing. These local, high strain regions reduce the electrical and mechanical properties of the composite.

Furthermore, because the S-ECC was printed onto a glass slide the resulting surface was significantly smoother than the 1st generation samples. This smooth surface eliminated surface geometry, which can provide a false representation of the true strain in the composite. Finally, the process of transferring and encapsulation caused damage to the samples. Many samples that were highly conductive prior to transfer were non-conducting following transfer. For these reasons it is our belief that the 1st generation material is not better performing than the 2nd generation material, but merely the experimental methods used to test the 2nd generation material provide a more accurate representation of the true response of the material.

We hypothesize three approaches to improve the electro-mechanical response of the S-ECC. First, by incorporating high aspect ratio conductive fillers like carbon nanotubes and/or silver nanorods. A second method to improve the electro-mechanical response of the S-ECC would be to improve adhesion between the PDMS-encapsulant and the S-ECC to enhance load transfer and distribution. Finally, it is essential to improve the encapsulation process such that the S-ECC is not damaged during transfer.

3.5 Stretchable 3D interconnects using S-ECC

Typical stretchable electronic devices have been confined to planar designs. However, this designed limits the functionality and complexity of the devices which can be fabricated. Recently, there have been two publications focusing on fabrication of stretchable multilayer conductors but both have their limitation. The first approach, published by Guo and DeWeerth showed that 3D interconnects could be formed on PDMS through electro-beam deposition of Au onto PDMS [184]. However, their process involves many expensive cleanroom processes and the reliability of their device under

strain was excluded from publication. A second method, published by Niu et al. showed how bilayer stacks of stretchable conductive composites could be interconnected through the assembly of printed S-ECC photoresist [197]. However, their process again involved expensive cleanroom processes and their S-ECC had a very high resistivity of $4x10^{-2}$ Ω-cm [197]. Both these methods to prepare stretchable multilayer conductors show potential, however new processing methods to fabricate highly conductive multilayer S-ECC in a bench-top environment would increase the practicality of using this technology in real devices. In the following section we show how to make 3D structures of our S-ECC embedded in PDMS using only bench-top processes.

3.5.1 Fabrication of stretchable package

Three-dimensional stretchable packages were fabricated by spin coating Poly(methyl methacrylate) (PMMA) (Lucite International) on Pyrex wafers (Figure 35B). Strips of S-ECC were stencil printed in-between two pieces of Kapton tape 4-mil thick (Figure 35C). Similarly, circles of S-ECC 8 mm in diameter and 4-mil thick were stencil printed onto the PMMA coated Pyrex wafers using a micro-stencil (Mini Microstencil). The spacing of the circular patterns and strips had equal gap spacing such that the strips and the circular pattern could be aligned. These circular structures served as vias, interconnecting adjacent layers of S-ECC. Following patterning and curing of the S-ECC at 170 °C for 30 minutes, the S-ECC was encapsulated in PDMS (Figure 35D). The thickness of the PDMS encapsulant was controlled by weight. Following lift-off in acetone, the PDMS-encapsulated S-ECC was removed from the Pyrex wafer using a razor blade (Figure 35E). Bonding between patterned layers of S-ECC was accomplished

by depositing a small amount of uncured S-ECC on the surface of the printed circular "vias" of S-ECC (Figure 35F). The PDMS-encapsulated S-ECC and the wafer containing the circular "vias" were bonded at elevated pressure, at a temperature of 170°C for 30 minutes. Following curing of the S-ECC, PDMS was injected between the PDMS-encapsulated S-ECC and the Pyrex wafer containing the circular "vias" using a syringe (Figure 35G). The wafer was then degassed to remove air bubbles and the PDMS-encapsulant was cured at 60°C for 1 hour. The two-layer assembly was lifted off from the substrate in acetone (Figure 35H). This process was repeated alternating between the S-ECC strips and circular vias. The final structure produced is shown artistically in Figure 36.

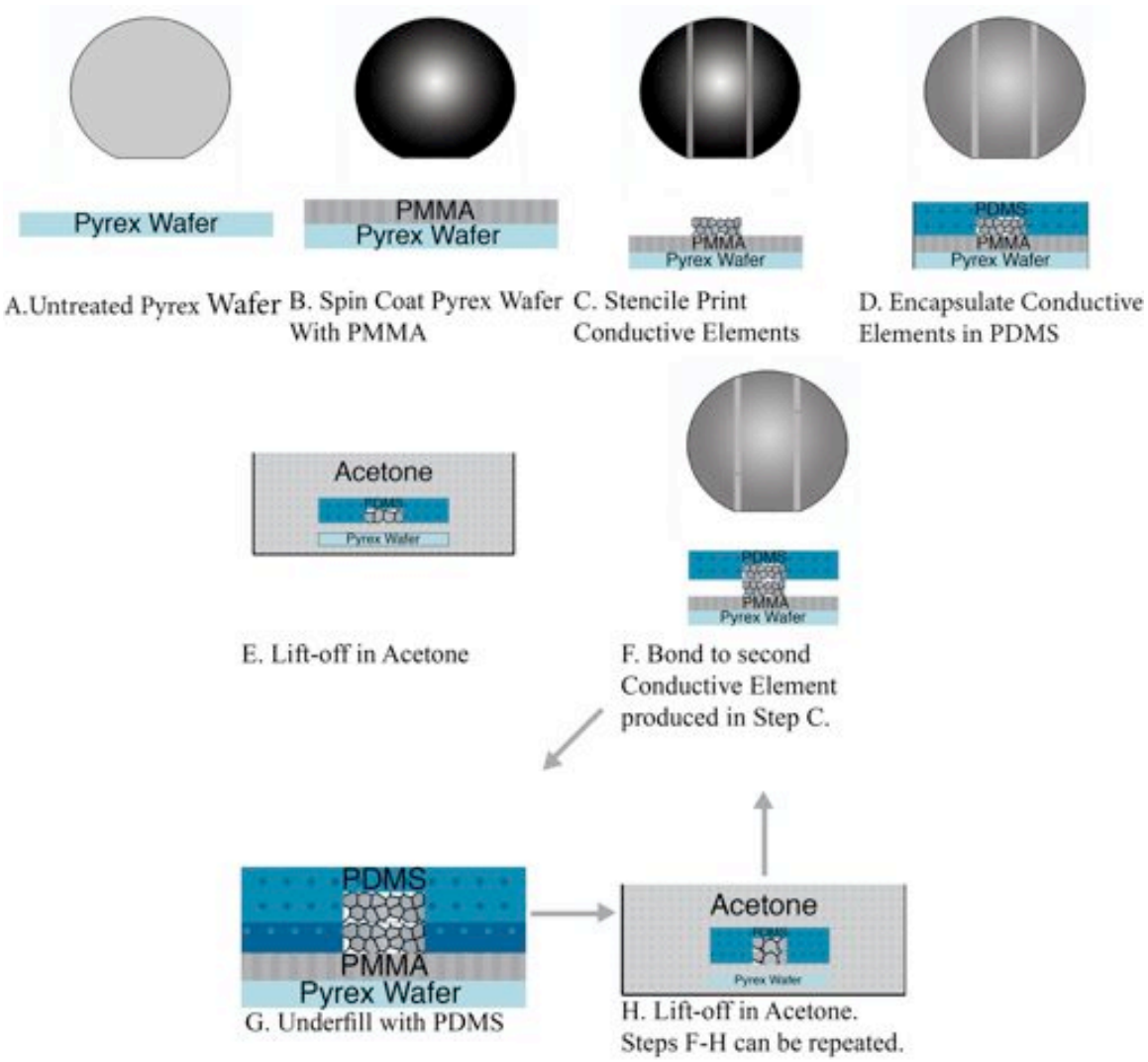

Figure 35. Schematic illustration of technique to fabricate 3D structures of S-ECC [198].

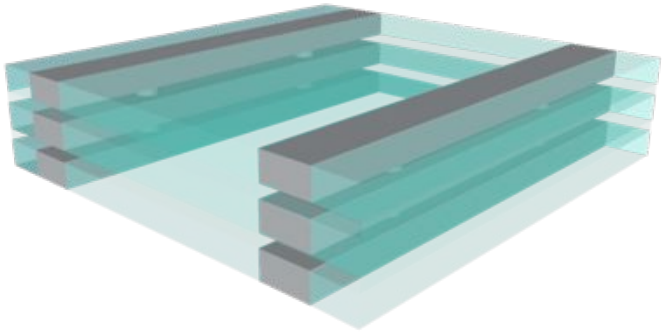

Figure 36. Schematic drawing of the fabricated 5-layer assembly of interconnected S-ECC [198].

Electrical conductivity of the fabricated 3D interconnects was measured using the four-wire method (Keithley Instruments). Cross-sectional images of the 3D interconnects were obtained using a 3D confocal microscope (Olympus Corporation). Coefficient of thermal expansion of the S-ECC and encapsulating PDMS was measured using a thermo-mechanical analyzer Model Q400 (TA Instruments). Dimensional changes in samples ~1 mm thick were measured as the samples were heated from room temperature to 200 °C, at a rate of 10°C/min using a thermo-mechanical analyzer Model Q400 (TA Instruments).

3.5.2 Results and discussion

We fabricated a 3-level assembly of encapsulated S-ECC as described in the experimental methods. Electrical characterization of the stretchable 3D conductive structures showed degradation with increasing levels of interconnection. The degradation in electrical properties associated with increased interconnection is likely the result of poor interconnection between layers or problems with the encapsulation process. However, cross-sectional 3D confocal micrographs of the structures showed no visual evidence of poor adhesion at the interface (Figure 37A). Because device failure is likely

to happen at the interface between two adjacent layers, it would be advantageous to use a different S-ECC formulation with improved adhesion and higher modulus such that the load is not accommodated by strain at the interface. Use of a different S-ECC formulation with improved adhesion could enhance the conductivity and reliability of the package.

Furthermore, to ensure that conductive paths on each level were isolated we took cross-sectional images using a 3D confocal micrograph. We found no evidence of inter-level connectivity other than at the vias. A representative cross-sectional image of the isolated levels in the 3D conductive structure is shown in Figure 37B.

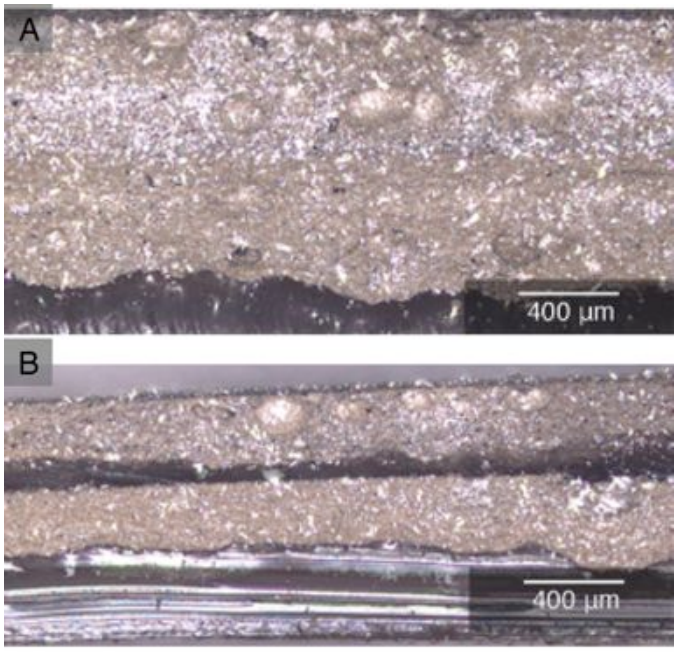

Figure 37. 3D confocal micrograph of A. Stretchable "via" like structures B. Electrically isolated layers within the stretchable conductive 3D package [198].

We characterized the linear coefficient of thermal expansion (CTE) (α_L) of both the S-ECC and the encapsulating PDMS using Thermo-mechanical analysis (TMA). A plot of the dimensional change as a function of temperature for the PDMS-encapsulant

and the S-ECC is shown in Figure 38. Ideally, the CTE for both the S-ECC and the encapsulating PDMS should be equivalent to minimize stress at the interface and to prevent warpage. We found that the PDMS-encapsulant used had a high CTE of 506.6 μm/(m °C). The S-ECC had a significantly lower CTE because it contains ~28 vol% Ag flakes, with a CTE of ~18 μm/(m °C). Experimentally, we found the CTE of the S-ECC to be 385.9 μm/(m °C). Even though the mismatch between these materials is large, CTE mismatch is less of a problem in stretchable electronics compared to rigid electronics, because S-ECC and PDMS-encapsulant is compliant. Thus S-ECC can accommodate the thermal-mechanical stresses. However, when preparing samples with a high areal density of S-ECC, in a non-centrosymetric pattern, there was noticeable warpage of the layup following successive thermal cycling. The warpage associated with the CTE mismatch between the S-ECC and the PDMS-encapsulant will make alignment challenging, especially as feature size is reduced. In future work, it is necessary that we tailor the CTE of the PDMS-encapsulant to match the lower CTE of the S-ECC. This can easily be accomplished through the incorporation of fillers into the S-ECC matrix.

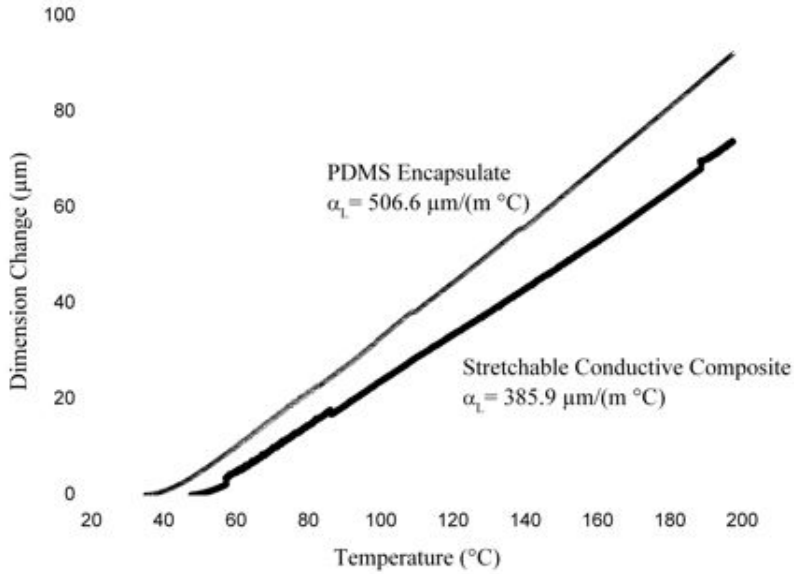

Figure 38. TMA of PDMS-encapsulate (sample size 1.161 mm) and stretchable conductive composites (sample size 1.2817 mm) [198].

We showed a method to fabricate multilayer S-ECC using a through silicone via methodology. Even though S-ECC is not ready for implementation in consumer devices, we show a simple, bench-top approach to fabricate 3D stretchable electrically conductive structures. This 3D stretchable package could be used to interconnect small discrete electronic devices, allowing electronic devices to be produced on a stretchable platform. Furthermore, this technology could be used succession with conventional microfluidic fabrication techniques to fabricate stretchable, solution processable, organic electronics allowing the fabrication of ultra-low cost stretchable electronics in a bench-top environment.

3.6 3rd generation stretchable electrically conductive composites

In our 3rd generation stretchable electrically conductive composite we abandoned the use of commercial PDMS formulations. Nearly all-commercial PDMS formulations contain inorganic fillers, which are used to increase the modulus and toughness of the PDMS. However, these fillers interfere with conduction pathway. In the following section we discuss formulation of a novel PDMS formulation ideal for use as a matrix for S-ECC. Furthermore, we modify the encapsulation method to enhance the electrical-mechanical response of the composite.

3.6.1 Formulation and characterization of PDMS matrix material

Obtaining virgin PDMS polymers from companies is challenging, most companies refuse to provide virgin polymers because they are not readily available and because it jeopardizes their intellectual property. Through negotiation with vendors we were able to obtain a wide variety of hydride and vinyl gums and fluids. Table 9 and Figure 39 shows the polymers that we were able to obtain for our formulations.

Table 9. Table showing the silicone polymers acquired.

Trade Name	Company	Functional Group	Degree of Functionality	Viscosity	Molecular Weight
1200A	Wacker	Vinyl	1.3 wt%	-	~110,00-120,000
V20,000	Wacker	Vinyl	1.3 wt%	20,000 cst	~48,000
V1000	Wacker	Vinyl	2.6 wt%	1,000 cst	~18,000
DMS-H41	Gelest	Hydride	Terminated	10,000 cst	~63,000
Poly(dimethylsiloxane), hydride terminated	Sigma-Aldrich	Hydride	Terminated	1,000 cSt	~24,000
Poly(dimethylsiloxane), hydride terminated	Sigma-Aldrich	Hydride	Terminated	-	~580
.1 M Platinum(0)-1,3-divinyl-1,1,3,3-tetramethyldisiloxane complex solution in vinyl terminated PDMS	Sigma-Aldrich	Pt Catlyst, Vinyl	Terminated	-	~24,000

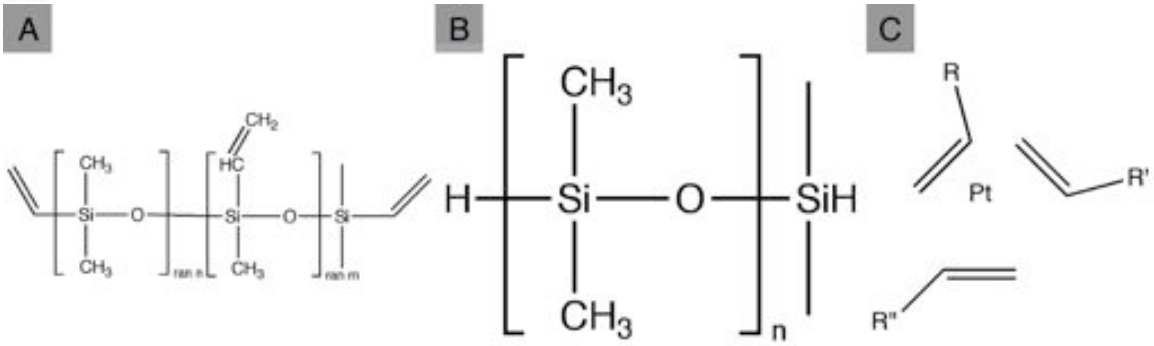

Figure 39. Molecular structure of A. Vinyl functionalized PDMS B. Hydride functionalized PDMS. C. Karstedt catalyst.

To quantify the properties of the PDMS matrix and resulting S-ECC a combination of Fourier transform infrared spectroscopy (FTIR), thermal mechanical analysis, differential scanning calorimetry, dynamic mechanical analysis, electrical characterization and simultaneous electro-mechanical testing was used.

Fourier transform infrared spectroscopy (FTIR)

FTIR is a useful technique to semi-quantitatively characterize the presence of specific functional groups. Table 10 shows the typical absorbance regions common in siloxanes and alkyl polymers.

Table 10. Typical absorption spectra for siloxanes and alkyl polymers [199].

Wavenumber (cm-1)	Functional Group
2975-2840	C-H stretch
2975-2950	CH_3 Asymmetric stretching vibration
2930	CH_2 absorption
2885-2865	Symmetric methylene group
2250-2100	SiH stretching vibration
985-800	SiH deformation
1290-1240	Si-CH_3 symmetric deformation vibration
~1410	Asymmetric CH_3 vibration
890-740	Methyl rocking vibration
1250-1220	
1020-1000	SI-CH_2-CH_2
970-945	
1250-1175	-Si-CH_2-CH_2
3700-3200	-OH stretch
1040-1020	SiOH deformation vibration
955-830	Si-O stretch for silanol

FTIR characterization of the polymers used was performed at ambient temperature with a FTIR spectrometer (Nicolet, Magna IR 560) using transmission mode. Figure 40 and Figure 41 show the FTIR spectra for the hydride terminated PDMS used. These spectra both show peaks at ~2130 cm^{-1} relating to the Si-H bond. The peaks magnitude was stronger for the Sigma Aldrich PDMS because it has a shorter chain length, thus it has a higher density of Si-H functional groups compared to DMS-H41. This is because DMS-H41 has a much longer chain length than the Sigma Aldrich PDMS.

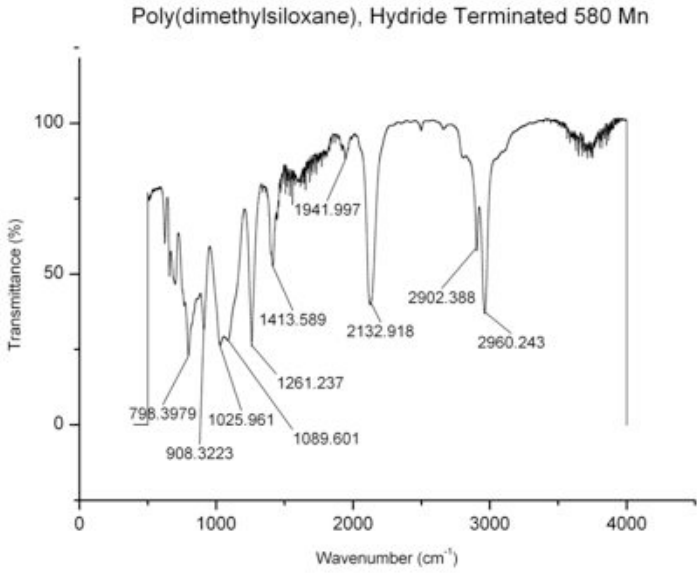

Figure 40. Sigma Aldrich (~580 Mn) hydride terminated PDMS.

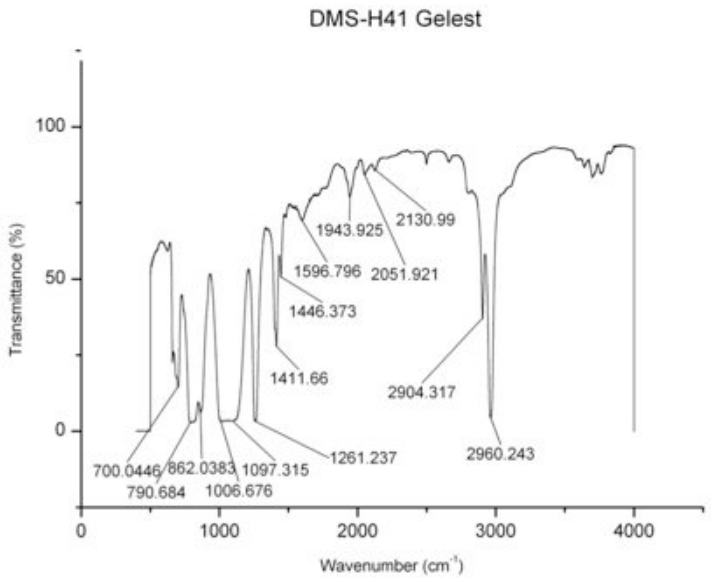

Figure 41. Gelest hydride terminated PDMS.

The FTIR spectra for the Wacker 1200A, vinyl functionalized PDMS, is shown in Figure 42. In the spectrum it is difficult to locate the presence of the vinyl group in the fingerprint region because it overlaps with other peaks. Thus the vinyl concentration could not be used to quantify the crosslinking density.

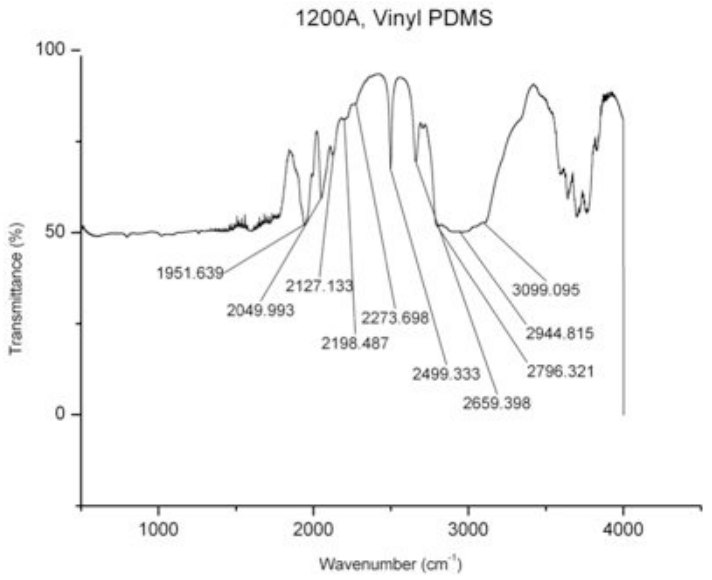

Figure 42. FTIR spectra of Wacker 1200A vinyl functionalized PDMS.

Comparison of the uncured formulations FTIR spectra (Figure 43) to the cured spectra (Figure 44) is difficult because the formulation used has a low crosslink density. Thus, there are very few reactive groups to produce signal. Because the absorbance of vinyl groups was indistinguishable, the hydride absorption peak was the only spectroscopic method available to quantify the reaction. Following curing, the magnitude of the hydride peak (~2130 cm^{-1}) decreases significantly, indicating hydrosilylation has occurred. The FTIR of the cured PDMS still shows evidence of silicone-hydride indicating that there is still unreacted hydride. This unreacted hydride is not the result of an excess amount of hydride, but rather the result of vitrification. The formulation was engineered to contain excess vinyl concentration to enable bonding during the transfer process. To confirm an excess concentration of vinyl functional groups molar concentration of hydride was increased 10 fold, and the resulting FTIR spectra was indistinguishable from the spectra obtained from the formulation used. Furthermore, the modulus of the composite increased.

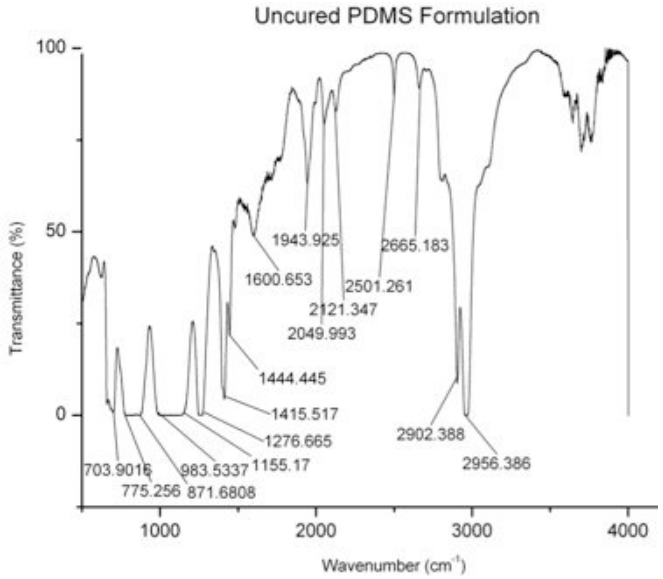

Figure 43. FTIR Spectra of the uncured PDMS formulation.

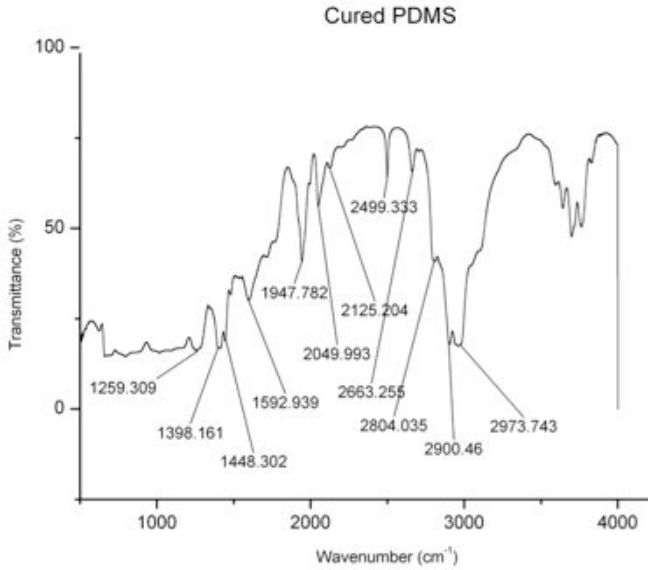

Figure 44. FTIR spectra of the cured PDMS formulation.

Thermal analysis of S-ECC

A combination of TMA, DSC and DMA were used to quantify the curing process, mechanical properties and response of the S-ECC.

The coefficient of thermal expansion is typically one of the most important parameters to quantify the reliability of electronic devices. Mismatches in CTE cause internal stresses, which can lead to device failure. In S-ECC, mismatches in CTE are less of a concern because internal stresses can be accommodated because the materials are compliant. However, the CTE plays a critical role in determining the conductivity of the composite. To obtain high conductivity requires that the S-ECC be cured in the expanded state. Thus it is important that the CTE of the matrix material is large. Furthermore, CTE of crosslinked polymers above their melting temperature provides a qualitative determination of crosslink density. The CTE of the composite is important for two key

reasons. First, it is important that the CTE of the composite is not too high because this will cause the composite to expand too much during heating, resulting in a decrease in particle contact and increase in resistivity. Secondly, if this technology is to be applied to large area arrays or 3D S-ECC it is desirable to have a match between the CTE of the composite and the encapsulant, to prevent warpage of the package and delamination of the layers. CTE of the polymer matrix, S-ECC and encapsulant was determined using a Q400 TMA (TA Instruments), equipped with a macro-expansion probe. The linear dimensional change of the sample was measured while the sample was heated from 50°C – 300°C at a rate of 5°C/min. Graphs of the linear expansion of the matrix material, S-ECC and encapsulant can be seen in Figure 45A-C respectively. From these figures the linear CTE was found to be 781, 558 and 248 μm/(m °C) for the matrix material, S-ECC and encapsulant respectively. PDMS is notorious for having an extremely high CTE and the matrix material used is no exception. The high CTE of the matrix produces a large compressive stress on the composite following curing at elevated temperatures. This large compressive stress results in a significant shrinkage in the S-ECC, enhancing the conductivity of the composite. The CTE of the S-ECC is significantly lower than the CTE of the polymer because of the inclusion of ~29 vol% of Ag flakes with a CTE of ~18.9 μm/(m °C). The CTE of the composite is still relatively high, which might contribute to a reduction in electrical performance at elevated temperatures. Finally, the CTE of the encapsulant was found to be much lower than the S-ECC. The lower CTE of the encapsulant is attributed to the high concentration of silica fillers used as toughners and the higher crosslinking density of the encapsulant compared to the matrix. Due to the

large mismatch in CTE between the composite and the encapsulant, it will be important to quantify the reliability of large area and 3D devices during thermal cycling.

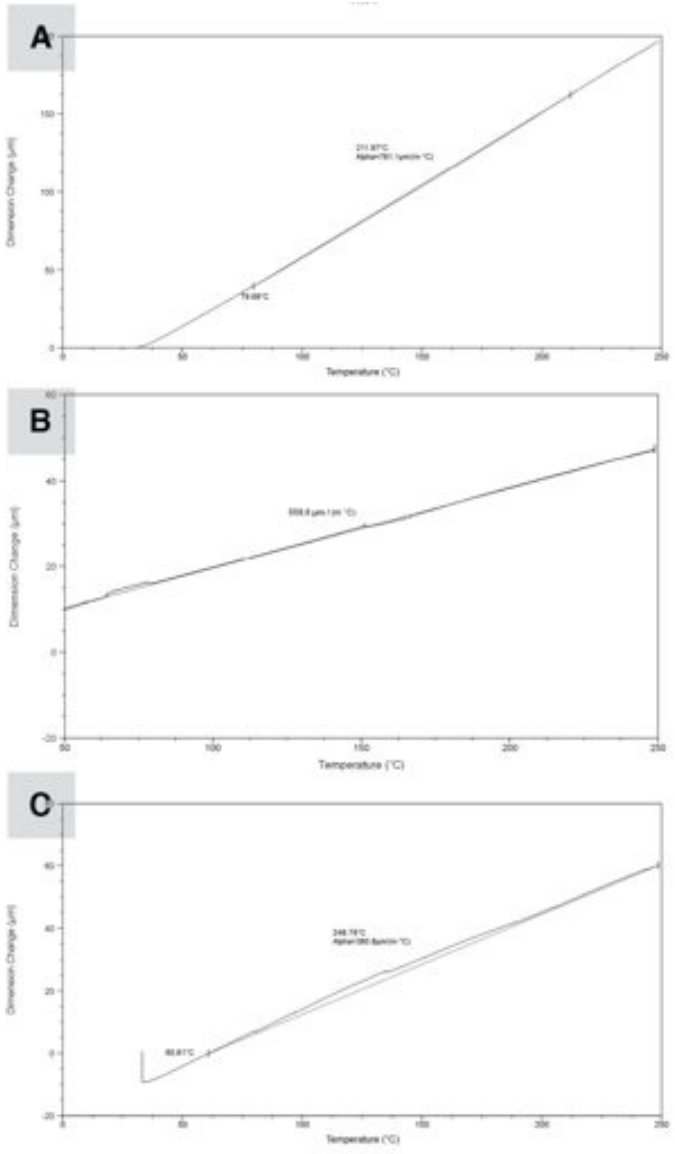

Figure 45. TMA of A. S-ECC matrix. B. S-ECC. C. PDMS encapsulant.

DSC was used to determine the curing temperature of the S-ECC matrix. DSC of the polymer matrix was conducted immediately after addition of the platinum catalyst. The curing point was measured by heating the sample at a rate of 10°C/min to 250°C. The resulting DSC plot is shown in Figure 46. From this experiment the reaction occurs

rapidly after reaching the onset temperature of 84.92°C. Typically hydrosilylation reactions can occur at room temperature; however the reaction rate is slow. By formulating the polymer such that curing does not occur until the melt is heated to elevated temperatures allows the composite to cure in the expanded state, resulting in a compressive stress upon cooling. This compressive stress increases the contact between fillers, increasing the conductivity of the composite. Future work focusing on inhibition of crosslinking reaction at low temperatures should result in increased conductivity of the composite.

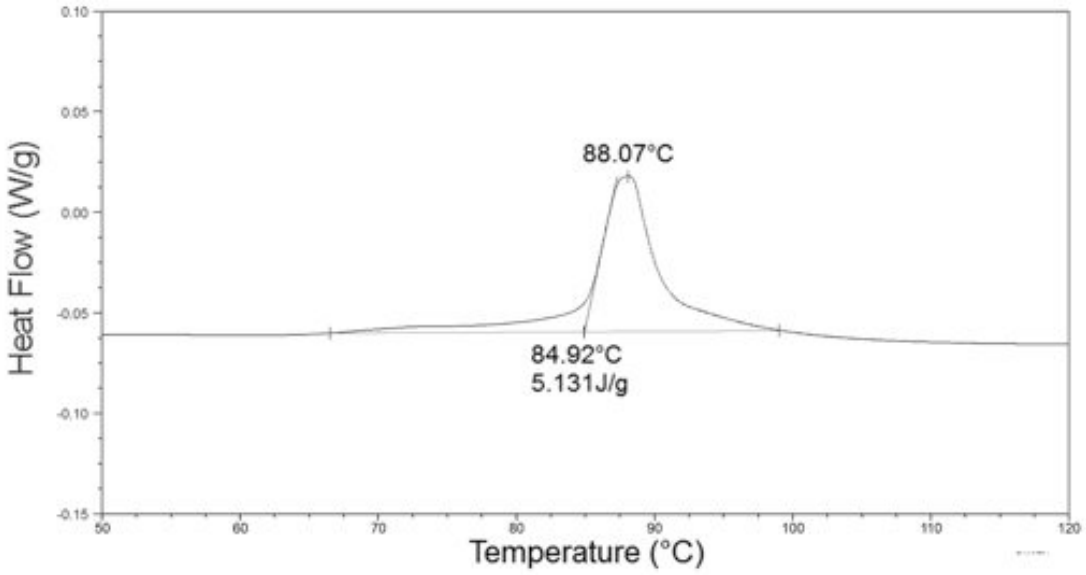

Figure 46. DSC showing the curing temperature of the PDMS matrix.

DMA is extremely sensitive to transitions in crosslinked PDMS. DMA operates by applying a sinusoidal stress or strain to a sample with a specific geometry. Because polymeric materials have both elastic and viscous response there will be a phase lag between the applied stress and the strain in the material. The frequency dependent stress and strain can be expressed as described in Eq. 18 and 19 respectively, where ω is the frequency of strain oscillation, t is the time and δ is phase lag between stress and strain.

$$\sigma = \sigma_0 \sin(t\omega + \delta) \quad (18)$$

$$\varepsilon = \varepsilon_0 \sin(t\omega) \quad (19)$$

From these equations it is possible to deduce the storage modulus (E') (Eq. 20) and loss modulus (E") (Eq. 21). The storage modulus is the energy stored due to elastic deformation and the loss modulus is the energy lost due to heat dissipation. From the storage modulus and loss modulus it is possible to define the phase angle tan(δ) as shown in Eq. 22.

$$E' = \frac{\sigma_0}{\varepsilon_0} \cos(\delta) \quad (20)$$

$$E'' = \frac{\sigma_0}{\varepsilon_0} \sin(\delta) \quad (21)$$

$$\tan \delta = E''/E' \quad (22)$$

A typical method for DMA consists of applying a strain at a single frequency while heating or cooling. As the sample is heated the polymer undergoes a series of transitions depending on its temperature, thermal-mechanical history and molecular structure. Typically there are 4 commonly recognized transitions that are observed from DMA of polymers. At extremely low temperatures polymer chains move only by local motion, however upon heating polymers undergo a transition, where there motion has increasing degrees of freedom associated with the ability of the bonds on the polymer chain to bend and stretch. This γ transition (T_γ) in DMA is recognized by a sharp decrease in modulus. As the temperature continues to increase, the polymer's free volume increases to the point where side groups on the polymeric chain can start to move. This β transitions (T_β) appears similar to γ transitions but occurs at higher temperatures. Finally polymers exhibit a glass transition (T_g), where the polymers undergo a transition from a solid-like to a viscous response. Glass transitions can be distinguished by a dramatic decrease in modulus. The decrease in modulus following a glass transition is significantly

greater than the change in modulus following T_γ and T_β, and always occurs at higher temperatures. Once passing through T_g the modulus either reaches a rubbery plateau, if the polymer is crosslinked, or the polymers modulus decreases rapidly upon reaching its melting point. An idealized plot of common transitions found during DMA is shown in Figure 47.

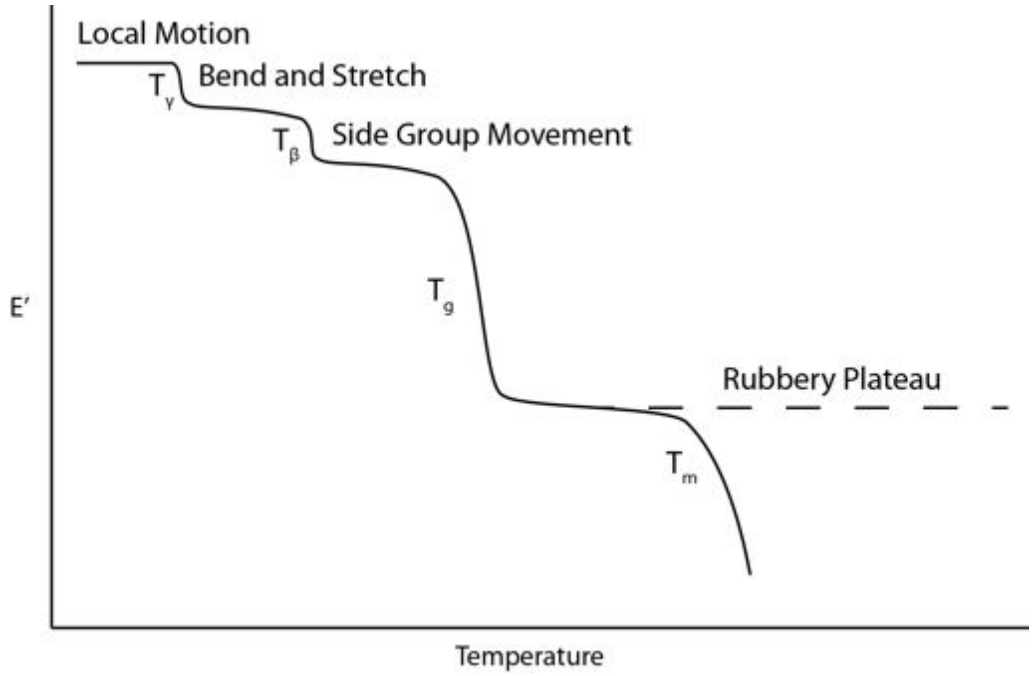

Figure 47. Idealized plot of polymeric transitions in DMA during a temperature sweep experiment at a constant oscillation frequency.

DMA provides two methods of quantifying the crosslink density of silicone. The first method based on the theory of rubber elasticity; this model assumes a direct correlation of the modulus of the polymer at $T > T_g$ and the molecular weight between crosslinks. According to this theory, the density of crosslinks (ρ) can be defined by Eq. 23, where G' is the shear storage modulus, R is the gas constant and T is the absolute temperature at which the modulus is determined [200]. The glass transition temperature

can also be used as an indicator of the crosslink density as shown in Eq. 24, where T_g is the glass transition temperature, T_{g0} is the glass transition temperature of the resin, K is a constant and M_c is the molecular weight between crosslinks. However, this method is less accurate because it requires knowledge of the glass transition temperature of the uncured resin, which changes with formulation.

$$\rho = \frac{G'}{RT} = \frac{E'}{3RT} \tag{23}$$

$$T - T_{g0} = \frac{K}{M_c} \tag{24}$$

DMA of the cured S-ECC was conducted using a 2890 DMA (TA instruments) using the film-tension mold. Specimens were prepared by printing strips of ECA 400 μm thick between two pieces of Kapton tape. Following printing, the S-ECC was easily removed with a razor blade. Testing was conducted by initially cooling the composite to -145°C at a rate of 2°C/min using the liquid nitrogen cooling system. Following cooling the specimen was held isothermally for 15 minutes before heating to 50°C at a rate of 2°C/min. During this experiment the sample was oscillated at a constant frequency of 1 Hz. The resulting graph from the DMA experiment is shown in Figure 48. From this graph there are two observed transitions. During cooling there are transitions at ~-62°C and ~-140°C. Both these transitions look identical but can be distinguished by the temperatures at which they occur. The transition at ~-140°C is likely the glass transition, where the transition at -62°C likely corresponds to the melting/crystallization of the polymer. During heating the same two transitions were observed. The difference in the glass transition temperature was relatively small, a couple of degrees and was likely the result of equipment imprecision. On the other hand, the melting/crystallization transition

during heating was at ~-30°C, >30°C higher than observed during cooling. This difference is related to requirement that the polymer be undercooled, to the point where nuclei can form, for crystallization to proceed.

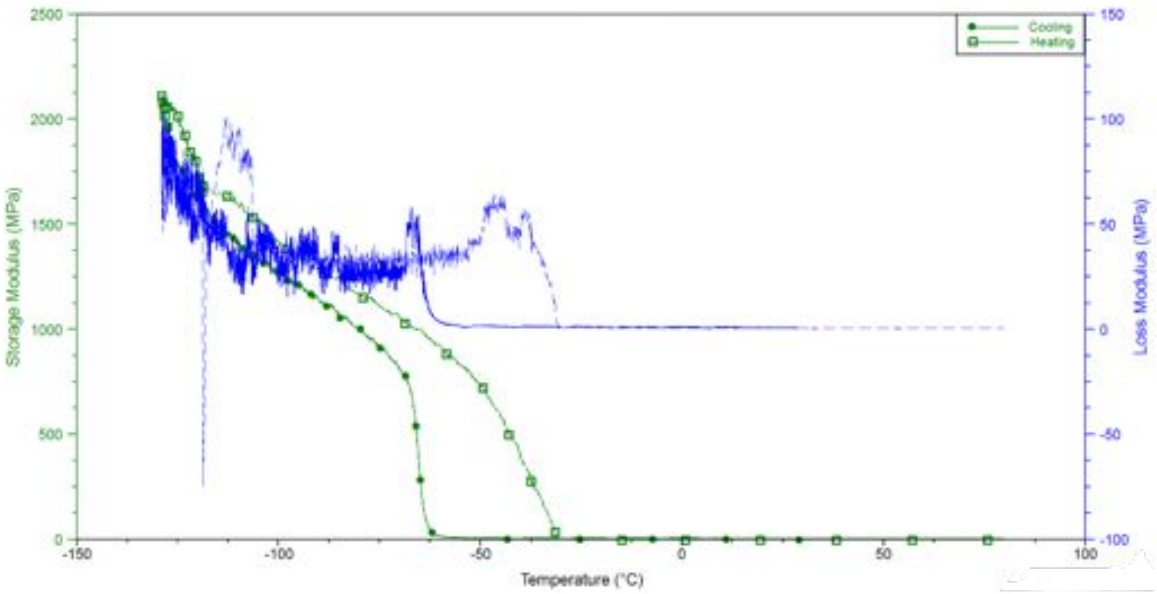

Figure 48. DMA of S-ECC during cooling and heating.

Confirmation that this higher temperature transition corresponds to a melting / crystallization transition was obtained using DSC (Figure 49). Upon cooling there is a clear crystallization peak with an onset temperature of -65°C. The onset temperature corresponds well with the first transition observed in DMA. This crystallization peak has a corresponding melting peak, with an onset temperature of -47.39°C. The melting was observed at a lower temperature than observed in DMA. A difference in observed transition temperatures between different characterization methods is common. This difference is due to differences in sensitivity of the technique to the transition of interest.

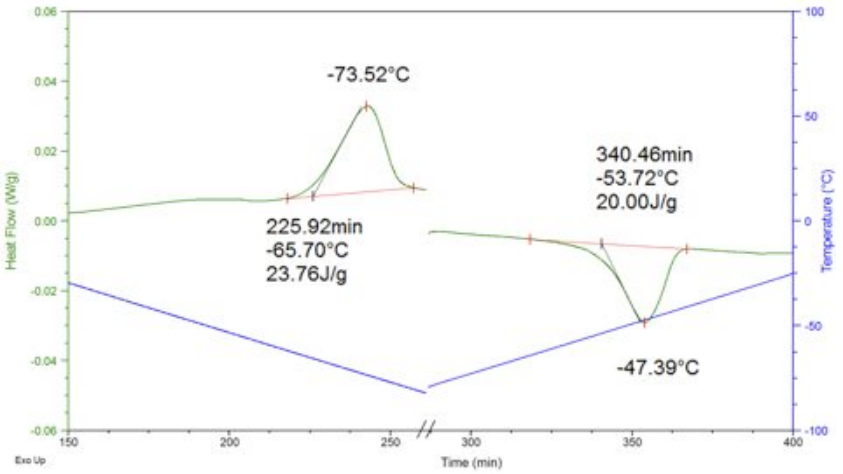

Figure 49. DSC of silicone matrix crystallization.

For S-ECC the ability of the rubber to crystalize is essential for its performance. During the stretching process, polymer chains will start to align. This alignment can cause shear-induced crystallization. Since crystallization increases the modulus of the composite, mechanically induced crystallization can be used as a method to evenly distribute the strain through the composite. If a local region experiences a large strain, shear induced crystallization will cause the modulus to increase locally. This increase in local modulus will protect this region from further strain, as lower modulus regions will accommodate the stress. An ideal S-ECC will undergo localized plastic deformation during stretching. Provided there is sufficient adhesion to the encapsulating substrate, the resulting plastic deformation creates surface geometry, which can accommodate repeated strains without any further damage to the composite. Thus the shear induced crystallization process plays an essential role in evenly distributing the strain, maximizing stretchability and reliability.

3.6.2 Scanning electron micrograph of S-ECC

Scanning electron micrographs were taken using a LEO 1530 SEM. These images were used to visualize the particle dispersion, surface morphology and effect of applied strain S-ECC structure. Figure 50A-B shows the top surface of the virgin S-ECC and the top surface of the S-ECC modified with AA respectively. Looking at the two images, both appear to be relatively homogeneous. The flakes appear to have no preferred orientation. One key difference between the AA treated and virgin S-ECC is the morphology of the composite. In the virgin S-ECC, the flakes are clearly visible and the polymer tends to occupy channels between the flakes. On the other hand, in the AA treated sample, the flakes are hardly visible. It appears that polymer wets the surface of the flakes in the AA modified formulation. This observation is expected because AA, as previously shown, removes the surfactant from the surface of the Ag flakes. Without being stabilized by a surfactant, the Ag flakes have a very high surface energy, thus there is a strong driving force for the silicone, with a low surface energy, to wet the surface of the Ag flakes. Wetting of the surface of the flakes typically would be detrimental to the electrical conductivity because it would interfere with the contact between fillers. However, since contact and sintering occurs prior or simultaneously with the removal of the surfactant, surface adsorption does not affect the electrical conductivity of the composite. Furthermore, the addition of AA enhances the mechanical properties of the composite because the increased wetting of the conductive fillers aids in stress distribution. Proper stress distribution in composites is extremely important because it reduces the number and magnitude of high stress regions, preventing premature failure of the composite.

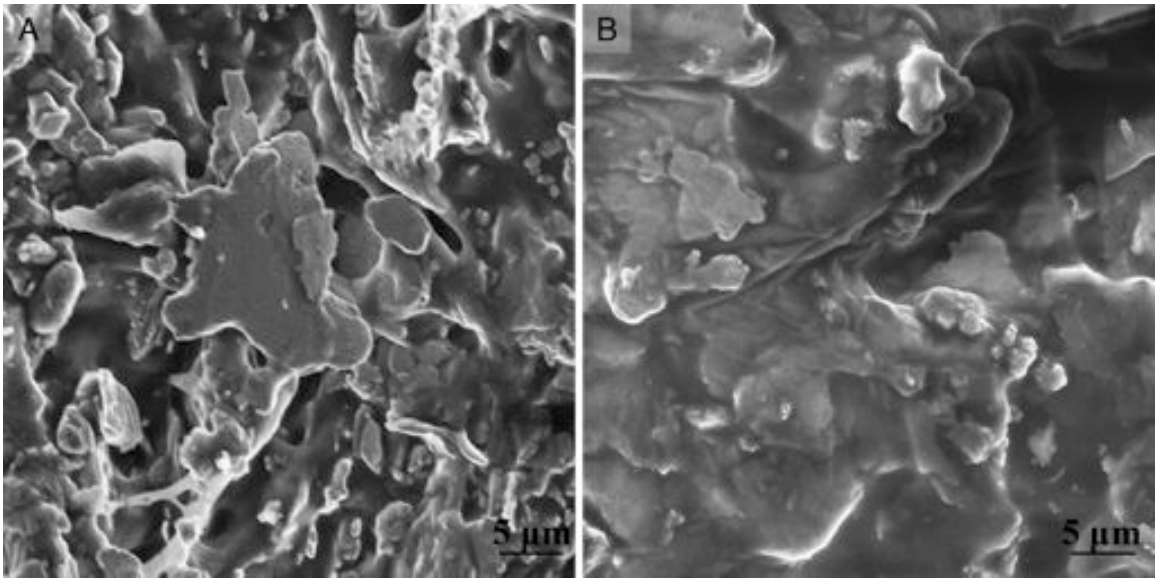

Figure 50. SEM image of top surface morphology of A. S-ECC B. S-ECC with AA.

Figure 51 shows cross sectional images after the S-ECC was strained to 50% 5000 times. Figure 51A-B show the cross-section of the strained composite parallel to the tensile direction for virgin and AA treated formulations respectively. From these images it is evident that the flakes start to align after repeated tensile strains. The Ag flakes anisotropic shape and the resulting compressive stress, in the transverse direction, causes the alignment of the Ag flakes, during tensile strain. As the flakes align and are compressed, contact between the Ag flakes is increased, enabling stable or even enhanced electrical conductivity during straining. Furthermore, as depicted in Figure 51A-B, the degree of alignment is more pronounced for small highly anisotropic flakes compared to larger uniformly shaped flakes. Figure 51C-D show cross-sectional images of the stretched S-ECC in the direction perpendicular to the applied strain, for virgin and AA treated flakes respectively. In these images there is no evidence of alignment or ordering of the flakes. However, it is likely that the flakes have out of plane alignment but this cannot be determined without taking serial crosssectional images.

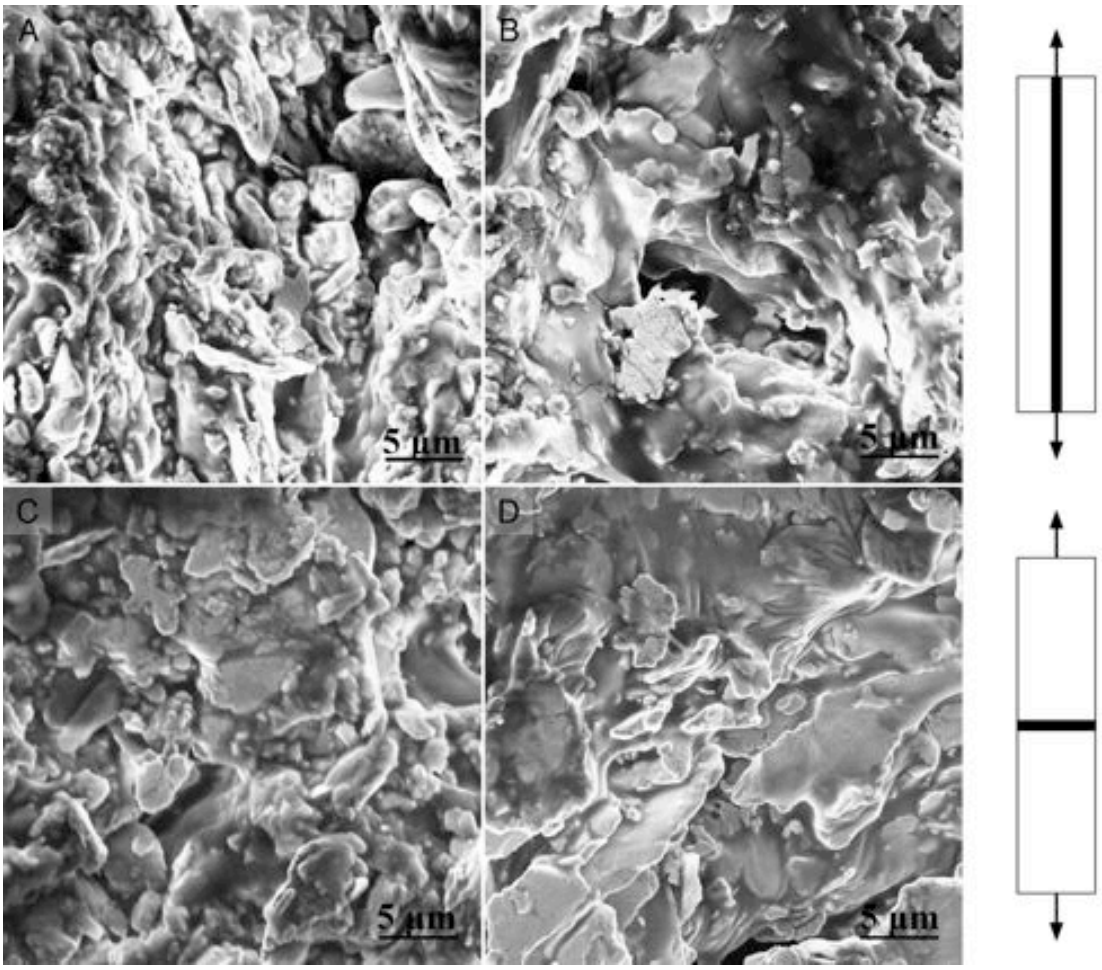

Figure 51. SEM cross-sectional images of S-ECC after 5,000 cycles to tensile strain of 50% A. Parallel to strain direction in virgin formulation. B. Parallel to tensile strain AA treated flakes. C. Perpendicular to tensile strain virgin formulation. D. Perpendicular to tensile strain AA treated.

Figure 52A shows the surface topography and the perpendicular cross section of an S-ECC after being stretched 5000 times to 50% elongation. From this image alignment on the top surface is evident, where the flakes in the perpendicular cross-section appear randomly dispersed. Furthermore, the flakes on the top surface appear to be arranged in a shingle like fashion, such that when stretching each flake slides on the surface of another. This surface geometry aids in the material's ability to stretch without deterioration of its

electrical performance. Figure 52B shows the top surface of AA treated S-ECC while being strained to 30%. In this image the polymer can be seen stretching around the silver flakes. When stretching, the polymer forms striations in the composite. These striations are caused by the stress associated with the polymer trying to compress the undeformable Ag flakes. To relive some of this stress the flakes will rotate giving rise to the observed anisotropic orientation.

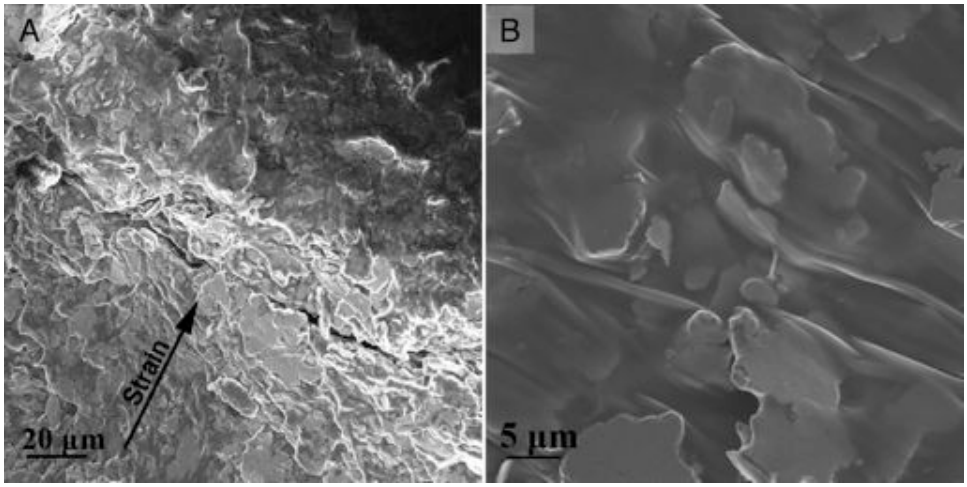

Figure 52. SEM image showing A. surface topography and perpendicular cross section of S-ECC after 5000 tensile elongations to 50%. B. Surface of AA treated S-ECC strained to 30%.

Another strange observation when looking at the SEM images of the virgin formulation was that there was surface reconstruction of the Ag flakes, similar to when AA was used (Figure 53). The observed surface reconstruction was modest in comparison to samples treated with AA, but was still significant enough to enhance the conductivity of the composite. It was found through DSC, that the hydride terminated PDMS can reduce the silver salt, formed by the surfactant, at ~132°C, generating silver nanoparticles. The reduction process in the presence of hydride terminated silicone

occurs at a temperature halfway between the desorption temperature in the presence of AA (~110°C) and the desorption temperature in air (~153°C).

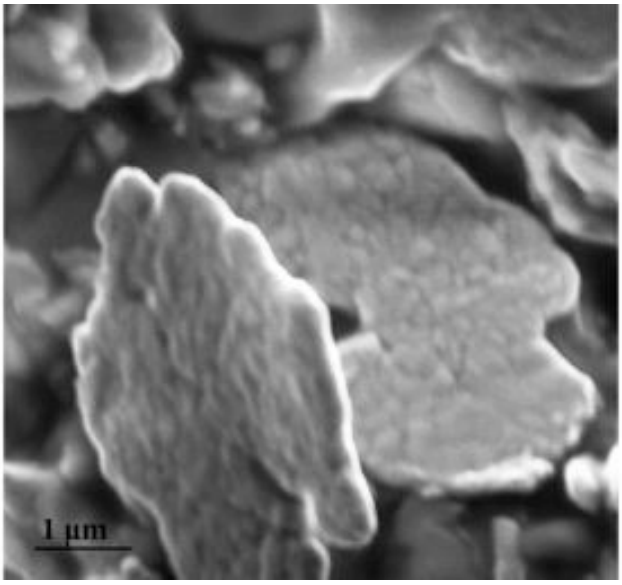

Figure 53. Surface morphology of Ag flakes in virgin composite formulation.

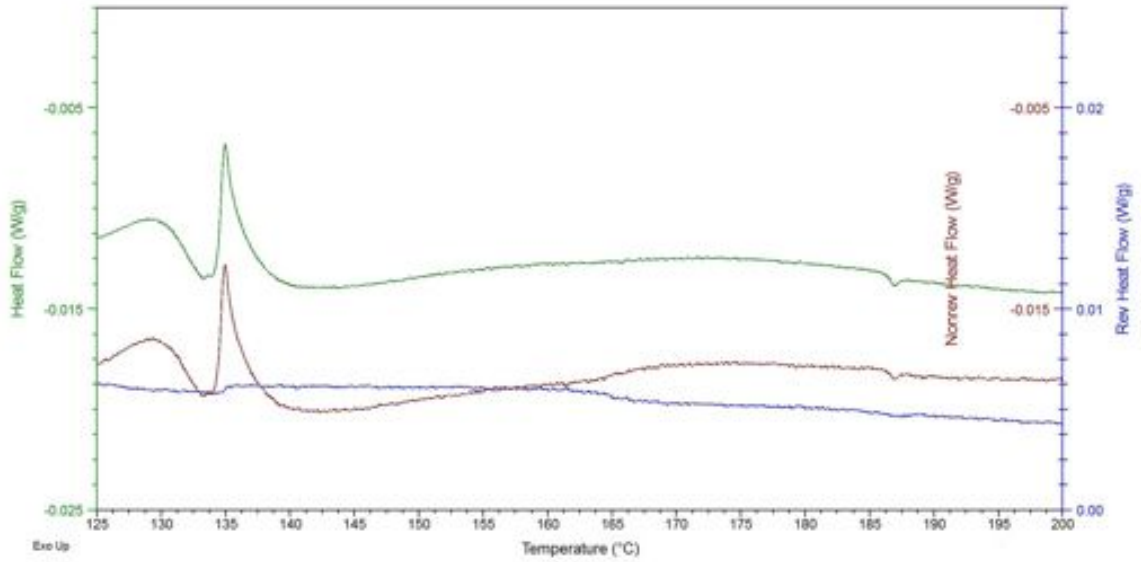

Figure 54. Reduction of surfactant by hydride-terminated silicone.

Electrical properties of S-ECC

The bulk resistivity of the prepared S-ECC were characterized as described in Appendix A. Initially, the effect of curing temperature on the bulk resistivity was determined. It was found that the bulk resistivity was minimized by rapidly curing the composite at 150°C. Curing at 150°C resulted in a composite with a bulk resistivity of 7.51×10^{-5} Ω-cm. Curing at lower temperatures limited the expansion of the polymer prior to curing, minimizing the resulting compressive stress upon cooling. On the other hand, curing at temperatures greater than 150°C resulted in the composite curing too rapidly, which prevented the fillers from establishing good contact prior to gelation. A plot of the measured bulk resistivity as a function of curing temperature can be seen in Figure 55.

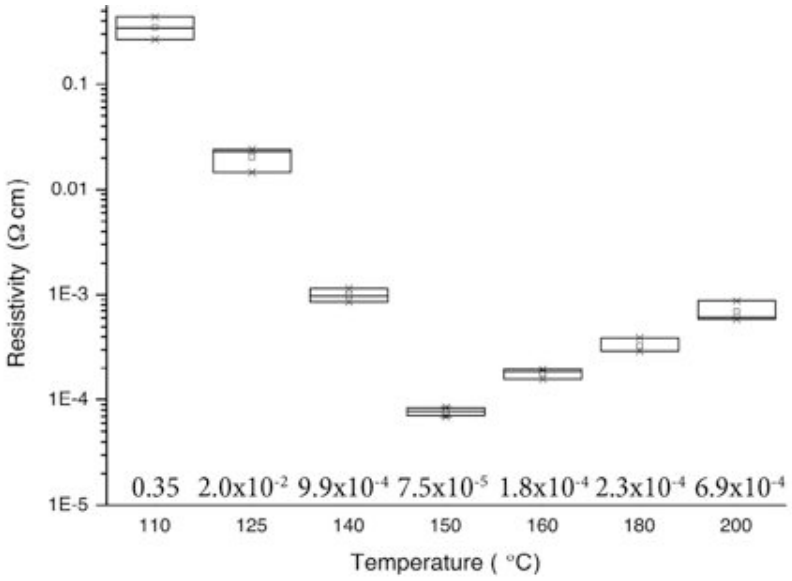

Figure 55. Graph showing S-ECC resistivity as a function of curing temperature.

Unlike epoxy-based ECC, having the highest possible crosslinking density does not result in improved mechanical and electrical properties in silicone S-ECC. In S-ECC the crosslinking structure needs to be able to accommodate large strains, have high

toughness and tear strength and support a highly conductive ECC. Thus it is not ideal to have the maximum possible crosslinking density, because it will result in undesirable mechanical properties. Figure 56 shows the electrical resistivity of the composites as a function of crosslinking density. There is an observed trend that as cross-linking increases the conductivity decreases. Actually, the opposite trend is observed: the electrical conductivity tends to increase with decreasing crosslinking density. This difference is related to the difference in the mechanism resulting in shrinkage. For conventional ECC a majority of the shrinkage results directly from the crosslinking reaction. However, hydrosilylation reactions are notorious for having minimal shrinkage upon curing. Instead, when curing at elevated temperatures, PDMS will expand. Following crosslinking and cooling the polymer chains will collapse giving rise to a compressive stress on the composite. The magnitude of the collapse is directly correlated to the molecular weight between crosslinks. Thus as the crosslinking density decreases compressive stress on the composite increases. Formulation 98 had the lowest possible crosslinking density while having sufficient modulus and abrasion resistance necessary for real applications. The S-ECC prepared with AA showed uniformly lower resistivity than the unmodified formulation. This decrease in resistivity was associated with a change in the surface morphology, the formation of nanoparticles and sintering. Because AA enables the sintering of neighboring flakes the effect of crosslinking density / shrinkage was noticeably less significant than in the unmodified formulations. Moreover, it was found that the efficacy of AA to enhance the conductivity in silicone S-ECC was significantly less than in epoxy-based ECC. The reduced efficacy of AA in silicone-based S-ECC is due to silicone-hydrides' ability to catalyze the same chemical reaction as AA.

Based on these observations, the formulation labeled 98 showed the best electromechanical response and was the formulation used for the remainder of the experiments.

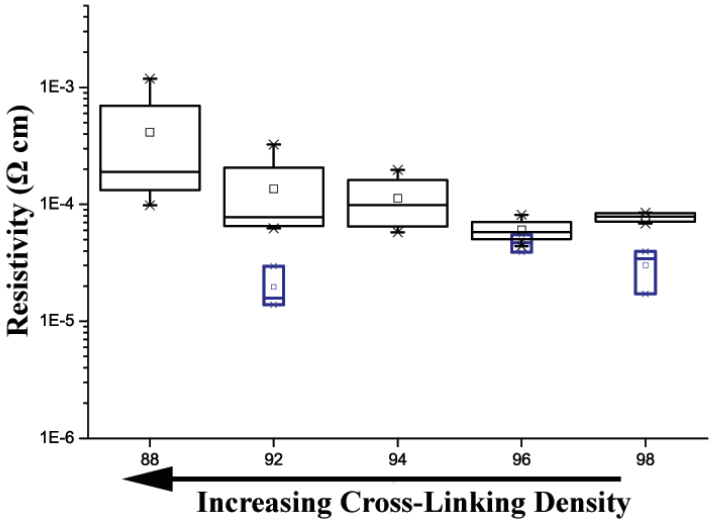

Figure 56. Electrical conductivity of S-ECC as a function of Relative vinyl concentration. Black box plots are for virgin formulations and the blue boxplots are for AA treated formulations.

Encapsulation and transfer of S-ECC

One of the most difficult challenges to prepare S-ECC was finding the proper encapsulant. The ideal encapsulant has good elasticity, high toughness, tear strength, excellent adhesion and transfer resolution. In previous experiments we used RTV-2 liquid silicone rubbers as the encapsulant. However, these encapsulates do not provide sufficient adhesion, even after modification of the vinyl-hydride ratio. By using a peroxide cured silicone encapsulant, excellent adhesion between the silicone encapsulant and the composite could be obtained. This improved adhesion is the result of increased

chemical crosslinking between vinyl groups in the encapsulant and excess vinyl groups in the composite, without any competitive crosslinking reactions.

Electrical mechanical response of S-ECC

The electrical mechanical response of the electrically conductive composite was determined by encapsulating conductive strips of S-ECC as previously described. Strips of S-ECC 100 μm thick encapsulated in PDMS 400 μm thick was cyclically strained to 50% tensile strain using an Instron 5548 microtester (Instron Corp.). Simultaneous Electrical measurements were taken by attaching Ni foil to the surface of the S-ECC between the clamps. The electrical resistance was measured at 150 ms intervals using a Kiethley 2400 source meter using a four-point method. The graph shown in Figure 57, shows the electrical resistivity when applying cyclical tensile strains to 50% elongation. From this figure, it is observed that the electrical resistivity of the composite increases slightly during the initial 10 percent of strain. However, after straining 10%, the electrical resistance remains relatively constant. The electrical response showed some variance between the elongation and recovery process. Prior to elongation the conductivity of the composite was minimized, however upon stretching the resistivity of the composite increased and then decreased. This increase in resistance is associated with the flakes initially sliding. As the flakes slide on the surface the contact area between flakes is reduced, increasing the resistivity. However, as the tensile strain increases the compressive force on the composite in the transverse direction increases; this compressive force increases the contact between flakes resulting in a higher conductivity. Because the polymer matrix has a low crosslink density its response is more viscous than elastic. The viscous nature of the composite results in a time dependent recovery process.

Because the composite does not recover elastically, the compressive stress on the flakes remains during recovery. This residual compressive stress causes the composite to have a lower resistivity during recovery than elongation. However, upon returning to a stress free state the resistivity of the composite increases slightly. This increase in resistivity in the stress-free state is likely related to the reorientation of the flakes during straining and the long recovery time needed for the flakes to reorient to their pre-strained conformation. Despite these minute variations in the electrical response, these variations are rather insignificant even after the composite has been strained 1000 times to 50% elongation. The average resistivity value during tensile strains to 50% of ~$5x10^{-3}$ Ω-cm is an acceptable resistivity for many applications. Furthermore, this reported resistivity is a significant underestimate. The actual electrical resistivity of the composite is significantly lower than measured because the measured resistivity includes the resistance of the connecting Ni foil and contact resistance between the Ni foil and the composite. The sample measured using the four wire method prior to stretching had a bulk resistivity of ~$4.42x10^{-5}$ Ω-cm where after stretching 5000 times to 50% elongation the measured resistivity decreased to ~$2.6x10^{-5}$ Ω-cm. This decrease in electrical resistivity is related to the alignment of Ag flakes within the composite.

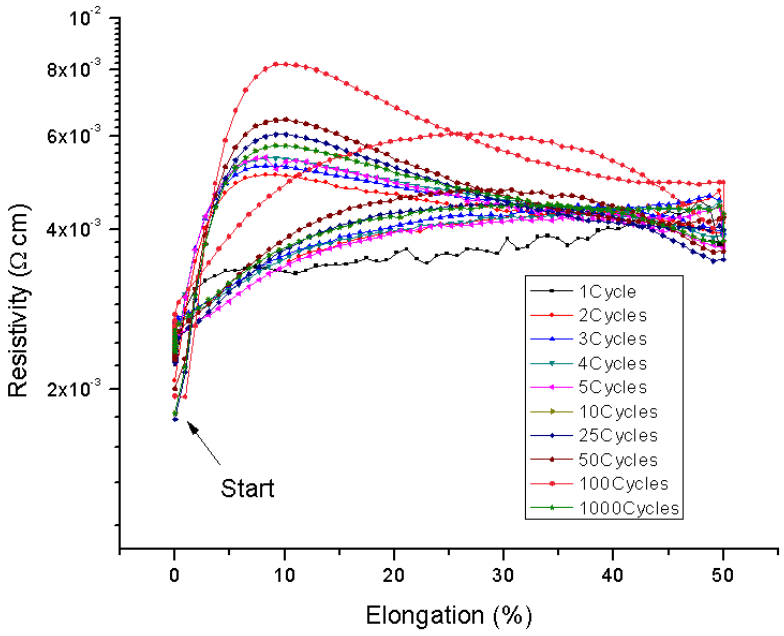

Figure 57. Electrical resistivity during cyclical tensile elongations to 50%.

Following cyclical measurements to 50% elongation, the sample was stretched to 100% and 150% tensile elongation 5000 times in succession. The measured resistivity after stretching to 100% elongation and 150% elongation 5000 times was found to be ~7.67x10^{-4} and ~7.15x10^{-4} Ω-cm respectively. For all electrical-mechanical measurements the strain rate was kept constant at a rate of 10 mm/min. Similar experiments were conducted with S-ECC formulated with AA. Prior to stretching the composite had a resistivity of 1.48x10^{-4} Ω-cm. The higher electrical resistivity found in the AA treated sample was related to the increased difficulty of the transfer process with the addition of AA. After 1000 tensile elongations to 150% the samples resistivity increased to ~3.62x10^{-4} Ω-cm. This improved electrical conductivity following mechanical deformation is likely related to the increased stress distribution and surface roughness of the Ag flakes. Tensile strains to 150% were repeated to 5000 cycles. After 5000 cycles the electrical resistivity increased to ~5.9x10^{-4} Ω-cm. The resistivity of the

AA formulated S-ECC, stretched 5000 times to 150% elongation, showed better performance than the virgin S-ECC, stretched 1000 times to 150%. Thus AA not only increases the electrical conductivity of the S-ECC but also the electro-mechanical response. Increasing the tensile strain to 200% for 5000 times resulted in a significant increase in the electrical resistivity to ~3.99×10^{-3} Ω-cm; however, even after strains of 200% the composite is still conductive enough to be used in many low power or low frequency RF applications.

After mechanically stretching a virgin S-ECC at elongations >200% in multiple directions the samples resistivity increased dramatically to 5×10^{-3} Ω-cm. However, after aging the sample in an 85°C/85% RH accelerated aging environment the resistivity continued to drop. After aging for 72 hours the resistivity of the composite returned to 1.04×10^{-4} Ω-cm. The recover of the electrical properties seen following aging is related to the viscoelastic response of the polymer composite. By increasing the temperature of the composite the recovery time is decreased. Additional aging of the composite, for a week, showed no effect on the electrical conductivity of the composite. The conductivity as a function of 85°C/85% RH aging duration is shown in Figure 58.

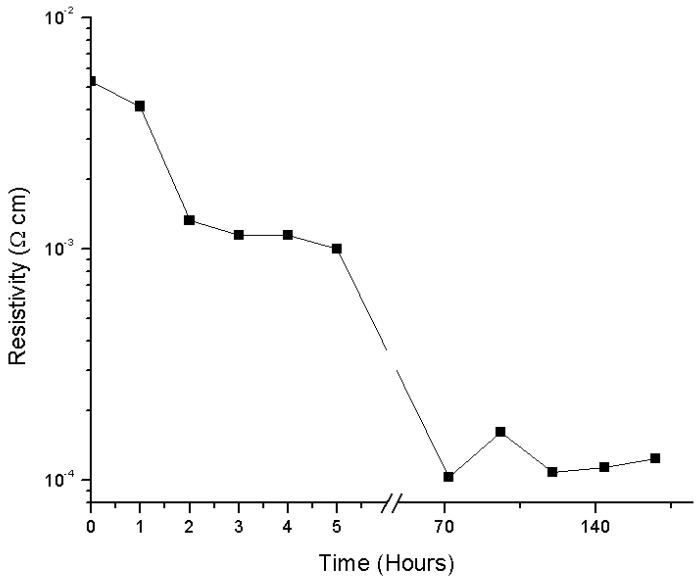

Figure 58. Resistivity of stretchable conductive composite as a function of 85°C/85% RH aging time after mechanical deformation to 150% elongation >5000 times and manually applied biaxial strain to elongations >200%.

We compared the results of our S-ECC to the best results published in recent literature. As shown in Table 11, the S-ECC produced performs better in all performance parameters: conductivity, reliability and tensile performance than any of the S-ECC published in literature. The one aspect where our material has not been quantified yet is printability; however, given the viscosity of the composite formulation and our experience with epoxy based ECC obtaining feature resolution of 250 μm should be easily achievable with high throughput.

Table 11. Comparison of performance of formulated S-ECC to published literature.

SWNT in Ionic liquid [187]	Elongation	Conductivity (S/cm)	Cycles	Sample Dimensions		
				Length	Width	Thickness
	25%	57	4000	N/A	N/Å	200 μm
	38%	57	N/A			
	50%	57	500			
	70%	57	50			
	110%	57	1			
	134%	0.8	1			
	150%	0.1	1			
Ag and SWNT [186]	0%	5710	N/A	10 mm	5 mm	140 μm
	20%	1510	>5000			
	120%	300	N/A			
	140%	20	N/A			
Jet-milled CNT [188]	29%	102	1	N/A	100 μm	50 to 1000 μm
	100%	102	1			
	118%	9.7	1			
	150%	0.1	1			
Unmodified S-ECC*	0%	23,809	N/A	20 mm	6 mm	100 μm
	50%	38,461	>5000			
	100%	1,303	>5000			
	150%	1,398	>5000			
AA modified S-ECC*	0%	6,756	N/A	11 mm	4.5 mm	100 μm
	150%	1,694	>5000			
	200%	250	>5000			

CHAPTER 4

STRETCHABLE RF DEVICES

The possibility of incorporating new functionality by designing flexible and stretchable electronic devices has captured the interest of engineers. Rapidly growing fields like radio frequency identification (RFID), wireless body area networks (WBAN), and medical implantable devices often require robustness, flexibility, stretchability, biocompatibility, comfort, and most importantly, ease of manufacturing and low cost. Moreover, stretchable and flexible antennas provide a means of new attractive applications for radio-frequency devices. Potential applications for stretchable RF devices include: reconfigurable antennas, curvilinear antennas and wearable RF devices [201-204]. Furthermore, the ability to stretch provides antennas with new functionality, including: the ability to tune spectral response and "smart antennas" with beam-forming and bending capabilities useful for security and surveillance systems[202, 203].

To date research on stretchable RF devices is extremely sparse. The only truly stretchable RF devices in publication used microfluidic channels filled with liquid metal (Gallium Indium Eutectic [GaInEu]) as the stretchable conductor. It has been shown that using this approach it is possible to produce stretchable half wave dipole antennas and inverted cone antennas [203-205]. Using liquid metal microfluidics to fabricate stretchable RF devices is "low cost" and highly scalable[1]. However, stretchable liquid metal RF devices have a few practical problems that prohibit their use in consumer

---

[1] Author claims low cost but cost but GaInEu is $4.50/g where Ag is only $1.16/g

electronics. First, indium resources are scarce, thus the already high price of indium is highly influenced by changes in demand. Secondly, GaInEu like other heavy metals is toxic, prohibiting their use in any wearable application. More importantly there are two fundamental materials properties that will prohibit the use of antennas formed with GaInEu. First, GaInEu freezes at 15.5°C, well below -90°C, minimum operational temperature typically required by consumer electronic devices. Secondly, GaInEu CTE is extremely low, on the order of 10^{-4}/°C. This is ~8 orders of magnitude lower than the CTE of PDMS. This extremely large CTE mismatch will cause the microfluidic chamber to explode or implode during thermal cycling. The following sections will discuss fabrication and characterization of a stretchable microstrip line and antenna using S-ECC, which has high impact toughness and a wide range of operational temperatures (-120°C<T<275°C).

4.1 Fundamentals of microstrip lines

A microstrip line is a planar transmission line to transmit microwave frequency signals. Microstip transmission lines consist of a conductive strip and backplane separated by a dielectric. A drawing of a conventional transmission line, indicating the important dimensional parameters and typical circuit diagram is shown in Figure 59A-B respectively.

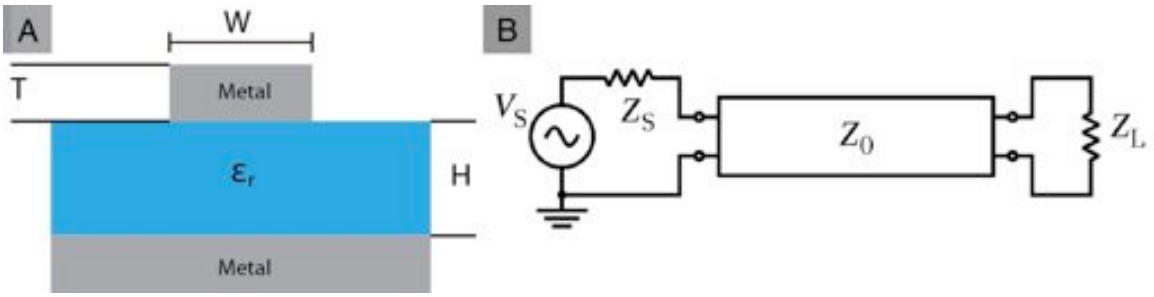

Figure 59. Schematic drawing of a microstrip line.

Typically when a wave travels through a microstrip the fields exist in both the microstrip itself and the air surrounding the microstrip line. Because of this the effective dielectric constant (K_{eff}) is slightly lower than the substrate's dielectric constant. Expressions for the determination of the K_{eff} can be found in Appendix B. Typically transmission lines are described in terms of their characteristic impedance (Z_0). The characteristic impedance is the resistance associated with the transmission of a wave through an infinite, reflection free, lossless transmission line. Because characteristic impedance is a measure of resistance its units are given in Ω, but this has no correlation to the DC electrical resistance of the microstrip line. Models to calculate characteristic impedance tend to be highly complex, typically characteristic impedance is calculated using a simulator.

Since materials used to transmit EM waves cannot transfer signal without loss, the quality of a transmission line is inversely related to the loss during transmission. Imperfect conductors and dielectrics, which give rise to power dissipation, lead to lossy transmission lines. There are two types of loss associated with microstrip lines, transmission loss (attenuation) and mismatch loss (reflection). The mismatch loss is not considered real because it can ideally be tuned out to zero by proper design of the matching network. Typically the propagation of the signal is described in terms of the

propagation constant (γ), which is separated into two components, attenuation (α) and phase (β) as shown in Eq. 25. The real portion α causes the signal amplitude to decrease along the transmission line. Typically the loss is defined in terms of dB/length. The phase constant β determines the sinusoidal amplitude and phase of the signal along the transmission line at a given time. The phase constant is defined as $\beta=2\pi/\lambda$ (degrees/length), where λ is the wavelength. Knowing β, a transmission line of length L will have an electrical phase of βL degrees.

$$\gamma = \alpha + j\beta \tag{25}$$

The amplitude of the wave frozen in time can be described by multiplying the amplitude of the wave in a lossless transmission line $\cos \beta l$ by the attenuation $\exp -\alpha l$. Typically the attenuation constant can be deconvoluted into four components: Loss due to metal conductivity (α_c), loss due to dielectric loss tangent (α_D), loss due to conductivity of dielectric (α_G) and loss due to radiation (α_R), such that the total attenuation can be described as shown in Eq. 26.

$$\alpha = \alpha_c + \alpha_D + \alpha_G + \alpha_R \tag{26}$$

At low frequencies, loss is dominated by the metallic component. Typically metallic loss varies predominantly with $\sqrt{f}$. Metallic loss is complex, comprising more than just the resistivity of the metal. The metallic loss is a function of the resistivity of the metal, sheet resistance and geometry of the transmission line. Typically the metallic loss is defined as the R' component of the series resistance by the transmission line. To determine R' requires that the sheet resistance is known. However, the sheet resistance cannot be simply determined from DC measurements, because of skin effects. The skin effect is a phenomenon where at high frequency only portions of the metallic conductor is

accessible to carry current. Thus, as the frequency increases, the effective cross-sectional area of the conductor decreases. This decrease in the effective cross-sectional area causes the resistance of the metal to increase as a function of frequency as shown in Eq. 27.

$$R_{RFSH} = \left(\frac{\pi f \mu_0 \mu_R}{\sigma}\right)^{1/2} \tag{27}$$

R_{RFSH} is typically given in units of Ω/□, to find R' this needs to be converted to Ω/cm. This conversion is dependent on the geometry. Once the resistance value R' is known, α_c can be determined as shown in Eq. 28.

$$\alpha_c = 8.686 \, \frac{R'}{2Z_0} \, \frac{dB}{meter} \tag{28}$$

The dielectric loss tangent tan δ is proportional to the frequency, thus at high frequencies dielectric loss will cause greater attenuation than conductive loss, which is proportional to the square root of frequency. The dielectric loss is commonly described as shown in Eq. 29.

$$\alpha_D = 8.686 \tan\delta \, \frac{\omega C' Z_0}{2} \, \frac{dB}{meter} \tag{29}$$

The two remaining terms, conductivity of the dielectric and radiation loss, typically are insignificant loss mechanisms and normally can be neglected. This is because most dielectrics used are highly insulating thus there is minimal loss. Similarly, radiation loss, loss generated as heat is relatively small thus typically it can also be neglected.

Because coaxial cables are typically used for signal transmission obtaining the maximum signal depends on the match between the characteristic impedance of the microstrip line and the coaxial cable. A coaxial cable has a characteristic impedance which is defined by the radius of the signal pin as well as the dielectric constant. Based

on the dimensions of the cable the minimum loss, as a function of the characteristic impedance can be determined. For a conventional cable, the minimum loss is typically at an impedance of ~75 Ω. However, it is also desirable to a have high power handling density. The power handling density is also dependent on the characteristic impedance and is typically maximized when the microstrip line has a characteristic impedance of 30 Ω. Because of these two competing factors, 50 Ω characteristic impedance has been chosen as a standard for microstrip design and characterization.

4.2 Fabrication of stretchable microstrip line

Polymethylmethacrylate (PMMA) dissolved in anisole was spin coated onto a bare silicon wafer. 3cm x 1.5 mm x 250 μm (l w h) lines of uncured conductive composite were stencil printed using a flip-up microstencil (Mini Micro Stencil Inc.). The composite used for the ground plane was screen-printed between two pieces of Kapton tape 8 mils thick. The conductive composite (2^{nd} generation) was cured at 170°C for 30 min. Following curing of the conductive composite, uncured degased silicone was poured on top of the Si wafer and was allowed to cure at room temperature for 24 hrs. The thickness of the silicone encapsulation was controlled by weight. The PMMA was dissolved in acetone and the silicone encapsulated conductive composite was removed from the Si wafer using a razor blade. The ground plane was fabricated in a process identical to the microstrip line. The conductive lines were cut using a razor blade and bonded to a stretchable ground plane using a small amount of uncured silicone. After curing for 24 hours, excess silicone was cut using a razor blade and the final microstrip line was obtained. The fabrication process for the microstrip line is shown in Figure 60.

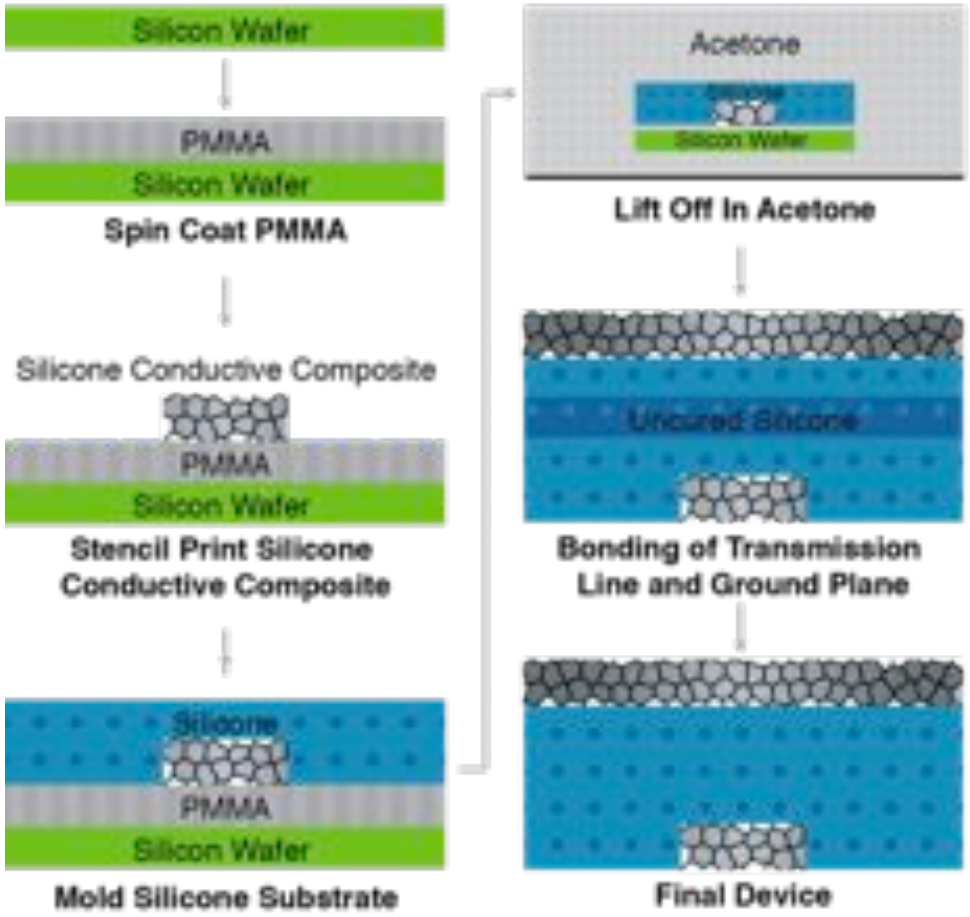

Figure 60. Schematic diagram showing the process to fabricate stretchable microstrip line [196].

The resulting microstrip line is shown in Figure 61, the highly elastomeric nature of the composite material enables tensile strains of 100% to be accommodated without any damage to the device. As shown in Figure 61, the resulting microstrip can be stretched, bent, rolled and twisted. This flexibility in conformation and structure of the microstrip line enables increased function and form factor. For example, the microstrip line can be stretched to change it frequency response, be bent or twisted to change its directionality and/or be integrated into conformably into curvilinear spaces.

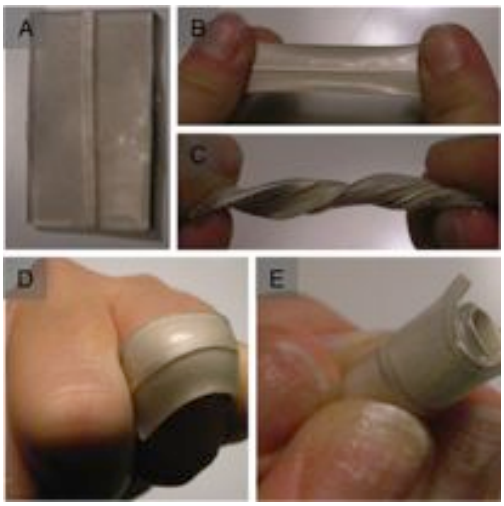

Figure 61. Photographs of microstrip line indicating its ability to flex, stretch and twist [196].

4.3 RF characterization of stretchable microstrip line

The microstrip line S-parameters from 100 MHz to 6 GHz were measured with a E8364B PNA Network Analyzer using a SOLT calibration. Connection to the measurement system was established using 18 GHz SMA connectors. These connectors were chosen because they matched perfectly to the dimension of the microstip line. Perfect match of the connector dimension to the microstrip line is essential since it is impossible to make connections with solder or other conductive adhesives.

The transmission line was measured in three different configurations: straight, bent and twisted. The result in Figure 62, show little to no difference in the measured S-parameters between these three conformations, indicating that the line performance is unaltered by the bending and twisting of the line. The measured insertion loss at 6 GHz was found to be ~0.1 dB/mm. However, full wave measurements in High Frequency Structure Simulator (HFSS) using the extracted DC resistivity of 2x10-4 Ω cm showed a

much lower insertion loss, of about 0.0166 dB/mm at 6 GHz. This discrepancy between the simulated and experimental results can be attributed to two key factors. First, the resistivity is expected to increase with frequency and the simulator only used the measured DC conductivity. The secondly, this discrepancy is due to the poor contact between the SMA connector and the microstrip line. Hence the actual S-parameters of the transmission line is expected to be better than measured and closer to the simulated values. The poor contact resistance is likely due to the small contact area between the signal pin connector and the microstrip signal line. The poor contact between the SMA connectors and the microstrip line was verified using the Keithley 2000 multimeter. The DC resistance of the bare signal line was measured to be 0.2 Ω. Measuring the resistance through the SMA contacts resulted in a total resistance of 5 Ω. This high contact resistance results in parasitic mismatch, translating in increased losses during RF measurement.

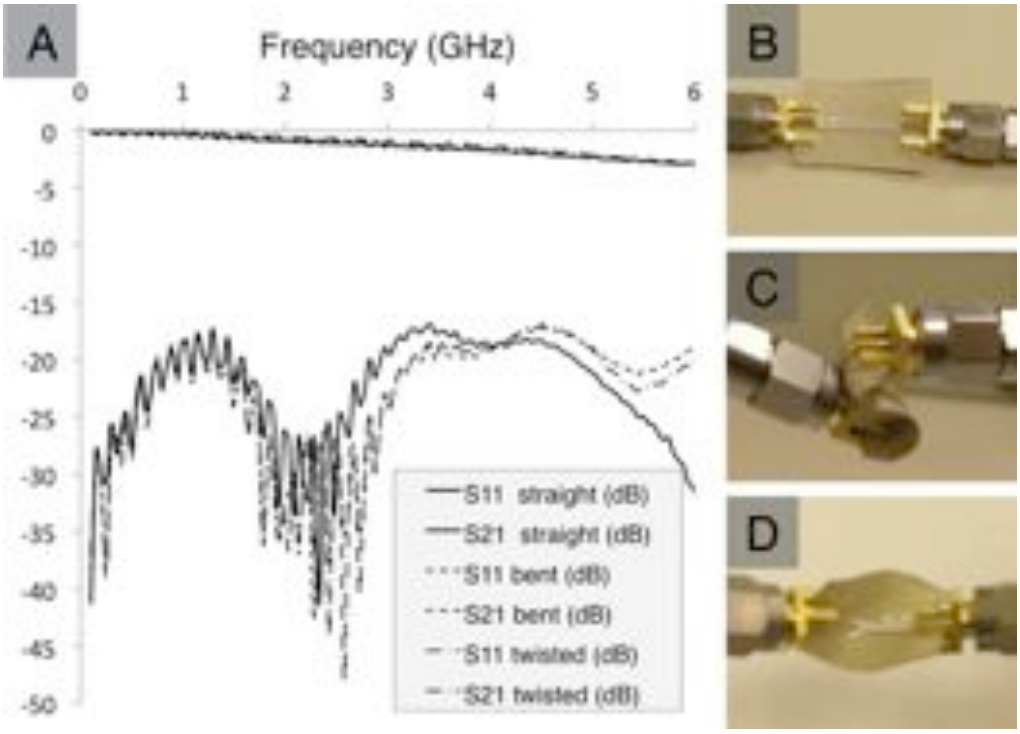

Figure 62. S-parameter measurement results for different line configurations: B. Straight C. Bent D. Twisted [196].

Due to the poor mechanical contact of the connector we were unable to quantify the changes in S-parameters with lengthwise stretching of the line. However, data from the electro-mechanical measurements (Figure 34) promises good and predictable results in the RF regime during tensile elongations.

Following RF testing, cross-sections of the microstrip line was imaged using a 3D confocal microscope (Olympus Corporation). An image of a cross-section is shown in Figure 63. From the dimensions we confirmed that the fabricated microstrip line had a close match to the desired 50 Ω characteristic impedance. Furthermore, from this image the features of the microstrip line are well defined and there is good adhesion between the substrates of the ground plane and microstrip line.

Figure 63. Cross-section of stretchable microstrip line after testing [196].

We are currently in the progress of testing our microstrip line with our 3rd generation materials and expect significantly better results.

4.4 Fabrication of stretchable RF antenna

Creation of an antenna with materials that can bend, stretch and twist provides added functionality, compared to mechanically rigid antennas. The ability to bend, stretch and twist provides the possibility of dynamic reconfiguration, enabling frequency response and directionality to be modulated in dynamic and controllable ways. Bowtie antenna of S-ECC (3rd generation) were screen printed onto Teflon and cured. The antenna was designed to resonate at the Ultra High Frequency (UHF) frequency of 915 MHz. Following curing, the antenna was encapsulated in PDMS and cured. Image of the printed antenna on Teflon and the PDMS packaged stretchable antenna is shown in Figure 64. The antennas S-parameters from 100 MHz to 2 GHz were measured with a E8364B PNA Network Analyzer using a SOLT calibration. Connection to the measurement system was established using 18 GHz SMA connectors. Measurements

were made while the antenna was supported on 4-inch thick foam with a dielectric constant of 1.03.

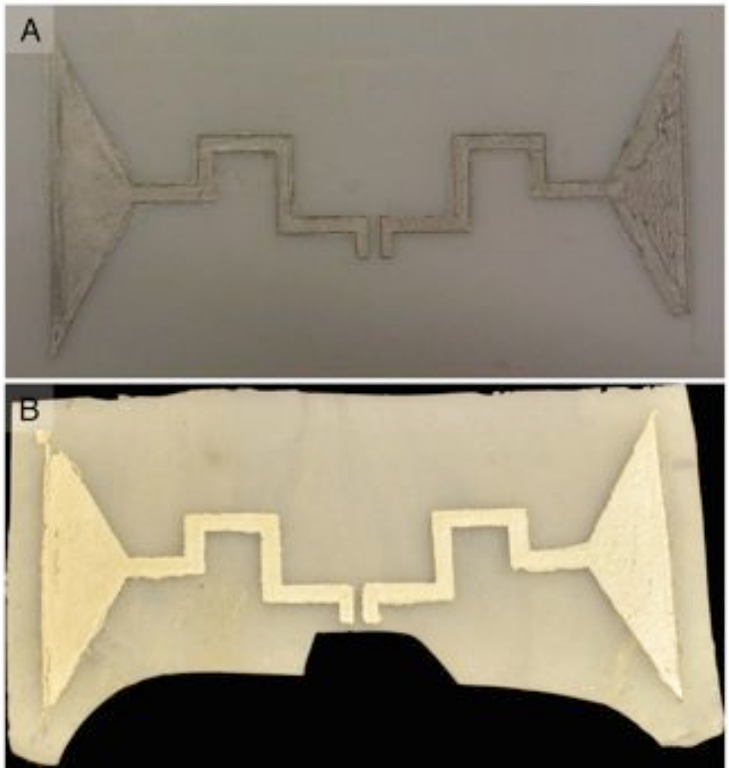

Figure 64. Images showing A. Printed antenna on Teflon B. Stretchable antenna after encapsulation.

The return loss (S_{11}) measurement of the stretchable antenna is shown in Figure 65. From this graph the antenna shows a strong resonance at 895.6 MHz. The observed resonant frequency of 895.6 MHz is slightly lower than the design of 914 MHz, which is partly caused by the increased path length associated with the conductor being a composite not bulk metal. The antenna had a reasonable return loss of about -26.87 dB at the resonant frequency. A return loss of about ~15 dB is sufficient for the antenna to perform properly. Moreover, the antenna showed a 10 dB bandwidth of 12.85%..

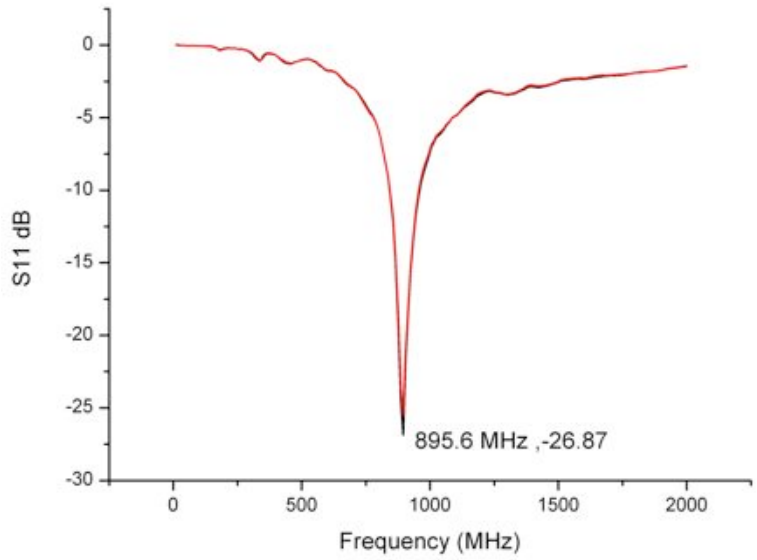

Figure 65. S11 measurements of fabricated unstrained antenna.

We did attempt to measure the antenna under strain however these experiments were difficult. During strain, the resonant frequency tended to downshift to lower resonance frequencies. This would be expected as the path-length of the antenna becomes longer when strained. However, when straining the antenna, the return loss at the resonant frequency decreased dramatically. This change is partly the result of interactions between the sample and the conductive elements used to strain the sample, in our case a person's hand. We are currently designing a fully insulating mechanical stretcher to mechanically modulate the dimensions of the sample without electrical interference. The results of these experiments will be included in a future publication.

CHAPTER 5

SUMMARY, CONCLUSIONS AND FUTURE AREAS OF INTEREST

The diminished returns on investment of research and development focusing on reducing the size of transistors has caused the electronics industry to seek a new approach to enhance the performance of electronic devices. The electronics industry has shifted their focus from reducing the size of the transistor to redesigning the electronic package to increase interconnectivity, parallel processing capabilities and form factor. A second area of emphasis of the electronics packaging industry has focused on changing the way electronics interact with their surroundings. Research has focused on redesigning the electronic package so that electronic devices can directly interact with their environment rather than through peripheral devices. However, to achieve new modes of interface requires that the electronic devices have new ways to sense and respond to their environment and interfaces. In this thesis, we developed a new electrically conductive material which is mechanically compliant. This stretchable electrically conductive material can serve as a flexible and stretchable platform for electronic and radio frequency devices, enabling electronic devices to have coupled mechanical and electrical response.

5.1 Summary of results

In Chapter 2 of this thesis, we show through proof of concept type experiments that the conductivity of ECC is governed by the secondary charge transport (tunneling and hopping), rather than through constriction resistance associated with poor contact

between conductive fillers. This information provides a new perspective on how to approach improving the conductivity of ECC.

In Chapter 3, we show three generations of silicone based S-ECC, each with increasing performance. Throughout these generations of materials we learned the importance of crosslinking density, curing temperature and adhesion to encapsulating PDMS substrate. Furthermore, we show how the addition of AA can be used to reduce Ag salt formed between the surfactants and the surface of the Ag flakes. The ability of AA to reduce Ag salt on the surface of Ag flakes caused the formation and sintering of nanoparticles, dramatically increasing conductivity of the S-ECC. Using the insight gained from the development of the first two generations of S-ECC, we developed a S-ECC with unprecedented electro-mechanical performance and reliability. The S-ECC developed can withstand >5,000 cyclical tensile strains to 50% elongation while maintaining a high conductivity of 38,461 S/cm. Finally in this section we show how this material could be processed to produce stretchable 3D interconnected structures without the need for any cleanroom or vacuum processes.

In Chapter 4, we utilize the S-ECC developed in Chapter 3 to fabricate stretchable RF devices. We show that our materials and processes can easily be adapted to produce stretchable microstip line and antennas. Characterization of our stretchable microstrip line showed good performance up to 6 GHz, with a low insertion loss of 0.1 dB/mm. Furthermore, it was found that our microstrip line performance was stable during bending and twisting. Fabrication of an antenna designed to resonate at 915 MHz had a strong resonance of 26.87 dB with a large bandwidth of 12.85%. However, this antenna resonated at a slightly lower frequency of 895.6 MHz due partially to the increased path-

length associated with the longer conduction pathway in composites compared to bulk metals.

5.2 Future work

5.2.1 Understanding of the conduction mechanism in ECC

To gain further insight to the conduction mechanism in ECC there are many future experiments which could provide fruitful results. First, since each mechanism of charge transport has a distinguishable frequency response, high frequency conductivity measurements could provide a useful method of deducing the predominate mechanism of secondary charge transport. Similarly, the mechanism and rate of transport could be experimentally simulated by measuring tunneling current through a thin polymer interface, as a Ag flake modified conductive AFM tip approaches a surface under potential.

5.2.2 Stretchable conductive composites

The unprecedented performance of our S-ECC enables many new applications impossible with previous materials. For each of these individual applications the formulation will have to be optimized to obtain the desired electro-mechanical response. The remainder of this section will talk about some of the novel applications/areas of interest for this material.

Ultra-low stress large area interconnects

The electronics packaging industry has been working on maximizing die size and interconnect density, but have been limited by the large internal stresses generated by the CTE mismatch between the IC and the organic substrate. Decades worth of research has focused on minimizing these internal stresses. The uses of stretchable interconnect and underfill materials will decouple the IC from the organic substrate eliminating the stresses associated with the CTE mismatch. However, currently the S-ECC has extremely poor adhesion. Future formulations of S-ECC need to be developed to optimize stretchability and adhesion. This could easily be accomplished by selectively functionalizing the PDMS with epoxide groups. One simple method to achieve epoxy functionality on PDMS resins is to react allyl glycidyl ether with hydride terminated silicone in the presence of platinum.

Furthermore, it is desirable to surface mount active component and interconnect them with the stretchable flexible package. However, if the S-ECC was to strain underneath the surface mounted component it would likely cause failure at the interface. To minimize strain beneath the surface mounted device, short chain hydride terminated silicone could be inkjet printed in areas where devices are going to be connected. Inclusion of addition short chain hydride-terminated silicone will increase the modulus locally, minimizing strain in that region.

Inkjettable stretchable electrically conductive composite

To reduce cost, increase resolution and throughput it is desirable to inkjet print S-ECC. However, the filler size is currently too large to be printed through a nozzle.

Replacement of the large Ag flakes with Ag nanowires could enable inkjet printing of the S-ECC.

Ultra low cost stretchable electrically conductive composite

The cost of Ag is too high for use in low cost consumer electronic devices. For example, a back of the hand calculation to determine the cost of materials and fabrication of the stretchable antenna we fabricated estimated its cost to be ~$3 per antenna. However, the desired cost benchmark for mass market RFID is <5 cents per tag. One method to reduce the cost of the antenna is to reduce the cost of the materials. By replacing the Ag flakes with Ag coated copper flakes the cost to fabricate S-ECC devices can be reduced significantly. However, if Ag coated copper is to be used more work needs to be done to improve the passivation of the flakes, preventing the oxidation of the copper.

5.3 Stretchable radio frequency devices

Since there have been extremely few publications on composites materials for antennas or stretchable antennas many fundamental experiments need to be conducted. First, because composites have complex conduction mechanisms and structures compared to bulk metals, studies focusing on the propagation of EM waves through ECC is needed. It is conceivable that the wave propagation through the composite will depend strongly on the size, order, surface chemistry, and interconnectivity of the conductive fillers; as well as the dielectric properties of the polymer matrix. The material response should also have an atypical frequency dependence depending on all of the aforementioned parameters.

Similarly, there have been very few publications focusing on the RF properties of stretchable RF devices during mechanical deformation. Future work focusing on creative architectures should enable unique and controlled frequency response and directivity during mechanical deformation. Future work should emphasize how mechanical deformation of stretchable RF devices can be used to create reconfigurable and directional RF devices simplistically.

5.4 Concluding remarks

Composite materials, because of their ability to achieve tunable material properties impossible with a single material, will become increasingly important in electronic packaging. We utilize these unique attributes of composite materials to make highly conductive stretchable conductors. The unprecedented performance achieved with our material enables new applications impossible prior. We showed how using these materials we can fabricate stretchable RF devices simply with extremely good performance. However, the work presented here is just the proof of concept. The material developed has a plethora of applications currently unexplored. Future developments of this material and processes will enable the fabrication of a wide variety of stretchable electronic, radio frequency and sensory devices currently impossible with current materials and processes.

APPENDIX A

MEASUREMENT OF BULK RESISTIVITY

Bulk resistivity was determined by initially measuring the bulk resistance using a Keithley 2000 (Keithley Instruments Inc.) multimeter, four wire method. The four wire method eliminated any contact resistance by measuring the voltage across a region where current is applied. Since no current flows through the contacts used to measure the voltage, there is no resistance associated with these contacts. The width and length of the specimen was measured using a digital caliper (VWR). The thickness of the sample was measured by Heidenhain (thickness measuring equipment, ND 281B, Germany). The bulk resistivity was calculated using Equation 1 where l, w and t is the length, width and thickness respectively:

$$\rho = \frac{t \times w}{l} \times R \tag{30}$$

APPENDIX B

DETERMINATION OF EFFECTIVE DIELECTRIC CONSTANT FOR A MICROSTRIP TRANSMISSION LINE

Based on the equation proposed by Hamerstad and Jensen, the effective dielectric constant can be described as shown in Eq. 31. It has been found that this model is better than 0.2% accurate when ε_r<128 and 0.01≤W/h≤100.

$$\varepsilon_{eff}(W, h, \varepsilon_r) = \frac{\varepsilon_r + 1}{2} + \frac{\varepsilon_r - 1}{2}\left(1 + 10\frac{h}{W}\right)^{-ab} \tag{31}$$

Where: $v = W/h$

$$a(v) = 1 + \frac{1}{49}\ln\left(\frac{v^4 + (v/52)^2}{v^4 + 0.432}\right) + \frac{1}{18.7}\ln\left(1 + \left(\frac{v}{18.1}\right)^3\right) \quad (32)$$

$$b(\varepsilon_r) = 0.564\left(\frac{\varepsilon_r - 0.9}{\varepsilon_r + 3}\right)^{0.053} \quad (33)$$

However, this equation fails when there is a non-zero strip thickness, to adjust for this a correction factor must be used.

$$\Delta W_1 = \frac{t}{h\pi}\ln\left(1 + \frac{4e}{\frac{t}{h}\coth^2\sqrt{6.517W}}\right) \quad (34)$$

$$\Delta W_r = \frac{1}{2}\Delta W_1\left(1 + \operatorname{sech}\sqrt{\varepsilon_r - 1}\right) \quad (35)$$

REFERENCES

[1] (2011, 4/05/2011). *Microprocessor Quick Reference Guide*. Available: http://www.intel.com/pressroom/kits/quickreffam.htm - xeon

[2] G. E. Moore, "Cramming more components onto integrated circuits," *Electronics,* vol. 38, April 19, 1965 1965.

[3] V. V. C. Zhirnov, R.K., III; Hutchby, J.A.; Bourianoff, G.I.; , "Limits to binary logic switch scaling - a gedanken model," *Proceedings of the IEEE* vol. 91, pp. 1934-1939, November 8, 2003 2003.

[4] R. R. Tummala, E. J. Rymaszewski, and A. G. Klopfenstein, "Microelectronics Packaging Handbook," *Springer,* p. 1027, 1997.

[5] I. C. Kang and L. Kwang-Lung, "Effects of gallium on wettability, microstructures and mechanical properties of the Sn-Zn-Ag-Ga and Sn-Zn-Ag-Al-Ga solder alloys," in *Electronic Materials and Packaging, 2002. Proceedings of the 4th International Symposium on*, 2002, pp. 49-54.

[6] H. Dong, Y. Li, M. J. Yim, K. S. Moon, and C. P. Wong, "Investigation of electrical contact resistance for nonconductive film functionalized with p-conjugated self-assembled molecules," *Applied Physics Letters,* vol. 90, pp. 092102/1-092102/3, 2007.

[7] Y. Li and C. P. Wong, "Recent advances of conductive adhesives as a lead-free alternative in electronic packaging: materials, processing, reliability and applications," *Materials Science & Engineering, R: Reports,* vol. R51, pp. 1-35, 2006.

[8] K. Gilleo, "Assembly with conductive adhesives," *Soldering & Surface Mount Technology,* vol. 19, pp. 12-17, 1995.

[9] P. G. Harris, "Conductive adhesives: A critical review of progress to date," *Soldering & Surface Mount Technology,* vol. 20, pp. 19-21, 26, 1995.

[10] Y. Myung Jin, L. Yi, M. Kyoung-sik, P. Kyung Wook, and C. P. Wong, "Review of Recent Advances in Electrically Conductive Adhesive Materials and

Technologies in Electronic Packaging," *Journal of Adhesion Science & Technology,* vol. 22, pp. 1593-1630, 2008.

[11] J. C. Agar, K. J. Lin, R. W. Zhang, J. Durden, K. Lawrence, K.-S. Moon, and C. P. Wong, "Deconstructing the Myth of Percolation in Electrically Conductive Adhesives and its Implication," presented at the ECTC, Las Vegas, 2010.

[12] Z. Rongwei, M. Kyoung-sik, L. Wei, and C. P. Wong, "Electrical properties of ACA joints assisted by conjugated molecular wires," in *Electronic Components and Technology Conference, 2009. ECTC 2009. 59th*, 2009, pp. 2034-2038.

[13] M. Chen, L.-Y. Wang, J.-T. Han, J.-Y. Zhang, Z.-Y. Li, and D.-J. Qian, "Preparation and Study of Polyacryamide-Stabilized Silver Nanoparticles through a One-Pot Process," *Journal of Physical Chemistry B,* vol. 110, pp. 11224-11231, 2006.

[14] D. Lu, S. Luo, and C. P. Wong, *Encyclopedia of Polymer Science and Technology, Second Ed., John Wiley & Sons, Inc., New York, .* vol. 5, 2002.

[15] J. S. Hwang, *Environmental-friendly electronics: lead-free technology,* vol. Electrochemical publications Ltd, 2001.

[16] D. L. Kleyer, M. A. Lutz, K. Mine, O. Mitani, K. Nakayoshi, and B. Vanwert, "Electrically conductive silicone compositions," ed: Google Patents, 2000.

[17] J. M. P. Pujol, J. B. Hall, P. B. Hogerton, F. B. McCormick, and J. M. Tingerthal, "Cyanate ester adhesives for electronic applications," ed: Google Patents, 1992.

[18] H. Fenghong, W. Zhanpeng, L. Wu, W. Dezhen, and J. Riguang, "Preparation and performance of natural graphite-silver nanoparticles/polyurethane conductive composites," *Acta Materiae Compositae Sinica,* p. 04, 2007.

[19] J. J. Licari and D. W. Swanson, "Adhesives technology for electronic applications: materials, processes, reliability," *William Andrew, Norwich, NY, USA,* 2005.

[20] S. i. Asai, U. Saruta, M. Tobita, M. Takano, and Y. Miyashita, "Development of an anisotropic conductive adhesive film (ACAF) from epoxy resins," *Journal of Applied Polymer Science,* vol. 56, pp. 769-77, 1995.

[21] D. D. Chang, P. A. Crawford, J. A. Fulton, R. McBride, M. B. Schmidt, R. E. Sinitski, and C. P. Wong, "An overview and evaluation of anisotropically conductive adhesive films for fine pitch electronic assembly," *IEEE Transactions on Components, Hybrids, and Manufacturing Technology,* vol. 16, pp. 828-35, 1993.

[22] J. Rocks, M. Halter, G. George, and F. Vohwinkel, "Calorimetric and rheological characterization of a high-performance epoxy curable at low temperatures," *Polym. Int.,* vol. 52, pp. 1749-1757, 2003.

[23] J. Leukel, W. Burchard, R.-P. Krueger, H. Much, and G. Schulz, "Mechanism of the anionic copolymerization of anhydride-cured epoxies analyzed by matrix-assisted laser desorption ionization time-of-flight mass spectrometry (MALDI-TOF-MS)," *Macromolecular Rapid Communications,* vol. 17, pp. 359-366, 1996.

[24] W. Fisch and W. Hofmann, "The hardening mechanism of epoxy resins," *J. Polym. Sci.,* vol. 12, pp. 497-502, 1954.

[25] W. Fisch, W. Hofmann, and J. Koskikallio, "Curing mechanism of epoxy resins," *J. Appl. Chem. (London),* vol. 6, pp. 429-41, 1956.

[26] J. Rocks, G. A. George, and F. Vohwinkel, "Curing kinetics and thermomechanical behaviour of co-anhydride cured aminoglycidyl epoxy resins," *Polym. Int.,* vol. 52, pp. 1758-1766, 2003.

[27] J. Rocks, L. Rintoul, F. Vohwinkel, and G. George, "The kinetics and mechanism of cure of an amino-glycidyl epoxy resin by a co-anhydride as studied by FT-Raman spectroscopy," *Polymer,* vol. 45, pp. 6799-6811, 2004.

[28] H. Teil, S. A. Page, V. Michaud, and J. A. E. Manson, "TTT-cure diagram of an anhydride-cured epoxy system including gelation, vitrification, curing kinetics model, and monitoring of the glass transition temperature," *J. Appl. Polym. Sci.,* vol. 93, pp. 1774-1787, 2004.

[29] H. Zweifel and T. Voelker, "Mechanism of anionic polymerization of maleic anhydride. 2," *Makromol. Chem.,* vol. 170, pp. 141-53, 1973.

[30] G. C. Stevens and M. J. Richardson, "Factors influencing the glass transition of DGEBA-anhydride epoxy resins," *Polymer,* vol. 24, pp. 851-858, 1983.

[31] K. M. Choi and J. A. Rogers, "A Photocurable Poly(dimethylsiloxane) Chemistry Designed for Soft Lithographic Molding and Printing in the Nanometer Regime," *Journal of the American Chemical Society,* vol. 125, pp. 4060-4061, 2003.

[32] "Product Information sheet Sylgard 184," in *Dow Corning*, ed, 2010.

[33] B. J. Basu, A. Thirumurugan, A. R. Dinesh, C. Anandan, and K. S. Rajam, "Optical oxygen sensor coating based on the fluorescence quenching of a new pyrene derivative," *Sensors and Actuators B: Chemical,* vol. 104, pp. 15-22, 2005.

[34] S. J. Clarson and J. A. Semlyen, *Siloxane polymers*: Prentice Hall, 1993.

[35] A. Colas and J. Cutis, *Biomaterials Science: An introduction to Materials in Medicine*: Elsevier, 1996.

[36] A. K. Bhowmick and H. L. Stevens, *Handbook of elastomers* vol. Second Edition. New York: Marcel Dekker, Inc., 2001.

[37] E. L. Warrick and P. C. Lauterbur, "Filler Phenomena in Silicone Rubber," *Industrial & Engineering Chemistry,* vol. 47, pp. 486-491, 1955.

[38] N. R. Langley and K. E. Polmanteer, "Relation of elastic modulus to crosslink and entanglement concentrations in rubber networks," *Journal of Polymer Science: Polymer Physics Edition,* vol. 12, pp. 1023-1034, 1974.

[39] K. E. Polmanteer, "Siloxane Elastomers," USA Patent 2927907, 1960.

[40] J.-B. Donnet and E. Custodero, "Reinforcement of Elastomers by Particulate Fillers," in *Science and Technology of Rubber (Third Edition)*, E. M. James, E. Burak, and R. E. Frederick, Eds., ed Burlington: Academic Press, 2005, pp. 367-400.

[41] M. Morton, "Mechanisms of Reinforcement of Elastomers by Polymeric Fillers," in *Multicomponent Polymer Systems*. vol. 99, ed: AMERICAN CHEMICAL SOCIETY, 1971, pp. 490-509.

[42] G. Berrod, A. Vidal, E. Papirer, and J. B. Donnet, "Reinforcement of siloxane elastomers by silica. Chemical interactions between an oligomer of poly(dimethylsiloxane) and a fumed silica," *Journal of Applied Polymer Science,* vol. 26, pp. 833-845, 1981.

[43] M. Zaborski, A. Vidal, G. Ligner, H. Balard, E. Papirer, and A. Burneau, "Comparative study of the surface hydroxyl groups of fumed and precipitated silicas. I. Grafting and chemical characterization," *Langmuir,* vol. 5, pp. 447-451, 1989.

[44] A. Burneau, O. Barres, J. P. Gallas, and J. C. Lavalley, "Comparative study of the surface hydroxyl groups of fumed and precipitated silicas. 2. Characterization by infrared spectroscopy of the interactions with water," *Langmuir,* vol. 6, pp. 1364-1372, 1990.

[45] P. Jerschow, "Silicone Elastomers," *Rapra Review Reports,* vol. 12, 2001.

[46] L. N. Lewis, J. Stein, Y. Gao, R. E. Colborn, and G. Hutchins, "Platinum Catalysts Used in the Silicones Industry: Their Synthesis and Use in Hydrosilylation," *Platinum Metal Reviews,* vol. 41, pp. 66-75, 1997.

[47] A. J. Chalk and J. F. Harrod, "Homogeneous Catalysis. II. The Mechanism of the Hydrosilation of Olefins Catalyzed by Group VIII Metal Complexes1," *Journal of the American Chemical Society,* vol. 87, pp. 16-21, 1965.

[48] S. Sakaki, N. Mizoe, M. Sugimoto, and Y. Musashi, "Pt-catalyzed hydrosilylation of ethylene. A theoretical study of the reaction mechanism," *Coordination Chemistry Reviews,* vol. 190-192, pp. 933-960, 1999.

[49] L. Daoqiang, Q. K. Tong, and C. P. Wong, "Conductivity mechanisms of isotropic conductive adhesives (ICAs)," *Electronics Packaging Manufacturing, IEEE Transactions on,* vol. 22, pp. 223-227, 1999.

[50] S. W. Lee and S. S. Lee, "Shrinkage ratio of PDMS and its alignment method for the wafer level process," *Microsyst. Technol.,* vol. 14, pp. 205-208, 2007.

[51] J. Liu, "Conductive adhesives for electronics packaging," *UK: Electrochemical Publications Ltd,* 1999.

[52] M. J. Yim, Y. Li, K. S. Moon, and C. P. Wong, "Oxidation prevention and electrical property enhancement of copper-filled isotropically conductive adhesives," *Journal of Electronic Materials,* vol. 36, pp. 1341-1347, 2007.

[53] Y.-S. Lin and S.-S. Chiu, "Electrical properties of copper-filled electrically conductive adhesives and pressure-dependent conduction behavior of copper particles," *Journal of Adhesion Science and Technology,* vol. 22, pp. 1673-1697, 2008.

[54] Y.-S. Lin and S.-S. Chiu, "Effects of oxidation and particle shape on critical volume fractions of silver-coated copper powders in conductive adhesives for microelectronic applications," *Polymer Engineering and Science,* vol. 44, pp. 2075-2082, 2004.

[55] S.-Y. Park, T.-W. Yoon, C.-H. Lee, I.-B. Jeong, and S.-H. Hyun, "Surface modification of Ag coated Cu conductive metal powder for conductive silicone sealant gasket paste," *Materials Science Forum,* vol. 534-536, pp. 933-936, 2007.

[56] J.-C. Huang, "Carbon black filled conducting polymers and polymer blends," *Advances in Polymer Technology,* vol. 21, pp. 299-313, 2002.

[57] R. Zhang and F. Liu, "Advances in Carbon Black-Polymer Composites," *Polymer Materials Science & Engineering,* vol. 21, pp. 45-49, 2005.

[58] S. Stankovich, D. A. Dikin, G. H. B. Dommett, K. M. Kohlhaas, E. J. Zimney, E. A. Stach, R. D. Piner, S. T. Nguyen, and R. S. Ruoff, "Graphene-based composite materials," *Nature (London, United Kingdom),* vol. 442, pp. 282-286, 2006.

[59] X. Wang, L. Zhi, and K. Muellen, "Transparent, Conductive Graphene Electrodes for Dye-Sensitized Solar Cells," *Nano Letters,* vol. 8, pp. 323-327, 2008.

[60] Y. Kim, S. Y. Cho, Y. S. Yun, and H.-J. Jin, "Electroconductive adhesives based on polyurethane wtih multiwalled carbon nanotubes," *Modern Physics Letters B,* vol. 23, pp. 3739-3745, 2009.

[61] M. Heimann, M. Wirts-Ruetters, B. Boehme, and K.-J. Wolter, "Investigation of carbon nanotubes epoxy composites for electronics packaging," *IEEE Electronic Components and Technology Conference,* vol. 58th, pp. 1731-1736, 2008.

[62] X. Yu, R. Rajamani, K. A. Stelson, and T. Cui, "Carbon nanotube based transparent conductive thin films," *Journal of Nanoscience and Nanotechnology,* vol. 6, pp. 1939-1944, 2006.

[63] M. Moniruzzaman and K. I. Winey, "Polymer Nanocomposites Containing Carbon Nanotubes," *Macromolecules,* vol. 39, pp. 5194-5205, 2006.

[64] Y. Oh, D. Suh, Y. Kim, E. Lee, J. S. Mok, J. Choi, and S. Baik, "Silver-plated carbon nanotubes for silver/conducting polymer composites," *Nanotechnology,* vol. 19, pp. 495602/1-495602/7, 2008.

[65] H. P. Wu, X. J. Wu, M. Y. Ge, G. Q. Zhang, Y. W. Wang, and J. Jiang, "Properties investigation on isotropical conductive adhesives filled with silver coated carbon nanotubes," *Composites Science and Technology,* vol. 67, pp. 1182-1186, 2007.

[66] J. Jang and S. K. Ryu, "Physical property and electrical conductivity of electroless Ag-plated carbon fiber-reinforced paper," *Journal of Materials Processing Technology,* vol. 180, pp. 66-73, 2006.

[67] M. You, L. Zhang, Z. Gong, W. Liu, and A. He, "On the properties of conductive adhesive filled with electroless silver plated flake graphite," *Key Engineering Materials,* vol. 373-374, pp. 220-223, 2008.

[68] W. Lin, X. Xi, and C. Yu, "Research of silver plating nano-graphite filled conductive adhesive," *Synthetic Metals,* vol. 159, pp. 619-624, 2009.

[69] T. Liang, W. Guo, Y. Yan, and C. Tang, "Electroless plating of silver on graphite powders and the study of its conductive adhesive," *International Journal of Adhesion and Adhesives,* vol. 28, pp. 55-58, 2007.

[70] G. Lu, X. Li, and H. Jiang, "Electrical and shielding properties of ABS resin filled with nickel-coated carbon fibers," *Composites Science and Technology,* vol. 56, pp. 193-200, 1996.

[71] H. Zou, L. Zhang, M. Tian, S. Wu, and S. Zhao, "Study on the structure and properties of conductive silicone rubber filled with nickel-coated graphite," *Journal of Applied Polymer Science,* vol. 115, pp. 2710-2717, 2010.

[72] S. K. Kang, R. S. Rai, and S. Purushothaman, "Development of high conductivity lead (Pb)-free conducting adhesives," *IEEE Transactions on Components, Packaging, and Manufacturing Technology, Part A,* vol. 21, pp. 18-22, 1998.

[73] S. K. Kang and S. Purushothaman, "Development of conducting adhesive materials for microelectronic applications," *Journal of Electronic Materials,* vol. 28, pp. 1314-1318, 1999.

[74] D. Lu and C. P. Wong, "Isotropic conductive adhesives filled with low-melting-point alloy fillers," *IEEE Transactions on Electronics Packaging Manufacturing,* vol. 23, pp. 185-190, 2000.

[75] C. Gallagher, G. Matijasevic, and J. F. Maguire, "Transient liquid phase sintering conductive adhesives as solder replacements," *Proceedings - Electronic Components & Technology Conference,* vol. 47th, pp. 554-560, 1997.

[76] C. Gallagher, G. Matijasevic, and M. A. Capote, "Transient liquid phase sintering conductive adhesives for mechanical, electrical and thermal interconnects," Application: US
US Patent 96-704467
5853622, 1998.

[77] C. Shearer, B. Shearer, G. Matijasevic, and P. Gandhi, "Transient liquid-phase sintering composites: polymer adhesives with metallurgical bonds," *Journal of Electronic Materials,* vol. 28, pp. 1319-1326, 1999.

[78] J.-M. Kim, K. Yasuda, and K. Fujimoto, "Isotropic conductive adhesives with fusible filler particles," *Journal of Electronic Materials,* vol. 33, pp. 1331-1337, 2004.

[79] R. Zhang, K.-s. Moon, W. Lin, J. C. Agar, and C.-P. Wong, "A simple, low-cost approach to prepare flexible highly conductive polymer composites by in situ reduction of silver carboxylate for flexible electronic applications," *Composites Science and Technology,* vol. 71, pp. 528-534, 2011.

[80] S. M. Pandiri, "The behavior of silver flakes conductive epoxy adhesives," *Adhesives Age,* pp. 31-35, 1987.

[81] D. Lu and C. P. Wong, "Thermal decomposition of silver flake lubricants," *Journal of Thermal Analysis and Calorimetry,* vol. 61, pp. 3-12, 2000.

[82] D. Lu and C. P. Wong, "Characterization of silver flake lubricants," *Journal of Thermal Analysis and Calorimetry,* vol. 59, pp. 729-740, 2000.

[83] R. Zhang, J. C. Agar, and C. P. Wong, "Conductive Polymer Composites," in *Encyclopedia of Polymer Science and Technology*, ed: John Wiley & Sons, Inc., 2002.

[84] H. Dong, L. Fan, K.-s. Moon, C. P. Wong, and M. I. Baskes, "Molecular dynamics simulation of lead free solder for low temperature reflow applications," *Proceedings - Electronic Components & Technology Conference,* vol. 55th, pp. 983-987, 2005.

[85] S. Magdassi, M. Grouchko, O. Berezin, and A. Kamyshny, "Triggering the Sintering of Silver Nanoparticles at Room Temperature," *ACS Nano,* vol. 4, pp. 1943-1948, 2010.

[86] J. Kolbe, A. Arp, F. Calderone, E. M. Meyer, W. Meyer, H. Schaefer, and M. Stuve, "Inkjettable conductive adhesive for use in microelectronics and microsystems technology," *Microelectronics Reliability,* vol. 47, pp. 331-334.

[87] G. R. Palmese and J. K. Gillham, "Time-temperature-transformation (TTT) cure diagrams: relationship between Tg and the temperature and time of cure for a polyamic acid/polyimide system," *J. Appl. Polym. Sci.,* vol. 34, pp. 1925-39, 1987.

[88] M. J. Yim, Y. Li, K.-s. Moon, K. W. Paik, and C. P. Wong, "Review of Recent Advances in Electrically Conductive Adhesive Materials and Technologies in Electronic Packaging," *Journal of Adhesion Science and Technology,* vol. 22, pp. 1593-1630, 2008.

[89] G. Yi Li and C. P. Wong, "Nano-Ag Filled Anisotropic Conductive Adhesives (ACA) with Self-Assembled Monolayer and Sintering Behavior for High," in *Electronic Components and Technology Conference, 2005. Proceedings. 55th*, 2005, pp. 1147-1154.

[90] Y. Myung-Jin and P. Kyung-Wook, "Design and Understanding of Anisotropic Conductive Films(ACF's) for LCD Packaging," *IEEE Transactions on Components,* vol. 21, pp. 226-234, Jan 1 1998.

[91] Y. Li, M. Yim, and C. P. Wong, "High Performance Nonconductive Film with -Conjugated Self-Assembled Molecular Wires for Fine Pitch Interconnect Applications," *Journal of Electronic Materials,* vol. 36, pp. 549-554, 2007.

[92] G. R. Ruschau, S. Yoshikawa, and R. E. Newnham, "Resistivities of conductive composites," *Journal of Applied Physics,* vol. 72, pp. 953-9, 1992.

[93] R. Holm, "Electric Contacts, Theory and Application," 1967.

[94] R. Zhang, K. S. Moon, W. Lin, and C. P. Wong, "Electrical properties of ACA joints assisted by conjugated molecular wires," *IEEE Electron. Compon. Technol. Conf.,* vol. 59th, pp. 2034-2038, 2009.

[95] I. A. Chmutin, S. V. Letyagin, V. G. Shevchenko, and A. T. Ponamorcnko, "Conductive Polymer Composites: Structure, Contact Phenomena, and Anisotropy," *Vysokomol. Soedin. Ser. A,* vol. 36, 1994.

[96] V. I. Roldughin and V. V. Vysotskii, "Percolation properties of metal-filled polymer films, structure and mechanisms of conductivity," *Progress in Organic Coatings,* vol. 39, pp. 81-100, 2000.

[97] C. Li, E. T. Thostenson, and T.-W. Chou, "Dominant role of tunneling resistance in the electrical conductivity of carbon nanotube-based composites," *Appl. Phys. Lett.,* vol. 91, pp. 223114/1-223114/3, 2007.

[98] J. G. Simmons, "Generalized Formula for the Electric Tunnel Effect between Similar Electrodes Separated by a Thin Insulating Film," *Journal of Applied Physics,* vol. 34, pp. 1793 - 1803, 1963.

[99] R. Holm, *Electrical Contacts, Theory and Applications*. New York: Springer, 1967.

[100] R. Holm and B. Kirschstein, "Bemerkungen zu einer Arbeit von O. Mayr über die „Berechnung der elektrischen Durchbruchfeldstärke von Gasen mit Hilfe des Nernstschen Wärmetheorems “," *Electrical Engineering (Archiv fur Elektrotechnik),* Jan 1 1932.

[101] R. L. Jackson and L. Kogut, "Electrical Contact Resistance Theory for Anisotropic Conductive Films Considering Electron Tunneling and Particle

Flattening," *Components and Packaging Technologies, IEEE Transactions on,* vol. 30, pp. 59-66, 2007.

[102] Y. Myung-Jin and P. Kyung-Wook, "Design and understanding of anisotropic conductive films (ACF's) for LCD packaging," *Components, Packaging, and Manufacturing Technology, Part A, IEEE Transactions on,* vol. 21, pp. 226-234, 1998.

[103] Y. Myung-Jin and P. Kyung-Wook, "The contact resistance and reliability of anisotropically conductive film (ACF)," *Advanced Packaging, IEEE Transactions on,* vol. 22, pp. 166-173, 1999.

[104] J. C. Agar, J. Durden, R. W. Zhang, D. Staiculescu, and C. P. Wong, "Kinetically Controlled Assembly of Terpheny-4,4”-dithiol Self-Assembled Monolayers (SAMs) for Highly Conductive Anisotropically Conductive Adhesives (ACA)," presented at the ECTC, Orlando, 2011.

[105] R. L. McCreery, "Molecular Electronic Junctions," *Chemistry of Materials,* vol. 16, pp. 4477-4496, 2004.

[106] V. Mujica and M. A. Ratner, "Current-voltage characteristics of tunneling molecular junctions for off-resonance injection," *Chemical Physics,* vol. 264, pp. 365-370, 2001.

[107] V. Mujica, A. E. Roitberg, and M. Ratner, "Molecular wire conductance: Electrostatic potential spatial profile," *The Journal of Chemical Physics,* vol. 112, pp. 6834-6839, 2000.

[108] S. Baranovski and O. Rubel, "Description of Charge Transport in Amorphous Semiconductors," in *Charge Transport in Disordered Solids with Applications in Electronics*, S. Baranovski, Ed., ed: John WIley & Sons, 2006.

[109] J. Brunson, "Hopping Conductivity and Charge Transport in Low Density Polyethylene," Ph.D., Physics, Utah State University, Logan, 2010.

[110] D. K. Davies, "Carrier transport in polythene," *Journal of Physics D: Applied Physics,* vol. 5, p. 162, 1972.

[111] J. R. Dennison and J. Brunson, "Temperature and Electric Field Dependence of Conduction in Low-Density Polyethylene," *Plasma Science, IEEE Transactions on,* vol. 36, pp. 2246-2252, 2008.

[112] T. Renger and R. A. Marcus, "Variable-Range Hopping Electron Transfer through Disordered Bridge States: Application to DNA," *The Journal of Physical Chemistry A,* vol. 107, pp. 8404-8419, 2003.

[113] H. J. Wintle, "Charge motion and trapping in insulators: surface and bulk effects," *Dielectrics and Electrical Insulation, IEEE Transactions on,* vol. 6, pp. 1-10, 1999.

[114] H. J. Wintle, "Charge motion in technical insulators: facts, fancies and simulations," *Dielectrics and Electrical Insulation, IEEE Transactions on,* vol. 10, pp. 826-841, 2003.

[115] A. Miller and E. Abrahams, "Impurity Conduction at Low Concentrations," *Physical Review,* vol. 120, p. 745, 1960.

[116] H. P. Wu, J. F. Liu, X. J. Wu, M. Y. Ge, Y. W. Wang, G. Q. Zhang, and J. Z. Jiang, "High conductivity of isotropic conductive adhesives filled with silver nanowires," *International Journal of Adhesion and Adhesives,* vol. 26, pp. 617-621, 2006.

[117] H. Wu, X. Wu, J. Liu, G. Zhang, Y. Wang, Y. Zeng, and J. Jing, "Development of a novel isotropic conductive adhesive filled with silver nanowires," *Journal of Composite Materials,* vol. 40, pp. 1961-1969, 2006.

[118] Y. Tao, Y. Xia, H. Wang, F. Gong, H. Wu, and G. Tao, "Novel isotropical conductive adhesives for electronic packaging application," *IEEE Transactions on Advanced Packaging,* vol. 32, pp. 589-592, 2009.

[119] F. Marcq, P. Demont, P. Monfraix, A. Peigney, C. Laurent, T. Falat, F. Courtade, and T. Jamin, "Carbon nanotubes and silver flakes filled epoxy resin for new hybrid conductive adhesives," *Microelectronics Reliability,* vol. In Press, Corrected Proof.

[120] I. Reinhold, C. E. Hendriks, R. Eckardt, J. M. Kranenburg, J. Perelaer, R. R. Baumann, and U. S. Schubert, "Argon plasma sintering of inkjet printed silver

tracks on polymer substrates," *Journal of Materials Chemistry,* vol. 19, pp. 3384-3388, 2009.

[121] J. Perelaer, B.-J. de Gans, and U. S. Schubert, "Ink-jet printing and microwave sintering of conductive silver tracks," *Advanced Materials (Weinheim, Germany),* vol. 18, pp. 2101-2104, 2006.

[122] T. H. J. van Osch, J. Perelaer, A. W. M. de Laat, and U. S. Schubert, "Inkjet printing of narrow conductive tracks on untreated polymeric substrates," *Advanced Materials (Weinheim, Germany),* vol. 20, pp. 343-345, 2008.

[123] J. Perelaer, M. Klokkenburg, C. E. Hendriks, and U. S. Schubert, "Microwave Flash Sintering of Inkjet-Printed Silver Tracks on Polymer Substrates," *Advanced Materials (Weinheim, Germany),* vol. 21, pp. 4830-4834, 2009.

[124] M. Grouchko, A. Kamyshny, and S. Magdassi, "Formation of air-stable copper-silver core-shell nanoparticles for ink-jet printing," *Journal of Materials Chemistry,* vol. 19, pp. 3057-3062, 2009.

[125] E. Ide, S. Angata, A. Hirose, and K. F. Kobayashi, "Metal-metal bonding process using Ag metallo-organic nanoparticles," *Acta Materialia,* vol. 53, pp. 2385-2393, 2005.

[126] R. Zhang, K.-s. Moon, W. Lin, and C. P. Wong, "Preparation of highly conductive polymer nanocomposites by low temperature sintering of silver nanoparticles," *Journal of Materials Chemistry,* vol. 20, pp. 2018-2023, 2010.

[127] R. Zhang, W. Lin, K.-s. Moon, and C. P. Wong, "Fast Preparation of Printable Highly Conductive Polymer Nanocomposites by Thermal Decomposition of Silver Carboxylate and Sintering of Silver Nanoparticles," *ACS Applied Materials & Interfaces,* p. in press.

[128] K.-S. Moon, H. Dong, R. Maric, S. Pothukuchi, A. Hunt, Y. Li, and C. P. Wong, "Thermal behavior of silver nanoparticles for low-temperature interconnect applications," *Journal of Electronic Materials,* vol. 34, pp. 168-175, 2005.

[129] R. N. Das, F. D. Egitto, and V. R. Markovich, "Nano- and micro-filled conducting adhesives for z-axis interconnections: new direction for high-speed, high-density, organic microelectronics packaging," *Circuit World,* vol. 34, pp. 3-12, 2008.

[130] J. G. Bai, T. G. Lei, J. N. Calata, and G.-Q. Lu, "Control of nanosilver sintering attained through organic binder burnout," *Journal of Materials Research,* vol. 22, pp. 3494-3500, 2007.

[131] T. Wang, X. Chen, G.-Q. Lu, and G.-Y. Lei, "Low-temperature sintering with nano-silver paste in die-attached interconnection," *Journal of Electronic Materials,* vol. 36, pp. 1333-1340, 2007.

[132] H. Jiang, K.-S. Moon, J. Lu, and C. P. Wong, "Conductivity enhancement of nano silver-filled conductive adhesives by particle surface functionalization," *Journal of Electronic Materials,* vol. 34, pp. 1432-1439, 2005.

[133] H. Jiang, K.-S. Moon, Y. Li, and C. P. Wong, "Surface Functionalized Silver Nanoparticles for Ultrahigh Conductive Polymer Composites," *Chemistry of Materials,* vol. 18, pp. 2969-2973, 2006.

[134] H.-H. Lee, K.-S. Chou, and Z.-W. Shih, "Effect of nano-sized silver particles on the resistivity of polymeric conductive adhesives," *International Journal of Adhesion and Adhesives,* vol. 25, pp. 437-441, 2005.

[135] L. Ye, Z. Lai, J. Liu, and A. Tholen, "Effect of Ag particle size on electrical conductivity of isotropically conductive adhesives," *IEEE Transactions on Electronics Packaging Manufacturing,* vol. 22, pp. 299-302, 1999.

[136] R. Zhang and C. P. Wong, "Advanced Interconnect materials for ink-jet printing by low temperature sintering," *IEEE Electronic Components and Technology Conference,* vol. 59th, pp. 150-154, 2009.

[137] M. M. Hou and T. W. Eagar, "Low temperature transient liquid phase (LTTLP) bonding for Au/Cu and Cu/Cu interconnections," *Journal of Electronic Packaging,* vol. 114, pp. 443-447, 1992.

[138] R. Zhang, J. C. Agar, and C. P. Wong, *Conductive Polymer Composites*: John Wiley & Sons, Inc., 2010.

[139] D. Lu, Q. K. Tong, and C. P. Wong, "Conductivity mechanisms of isotropic conductive adhesives (ICA's)," *IEEE Transactions on Electronics Packaging Manufacturing,* vol. 22, pp. 223-227, 1999.

[140] D. Lu and C. P. Wong, "Effects of shrinkage on conductivity of isotropic conductive adhesives," *International Journal of Adhesion and Adhesives,* vol. 20, pp. 189-193, 2000.

[141] J. Miragliotta, R. C. Benson, and T. E. Phillips, "Vibrational analysis of a stearic acid adlayer adsorbed on a silver flake substrate," *Mater. Res. Soc. Symp. Proc.,* vol. 445, pp. 217-222, 1997.

[142] D. L. Markley, Q. K. Tong, D. J. Magliocca, and T. D. Hahn, "Characterization of silver flakes utilized for isotropic conductive adhesives," *Proc. - Int. Symp. Adv. Packag. Mater. Processes, Prop. Interfaces,* pp. 16-20, 1999.

[143] Y. Li, K.-S. Moon, and C. P. Wong, "Electrical property improvement of electrically conductive adhesives through in-situ replacement by short-chain difunctional acids," *IEEE Transactions on Components and Packaging Technologies,* vol. 29, pp. 173-178, 2006.

[144] Y. Li, K.-S. Moon, A. Whitman, and C. P. Wong, "Enhancement of electrical properties of electrically conductive adhesives (ECAs) by using novel aldehydes," *IEEE Transactions on Components and Packaging Technologies,* vol. 29, pp. 758-763, 2006.

[145] K. Nomura, H. Ohta, A. Takagi, T. Kamiya, M. Hirano, and H. Hosono, "Room-temperature fabrication of transparent flexible thin-film transistors using amorphous oxide semiconductors," *Nature,* vol. 432, pp. 488-492, 2004.

[146] R. J. Hamers, "Flexible electronic futures," *Nature,* vol. 412, pp. 489-490, 2001.

[147] N. Bilton. (2010, Sony Showcases New Rollable, Flexible Screen. *Bits*. Available: http://bits.blogs.nytimes.com/2010/05/26/sony-showcases-new-rollable-flexible-screen/

[148] M. Knight. (2011, Solar power enters the plastic age. *Earth's Frontiers*. Available: http://www.cnn.com/2011/TECH/innovation/01/21/plastic.solar.panel.revolution/index.html

[149] H. C. Ko, M. P. Stoykovich, J. Song, V. Malyarchuk, W. M. Choi, C.-J. Yu, J. B. Geddes Iii, J. Xiao, S. Wang, Y. Huang, and J. A. Rogers, "A hemispherical

electronic eye camera based on compressible silicon optoelectronics," *Nature,* vol. 454, pp. 748-753, 2008.

[150] D.-H. Kim, J.-H. Ahn, W. M. Choi, H.-S. Kim, T.-H. Kim, J. Song, Y. Y. Huang, Z. Liu, C. Lu, and J. A. Rogers, "Stretchable and Foldable Silicon Integrated Circuits," *Science,* vol. 320, pp. 507-511, April 25, 2008 2008.

[151] D.-H. Kim, N. Lu, R. Ghaffari, Y.-S. Kim, S. P. Lee, L. Xu, J. Wu, R.-H. Kim, J. Song, Z. Liu, J. Viventi, B. de Graff, B. Elolampi, M. Mansour, M. J. Slepian, S. Hwang, J. D. Moss, S.-M. Won, Y. Huang, B. Litt, and J. A. Rogers, "Materials for multifunctional balloon catheters with capabilities in cardiac electrophysiological mapping and ablation therapy," *Nat Mater,* vol. 10, pp. 316-323, 2011.

[152] J. Lee, J. Wu, M. Shi, J. Yoon, S.-I. Park, M. Li, Z. Liu, Y. Huang, and J. A. Rogers, "Stretchable GaAs Photovoltaics with Designs That Enable High Areal Coverage," *Advanced Materials,* vol. 23, pp. 986-991, 2011.

[153] J. Viventi, D.-H. Kim, J. D. Moss, Y.-S. Kim, J. A. Blanco, N. Annetta, A. Hicks, J. Xiao, Y. Huang, D. J. Callans, J. A. Rogers, and B. Litt, "A Conformal, Bio-Interfaced Class of Silicon Electronics for Mapping Cardiac Electrophysiology," *Science Translational Medicine,* vol. 2, p. 24ra22, March 24, 2010 2010.

[154] D.-H. Kim, J. Viventi, J. J. Amsden, J. Xiao, L. Vigeland, Y.-S. Kim, J. A. Blanco, B. Panilaitis, E. S. Frechette, D. Contreras, D. L. Kaplan, F. G. Omenetto, Y. Huang, K.-C. Hwang, M. R. Zakin, B. Litt, and J. A. Rogers, "Dissolvable films of silk fibroin for ultrathin conformal bio-integrated electronics," *Nat Mater,* vol. 9, pp. 511-517, 2010.

[155] S.-I. Park, A.-P. Le, J. Wu, Y. Huang, X. Li, and J. A. Rogers, "Light Emission Characteristics and Mechanics of Foldable Inorganic Light-Emitting Diodes," *Advanced Materials,* vol. 22, pp. 3062-3066, 2010.

[156] R.-H. Kim, D.-H. Kim, J. Xiao, B. H. Kim, S.-I. Park, B. Panilaitis, R. Ghaffari, J. Yao, M. Li, Z. Liu, V. Malyarchuk, D. G. Kim, A.-P. Le, R. G. Nuzzo, D. L. Kaplan, F. G. Omenetto, Y. Huang, Z. Kang, and J. A. Rogers, "Waterproof AlInGaP optoelectronics on stretchable substrates with applications in biomedicine and¬†robotics," *Nat Mater,* vol. 9, pp. 929-937, 2010.

[157] D. Lu and C. Wong, "Effects of shrinkage on conductivity of isotropic conductive adhesives," *International journal of adhesion and adhesives,* vol. 20, pp. 189-193, 2000.

[158] D. Lu, Q. K. Tong, and C. Wong, "Conductivity mechanisms of isotropic conductive adhesives (ICAs)," *Electronics Packaging Manufacturing, IEEE Transactions on,* vol. 22, pp. 223-227, 1999.

[159] Y. K.-s. M. R. Z. C. P. W. Yi Li; Myung Jim, "Development of novel, flexible, electrically conductive adhesives for next-generation microelectronics interconnect applications," *Electronic Components and Technology Conference,* pp. 1272-1276, May 27-30 2008.

[160] D. D. Lu and C. P. Wong, "Recent advances in developing high performance isotropic conductive adhesives," *Journal of Adhesion Science and Technology,* vol. 22, pp. 835-851, 2008.

[161] D. Lu, C. P. Wong, and Q. K. Tong, "A fundamental study on silver flakes for conductive adhesives," *Proceedings - International Symposium on Advanced Packaging Materials: Processes, Properties and Interfaces, 4th, Braselton, Ga., Mar. 15-18, 1998,* pp. 256-260, 1998.

[162] D. Lu and C. P. Wong, "High performance conductive adhesives," *IEEE Transactions on Electronics Packaging Manufacturing,* vol. 22, pp. 324-330, 1999.

[163] D. Lu, Q. K. Tong, and C. P. Wong, "Mechanisms underlying the unstable contact resistance of conductive adhesives," *IEEE Transactions on Electronics Packaging Manufacturing,* vol. 22, pp. 228-232, 1999.

[164] Y. Li, K.-s. Moon, H. Li, and C. P. Wong, "Conductivity improvement of isotropic conductive adhesives with short-chain dicarboxylic acids," *Proceedings - Electronic Components & Technology Conference,* vol. 54th, pp. 1959-1964, 2004.

[165] H. Hertz, "Miscellaneous Papers " 1986.

[166] H. Hertz, "Ueber die Ber¸hrung fester elastischer Kˆrper," *Journal f¸r die reine und angewandte Mathematik (Crelle's Journal),* vol. 1882, pp. 156-171, 1882.

[167] K. R. Shull, D. Ahn, W. L. Chen, C. M. Flanigan, and A. J. Crosby, "Axisymmetric adhesion tests of soft materials," *Macromolecular Chemistry and Physics,* vol. 199, pp. 489-511, Apr 1998.

[168] L. M. Grant, T. Ederth, and F. Tiberg, "Influence of surface hydrophobicity on the layer properties of adsorbed nonionic surfactants," *Langmuir,* vol. 16, pp. 2285-2291, Mar 7 2000.

[169] Y. Rao, S. Ogitani, P. Kohl, and C. P. Wong, "Novel polymer-ceramic nanocomposite based on high dielectric constant epoxy formula for embedded capacitor application," *Journal of Applied Polymer Science,* vol. 83, pp. 1084-1090, 2002.

[170] E. M. Vogel, K. Z. Ahmed, B. Hornung, W. K. Henson, P. K. McLarty, G. Lucovsky, J. R. Hauser, and J. J. Wortman, "Modeled tunnel currents for high dielectric constant dielectrics," *Electron Devices, IEEE Transactions on,* vol. 45, pp. 1350-1355, 1998.

[171] J. G. Simmons, "Generalized Formula for the Electric Tunnel Effect between Similar Electrodes Separated by a Thin Insulating Film," *Journal of Applied Physics,* vol. 34, pp. 1793-1803, 1963.

[172] T. Sekitani and T. Someya, "Stretchable, Large-area Organic Electronics," *Advanced Materials,* vol. 22, pp. 2228-2246, 2010.

[173] S.-I. Park, J.-H. Ahn, X. Feng, S. Wang, Y. Huang, and J. A. Rogers, "Theoretical and Experimental Studies of Bending of Inorganic Electronic Materials on Plastic Substrates," *Advanced Functional Materials,* vol. 18, pp. 2673-2684, 2008.

[174] D.-Y. Khang, H. Jiang, Y. Huang, and J. A. Rogers, "A Stretchable Form of Single-Crystal Silicon for High-Performance Electronics on Rubber Substrates," *Science,* vol. 311, pp. 208-212, January 13, 2006 2006.

[175] Y. Sun, W. M. Choi, H. Jiang, Y. Y. Huang, and J. A. Rogers, "Controlled buckling of semiconductor nanoribbons for stretchable electronics," *Nat Nano,* vol. 1, pp. 201-207, 2006.

[176] H. Kevin, R. Dinyari, G. Lanzara, K. Jong Yon, F. Jianmin, C. Vancura, C. Fu-Kuo, and P. Peumans, "An Approach to Cost-Effective, Robust, Large-Area

Electronics using Monolithic Silicon," in *Electron Devices Meeting, 2007. IEDM 2007. IEEE International*, 2007, pp. 217-220.

[177] P. J. Hung, K. Jeong, G. L. Liu, and L. P. Lee, "Microfabricated suspensions for electrical connections on the tunable elastomer membrane," *Applied Physics Letters,* vol. 85, pp. 6051-6053, 2004.

[178] D. S. Gray, J. Tien, and C. S. Chen, "High-Conductivity Elastomeric Electronics (Adv. Mater. 2004, 16, 393.)," *Advanced Materials,* vol. 16, pp. 477-477, 2004.

[179] D. H. Kim, J. Song, W. M. Choi, H. S. Kim, R. H. Kim, Z. Liu, Y. Y. Huang, K. C. Hwang, Y. Zhang, and J. A. Rogers, "Materials and noncoplanar mesh designs for integrated circuits with linear elastic responses to extreme mechanical deformations," *Proceedings of the National Academy of Sciences,* vol. 105, p. 18675, 2008.

[180] B. O. Kolbesen, C. Claeys, P. Stallhofer, and F. Tardiff, *Analytical and Diagnostic Techniques for Semiconductor Materials, Devices and Processes* Electrochemical Society, Incorporated, 1999.

[181] N. Bowden, S. Brittain, A. G. Evans, J. W. Hutchinson, and G. M. Whitesides, "Spontaneous formation of ordered structures in thin films of metals supported on an elastomeric polymer," *Nature,* vol. 393, pp. 146-149, 1998.

[182] S. P. Lacour, S. Wagner, Z. Huang, and Z. Suo, "Stretchable gold conductors on elastomeric substrates," *Applied Physics Letters,* vol. 82, pp. 2404-2406, 2003.

[183] S. P. Lacour, D. Chan, S. Wagner, T. Li, and Z. Suo, "Mechanisms of reversible stretchability of thin metal films on elastomeric substrates," *Applied Physics Letters,* vol. 88, pp. 204103-3, 2006.

[184] L. Guo and S. P. DeWeerth, "High-Density Stretchable Electronics: Toward an Integrated Multilayer Composite," *Advanced Materials,* vol. 22, pp. 4030-4033, 2010.

[185] "Emerson & Cumings: Microwave Products," ed.

[186] K.-Y. Chun, Y. Oh, J. Rho, J.-H. Ahn, Y.-J. Kim, H. R. Choi, and S. Baik, "Highly conductive, printable and stretchable composite films of carbon nanotubes and silver," *Nat Nano,* vol. 5, pp. 853-857, 2010.

[187] T. Sekitani, Y. Noguchi, K. Hata, T. Fukushima, T. Aida, and T. Someya, "A Rubberlike Stretchable Active Matrix Using Elastic Conductors," *Science,* vol. 321, pp. 1468-1472, September 12, 2008 2008.

[188] T. Sekitani, H. Nakajima, H. Maeda, T. Fukushima, T. Aida, K. Hata, and T. Someya, "Stretchable active-matrix organic light-emitting diode display using printable elastic conductors," *Nature Materials,* vol. 8, pp. 494-499, 2009.

[189] J. C. Agar, K. J. Lin, R. Zhang, J. Durden, K.-S. Moon, and C. P. Wong, "Novel PDMS(silicone)-in-PDMS(silicone): Low cost flexible electronics without metallization," in *Electronic Components and Technology Conference (ECTC), 2010 Proceedings 60th*, 2010, pp. 1226-1230.

[190] Y. Xia and G. M. Whitesides, "SOFT LITHOGRAPHY," *Annual Review of Materials Science,* vol. 28, p. 153, 1998.

[191] S. Befahy, P. Lipnik, T. Pardoen, C. Nascimento, B. Patris, P. Bertrand, and S. Yunus, "Thickness and Elastic Modulus of Plasma Treated PDMS Silica-like Surface Layer," *Langmuir,* vol. 26, pp. 3372-3375, Mar 2010.

[192] S. Béfahy, S. Yunus, V. Burguet, J. S. Heine, M. Troosters, and P. Bertrand, "Stretchable Gold Tracks on Flat Polydimethylsiloxane (PDMS) Rubber Substrate," *Journal of Adhesion,* vol. 84, pp. 231-239, 2008.

[193] H. Gao, L. Liu, K. Liu, Y. Luo, D. Jia, and J. Lu, "Preparation of highly conductive adhesives by in situ generated and sintered silver nanoparticles during curing process," *Journal of Materials Science: Materials in Electronics,* pp. 1-9, 2011.

[194] R.-W. Zhang, K.-S. Moon, W. Lin, J. C. Agar, and C.-P. Wong, "A simple, low-cost approach to prepare flexible highly conductive polymer composites by in situ reduction of silver carboxylate for flexible electronic applications," *Compos. Sci. Technol.,* vol. 71, pp. 528-534, 2011.

[195] R. Zhang, W. Lin, K.-s. Moon, and C. P. Wong, "Fast Preparation of Printable Highly Conductive Polymer Nanocomposites by Thermal Decomposition of

Silver Carboxylate and Sintering of Silver Nanoparticles," *ACS Appl. Mater. Interfaces,* vol. 2, pp. 2637-2645, 2010.

[196] J. Agar, J. Durden, D. Staiculescu, R. W. Zhang, E. Gebara, and C. P. Wong, "Electrically Conductive Silicone Nano-Composites For Stretchable RF Devices " in *Microwave Symposium Digest, 2011. MTT '11. IEEE MTT-S International*, 2011.

[197] X. Z. Niu, S. L. Peng, L. Y. Liu, W. J. Wen, and P. Sheng, "Characterizing and Patterning of PDMS-Based Conducting Composites," *Advanced Materials,* vol. 19, pp. 2682-2686, 2007.

[198] J. C. Agar, J. Durden, R. W. Zhang, D. Staiculescu, and C. P. Wong, "Through Silicone Vias: Multilayer Interconnects for Stretchable Electronics," presented at the ECTC, Orlando, 2011.

[199] G. Socrates, *Infrared and Raman characteristic group frequencies: tables and charts*: John Wiley & Sons Inc, 2004.

[200] K. P. Menard, *Dynamic Mechanical Analysis*: John Wiley & Sons, Inc., 2002.

[201] J. D. Boerman and J. T. Bernhard, "Performance Study of Pattern Reconfigurable Antennas in MIMO Communication Systems," *Antennas and Propagation, IEEE Transactions on,* vol. 56, pp. 231-236, 2008.

[202] N. Tiercelin and et al., "Polydimethylsiloxane membranes for millimeter-wave planar ultra flexible antennas," *Journal of Micromechanics and Microengineering,* vol. 16, p. 2389, 2006.

[203] J. H. So, J. Thelen, A. Qusba, G. J. Hayes, G. Lazzi, and M. D. Dickey, "Reversibly deformable and mechanically tunable fluidic antennas," *Advanced Functional Materials,* vol. 19, pp. 3632-3637, 2009.

[204] M. Kubo, X. Li, C. Kim, M. Hashimoto, B. J. Wiley, D. Ham, and G. M. Whitesides, "Stretchable Microfluidic Radiofrequency Antennas," *Advanced Materials,* vol. 22, pp. 2749-2752, 2010.

[205] S. Cheng, Z. Wu, P. Hallbjorner, K. Hjort, and A. Rydberg, "Foldable and Stretchable Liquid Metal Planar Inverted Cone Antenna," *Antennas and Propagation, IEEE Transactions on,* vol. 57, pp. 3765-3771, 2009.